

**Iron/Chromium Phase Decomposition Behavior in
Oxide Dispersion Strengthened Ferritic Steels**

CHEN DONGSHENG

Graduate School of Energy Science

Kyoto University

2015

Table of Contents

Chapter 1. Introduction.....	1
1.1. Backgrounds.....	2
1.2. Nuclear energy systems.....	3
1.2.1. Fission reactors.....	3
1.2.2. Generations IV reactors.....	3
1.2.3. Fusion reactors.....	5
1.3. Materials for advanced fission and fusion reactors.....	7
1.3.1. Conventional structural materials.....	7
1.3.2. Advanced structural materials.....	9
1.3.2.1. History of ODS steels.....	9
1.3.2.2. Development of ODS steels for advanced nuclear systems.....	10
1.3.2.3. Issues of development of high-Cr ODS ferritic steels.....	12
1.4. Literature survey.....	13
1.4.1. Aging effect on high-Cr ferritic alloys.....	13
1.4.2. Aging effect on high-Cr ODS ferritic steels.....	16
1.5. Objectives of this research.....	21
References.....	22
Chapter 2. Effects of Alloying Elements on Age-hardening Behavior of Fe-15Cr Alloys.....	27
2.1. Introduction.....	28
2.2. Experimental.....	29
2.2.1. Materials.....	29
2.2.2. Microstructural observation.....	31
2.2.3. Hardness measurements and tensile tests.....	32
2.2.4. Thermal aging condition.....	33
2.3. Results.....	34
2.3.1. Microstructural changes.....	34
2.3.1.1. Alloying effect.....	34
2.3.1.2. Thermal aging effect.....	35

2.3.2. Mechanical property changes	39
2.3.2.1. Vickers hardness evolution	39
2.3.2.2 Tensile property changes	40
2.3.3. Rupture manners.....	41
2.4. Discussion	44
2.5 Summary	46
References	47
Chapter 3. Correlation of Fe/Cr Phase Decomposition Process and Age-hardening in Fe-15Cr alloy	49
3.1. Introduction	50
3.2. Experimental	50
3.3. Results	52
3.3.1. Age-hardening behavior	52
3.3.2. Microstructure changes	53
3.4. Discussion	56
3.4.1. Phase decomposition characteristic	56
3.4.2. Age-hardening mechanism.....	60
3.4.2.1. Strengthening stage	60
3.4.2.2. Softening stage	62
3.5. Summary	65
References	66
Chapter 4. Age-hardening Susceptibility of High-Cr ODS Ferritic steels and SUS430 Ferritic Steel	68
4.1. Introduction	69
4.2. Experimental	69
4.2.1. Materials.....	69
4.2.2. Mechanical property tests.....	71
4.2.3. Microstructural observation.....	72
4.2.4. Thermal aging condition.....	72

4.3. Results	73
4.3.1. Mechanical property changes	73
4.3.1.1. Vickers hardness evolution	73
4.3.1.2. Tensile property changes	75
4.3.1.3. Small punch (SP) tests	76
4.3.2. Microstructures	79
4.3.2.1. TEM microstructures	79
4.3.2.2. High-resolution TEM images	82
4.3.2.3. Rupture surfaces	83
4.3.2.4. SP Fracture surfaces	83
4.4. Discussion	86
4.4.1. Correlation of age-hardening with microstructure evolution	86
4.4.2. Nucleation rate	86
4.4.3. Age-hardening mechanism	88
4.4.4. Mechanism of no-loss-of-elongation	89
4.5. Summary	90
References	91
Chapter 5. Characteristic Age-hardening Behavior of 15Cr-ODS Ferritic Steel	94
5.1. Introduction	95
5.2. Experimental	95
5.3. Results	99
5.3.1. Microhardness measurement	99
5.3.2. Tensile properties	100
5.3.3. Microstructure changes	102
5.4. Discussion	108
5.4.1. Age-hardening mechanism	108
5.4.2. Precipitation modeling	109
5.4.2.1. Nucleation	109
5.4.2.2. Growth	110
5.4.3. Roles of oxide particles	111

5.5. Summary	112
References	113
Chapter 6. Summary and Conclusions	116
List of Publications.....	121
List of Presentations	122
Acknowledgement.....	124

Chapter 1

Introduction

1.1. Backgrounds

According to the reports of International Energy Outlook 2014 (IEO2014) [1], world energy consumption will continue to increase by 2% per year. Non-OECD (Economic Cooperation and Development) regions account for virtually all of the increase in demand for petroleum and other liquid fuels, as shown in figure 1-1(a) [2]. In particular, non-OECD Asia and the Middle East account for 85% of the total increase in world liquid fuels consumption, as presented in figure 1-1(b). Fast-paced economic expansion among the non-OECD regions drives the increase in demand for fossil fuels, which continue to supply almost 80 percent of world energy use through 2040.

For continuous economic growth, each country has to make efforts to reduce the consumption of oil and natural gas. Renewable energy and nuclear power are the world's fastest-growing energy sources, each increasing by 2.5% per year. In this situation, nuclear energy is reconsidered to be a possible future energy in the world, because the nuclear power can continuously maintain stable energy supplies and play a role as a carbon-free alternative to fossil energy. Although new energy sources like solar energy or renewable energy have a similar possibility, their economic efficiency and reliability are still insufficient for high density electric power generation. However, the technology and economic efficiency of nuclear energy have been expected to be able to satisfy the current energy demands.

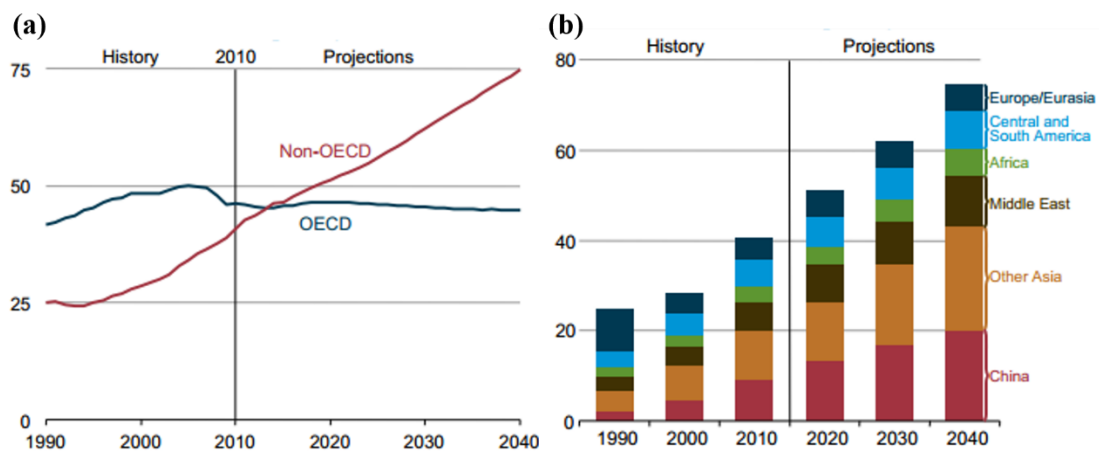


Figure 1-1 OECD and Non-OECD petroleum and other liquid fuels consumption, Reference case, 1990-2040 (million barrels per day) [2].

1.2. Nuclear energy systems

1.2.1. Fission reactors

Nuclear energy systems are classified by the generation [3], as shown in figure 1-2. The basic components of a nuclear reactor are the nuclear fuel, the moderator, the control rods and the coolant. Current reactors in operation around the world are generally considered to be the Generation II or III systems, while the Generation I systems retired some years ago. There are many possible nuclear reactor sizes and configurations, with different fuel compositions, moderators, coolants and control mechanisms, all capable of allowing a nuclear chain reaction to be sustained and controlled. Many of these configurations have been investigated and studied in research programs or as prototype commercial plants, though only a few have been developed to the point of industrial maturity. The most successful reactor type is the Light Water Reactor (LWR), which uses ordinary water under high pressure as both the coolant and the moderator. LWRs come in two design configurations - the Pressurized Water Reactor (PWR) and the Boiling Water Reactor (BWR).

1.2.2. Generations IV reactors

Many reactor types were considered initially for the Generations IV reactors, and the following promising nuclear systems were selected: Gas Cooled Fast Reactor (GFR), Lead Cooled Fast Reactor (LFR), Molten Salt Reactor (MSR), Sodium Cooled Fast Reactor (SFR), Supercritical Water Reactor (SCWR), Very High Temperature Reactor (VHTR).

Relative to the current nuclear power plant technology, the benefits for Gen IV include: 1) Nuclear waste that remains radioactive for a few centuries instead of millennia; 2) 100-300 times more energy yield from the same amount of nuclear fuel; 3) The ability to consume existing nuclear waste in the production of electricity; 4) Improved operating safety. Several materials, such as ferritic/martensitic (F/M) stainless steel, oxide dispersion strengthened (ODS) steel, nickel-based super alloys, refractory metals and ceramic materials (SiC and ZrC), have been suggested as candidate fuel cladding materials for Generations IV reactors, as listed in Table 1.1.

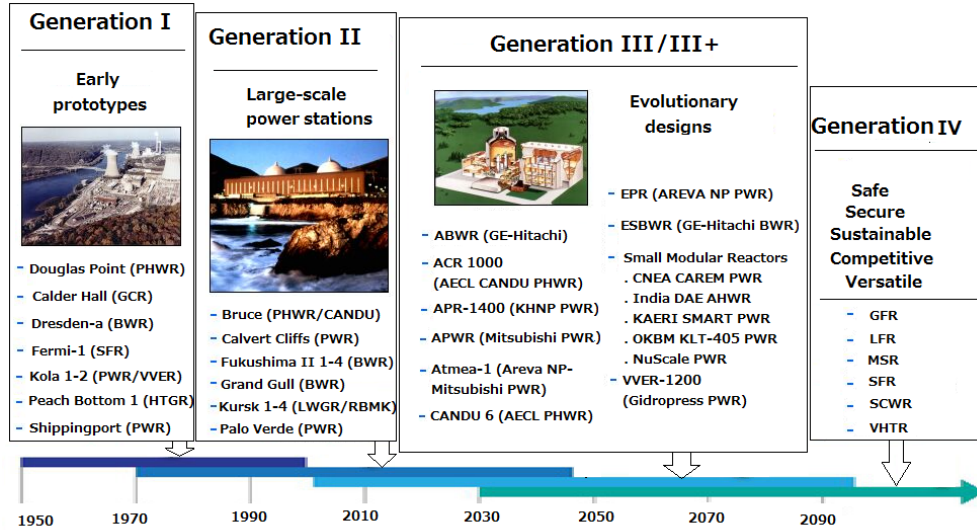


Figure 1-2 Generation systems of nuclear energy [3].

Table 1-1 Summary of design parameters for different GEN-IV concepts

Concept	VHTR	SCWR	MSR	GFR	SFR	LFR
Spectrum	Thermal			Fast		
Cladding	ZrC coating	F/M, Incoloy800, Inconel 690, 625&718	Not applicable	Ceramics	F/M, F/M ODSS	F/M, Ceramics, refractory alloys
Core structures	C/C, SiC _f /SiC	Ni alloys & F/M, ODSS	Hastelloy	SiC _f / SiC	F/M, F/M ODSS	F/M, ODSS
Reactor power (MW)	600	1700	1000	600	-	-
Net plant efficiency (%)	>50	44	44-50	48	-	-
Coolant	He	Water	Molten salt	He	Liquid Na	Lead alloy
Coolant T _{inlet} (°C)	640	280	565	490	-	-
Coolant T _{outlet} (°C)	1000	510	700-800	850	520	550-800

Abbreviations: F/M: Ferritic/martensitic steels (9-12wt. %Cr);

ODS: Oxide dispersion strengthened steels.

1.2.3. Fusion reactors

Fusion power would provide much more energy for a given weight of fuel than any technology currently in use and the fuel itself (primarily deuterium) exists abundantly in the ocean: about 1 in 6500 hydrogen atoms in seawater is deuterium. Because nuclear fusion reactions are so much more energetic than chemical combustion, and seawater is easier to access and more plentiful than fossil fuels, fusion could potentially supply the world's energy needs for millions of years. Despite being technically non-renewable, fusion power has many of the benefits of renewable energy sources (such as being a long-term energy supply and emitting no greenhouse gases) as well as some of the benefits of the resource-limited energy sources as hydrocarbons and nuclear fission (without reprocessing). Like these currently dominant energy sources, fusion could provide very high power-generation density and uninterrupted power delivery.

Among the fusion reactions (1.1-3), the following reaction (1.1) has been considered to be most adequate for near-future realization of fusion energy. This fusion reaction occurs between the nuclei of the two heavy isotopes of hydrogen-deuterium (D) and Tritium (T) – to form a helium nucleus and the release of a neutron and high energy:



Several tokamaks have been built, including the Joint European Torus (JET) and the Mega Amp Spherical Tokamak (MAST) in the UK and the tokamak fusion test reactor (TFTR) at Princeton in the USA. Although many fusion reactor concepts have been developed, the most typical magnetic storage configuration will probably be Tokamak type [5]. For its advance and development, the international thermo-nuclear reactor (ITER) was organized by international cooperation established by China, the European Union, India, Japan, Korea, Russia, and the United States. ITER's mission is to demonstrate the feasibility of fusion power, and prove that it can work without negative impact. The mission did not include a complete set up of blankets for energy generation. A part of blankets will be assembled as a test blanket module (TBM). A summary of structural materials [6] for fusion blanket and divertor is given in Table 1-2.

Table 1-2 Main candidate materials for plasma facing and breeding blanket components.

Function	First wall	Breeding blanket	Divertor
Plasma facing material	W-base alloy,	-	W-base alloy,
	W-coated ODS steel,		W-coated SiC _f /SiC,
	Flowing liquid metal: Li		Flowing liquid metal: Li, Ga, Sn, Sn-Li
Neutron multiplier material	-	Be, Be ₁₂ Ti, Be ₁₂ V, Pb	-
Tritium breeding material		Li, eutectic Pb-Li, Li-base ceramic	
		material (Li ₂ O, Li ₄ SiO ₄ , Li ₂ TiO ₃ ,	
		Li ₂ ZrO ₃ , LiAlO ₂)	
Structural material	RAFM steel, ODS steel,	RAFM steel, ODS steel,	ODS steel,
	Vanadium alloy, SiC _f /SiC	Vanadium alloy, SiC _f /SiC	W-base alloy
Coolant	-	Water, helium, eutectic Pb-Li, Li	Water, helium

Abbreviations: RAFM: Reduced activation ferritic/martensitic steel.

1.3. Materials for advanced fission and fusion reactors

Generation IV cladding and fusion blanket materials have more stringent requirements, such as superior resistance to radiation damage; outstanding dimensional stability against thermal (500-1000 °C) and irradiation creep (doses up to 200 dpa); corrosion resistance in the working environment. Because of these strict constraints, most materials employed for the fuel cladding in current commercial reactors are not suitable. Structural materials represent the key for containment of nuclear fuel and fission products as well as reliable and thermodynamically efficient production of electrical energy from nuclear reactors.

The main requirements for the materials to be used in advanced reactor systems are as follows [7]: 1) In-core materials need to exhibit excellent dimensional stability under irradiation, whether under stress (irradiation creep or relaxation) or without stress (swelling, growth). 2) Mechanical properties of all structural materials (tensile strength, ductility, creep resistance, fracture toughness, stiffness) have to remain acceptable after aging, and 3) High degree of chemical compatibility between the structural materials and the coolant as well as with the fuel. In this regard, degradation of toughness caused by thermal aging and irradiation are issues of important. These requirements have to be met under normal operating conditions, as well as in incidental and accidental conditions.

1.3.1. Conventional structural materials

Austenitic stainless steels were considered as the first structural material of fast reactor and fusion reactor as well as candidates for the supercritical water cooled reactors (SCWR) fuel assemblies and core internals. There is some overlap with the ITER operating temperature regime for 316LN at 280-300 °C, where austenitic stainless steels suffer severe irradiation hardening accompanied by a reduction in uniform strain and fracture toughness. Irradiation-assisted stress corrosion cracking is of much concern at temperatures below 350 °C. For operating temperature above 350 °C in the SCWR core internals, other irradiation effects, such as void swelling and grain boundary segregation as well as helium bubble coarsening, become important in the stainless steels. For swelling resistance and higher creep

strength, the addition of small amount of Ti, B and P to stainless steels is required; examples include Japanese PNC 316 [8], French 15-15Ti alloy [9] and US HT-UPS alloy [10]. However, it has been considered that austenitic stainless steels are not suitable for fusion systems because of their low thermal conductivity, high creep rate and high susceptibility to grain boundaries helium embrittlement.

To meet the high dose and high helium generation rate conditions projected for fusion DEMO systems and beyond, effects are focused on R&D of variants of F/M steels that contain 8~9 wt.% Cr [11], which are modified for reduced activation compositions and suppression of irradiation embrittlement. These steels are also selected as a candidate material for LFR fuel assemblies and core structures as well as core internals for SCWR. As for the fission reactor applications, higher strength F/M steels, such as NF616, E911 and HCM 12A, are considered as candidate materials for operation at temperatures up to 620 °C. For irradiation temperatures below ~400 °C, radiation hardening accompanied by reduction of uniform strain and flow localization is observed in F/M steels. Additionally, significant changes in fracture behavior, such as upward shifts of ductile-brittle transition temperature and reduction of upper shelf energy, are also found.

At temperatures above ~400 °C, creep, grain boundary segregation, corrosion and helium bubble formation are important issues. Since the mid of 1980s, the fusion materials programs in Japan, the European Union and the United States of America have been developing F/M steels containing high Cr, which would lessen the environmental impact of the irradiated and activated steels after service life of a fusion reactor. These conventional F/M steels, which contain 9~12 wt.% Cr with about 1% Mo, 0.1~0.2% C and combinations of small amount of V, W and Nb, have strength at elevated temperatures and good thermal properties such as conductivity and expansion coefficient. Zirconium alloy is prompted the selection for cladding material for fission because of low neutron absorption cross-section, high strength and good corrosion performance in hot water. However, increased burn-up level is required that are very sensitive to the input from the fuel costs. Zircaloy is limited at irradiation growth and creep properties in required burn-up levels next generation systems. Also, nickel alloys have very low radiation resistance due to their face-centered cubic matrix, which promotes radiation embrittlement, swelling and phase instability.

1.3.2. Advanced structural materials

The higher operating temperatures are required for improved efficiency and safety in fusion and fission reactors. Possible materials under investigation include mechanically alloyed ferritic and F/M steels [12], refractory metal alloys and SiC/SiC composites [13]. Application of reduced activation F/M steels for fusion DEMO plants are limited to maximum operating temperatures of ~550 °C. An approach to elevate the limit service temperature of the ferritic steels, which has higher thermal conductivity and lower swelling than austenitic steels, is to disperse oxide particles in the ferritic steels. A key strategy for designing high-performance radiation-resistant materials is based on the introduction of a high, uniform density of nano-scale particles that simultaneously provide good high temperature strength and neutron radiation damage resistance.

1.3.2.1. History of ODS steels

In 1916, the tungsten filament dispersed with thorium oxide (ThO_2) was produced in Germany. In 1946, sintered aluminum powders (SAP) were developed to increase heat resistance of Al alloys. In 1962, ODS-Ni alloy with ThO_2 (TD-Ni) was developed for application to turbine. After the development of mechanical alloying method by J.S. Benjamin, INCO, in 1970, the study on dispersion strengthened alloy processing made a great progress, and resultantly, dispersion strengthening coupled with solid solution hardening was achieved in so-called high temperature alloys. The fundamental deformation properties of metals are determined by the behavior of dislocations, which are systematic line shape distortions introduced into the crystalline lattice. When the material is under stress, these dislocations can move to cause macroscopic strain. The dislocation motion can be impeded by irregularities of strain field in the crystal, such as in the form of grain boundaries, or in the form of impurities, which can act as “pinning centers” or “sinks” for the dislocations.

ODS alloys typically consist of a high temperature metal matrix - such as iron aluminide, iron chromium, iron-chromium-aluminium, with small (5-50nm) oxide particles of alumina (Al_2O_3) or yttria (Y_2O_3) dispersed within it. In order to make the second phase be uniformly distributed in the matrix metal, ODS steels are usually fabricated by powder metallurgy

method. Dispersion strengthening is one of the strengthening methods to introduce high number density of obstacles to dislocation motion. When the obstacles like compounds are distributed in the fine grains, the matrix of the alloys can be significantly improved in the strength and hardness, which may be accompanied by a slight loss of plasticity and toughness. When the particles become smaller and higher in the size and number density, respectively, the performance of the ODS alloys becomes better. Generally, the following requirements have been imposed for dispersion strengthened particles: particles size should be as small as possible (less than 10 nm), particle spacing to achieve enough performance is in the range of several tens nm. In addition, the particle should be stable under high temperature and irradiation without mutual agglomeration.

1.3.2.2. Development of ODS steels for advanced nuclear systems

ODS F/M steels containing 9-12 wt.% chromium have been developed as the fuel cladding material of sodium-cooled fast reactor (SFR) [15, 16]. Recent irradiation experiments clearly showed that the F/M ODS steels were rather highly resistant to neutron irradiation embrittlement at temperatures ranging from 300 to 500 °C up to 15 dpa [17, 18]. The ODS steels showed irradiation hardening accompanied by no-loss-of-ductility. However, the application of F/M ODS steels to the cladding of SCWR and LFR is limited because of their insufficient corrosion resistance.

For high Cr ODS ferritic steels, the most critical issue for the application to SCWR and LFR is to improve their corrosion resistance. Figure 1-3 shows the weight gain after corrosion tests in SCPW (510 °C, 25MPa) up to 1800 h. The weight gain of 9Cr-ODS steel is much larger than 16Cr-ODS steel, indicating that 9Cr-ODS steel is not adequate for application to SCWR. An EPMA and XRD analysis revealed that a thick Fe₃O₄ film was formed on the surface of 9Cr-ODS steel but not detected in the high-Cr ODS steels. It should be noted that the weight gain is much larger in SUS430 (16Cr) than in 16Cr-ODS steel. This clearly indicates that the oxide particles dispersion plays an effective role in the high corrosion resistance of ODS steels, since the corrosion resistance in water environment is mainly controlled by Cr concentration.

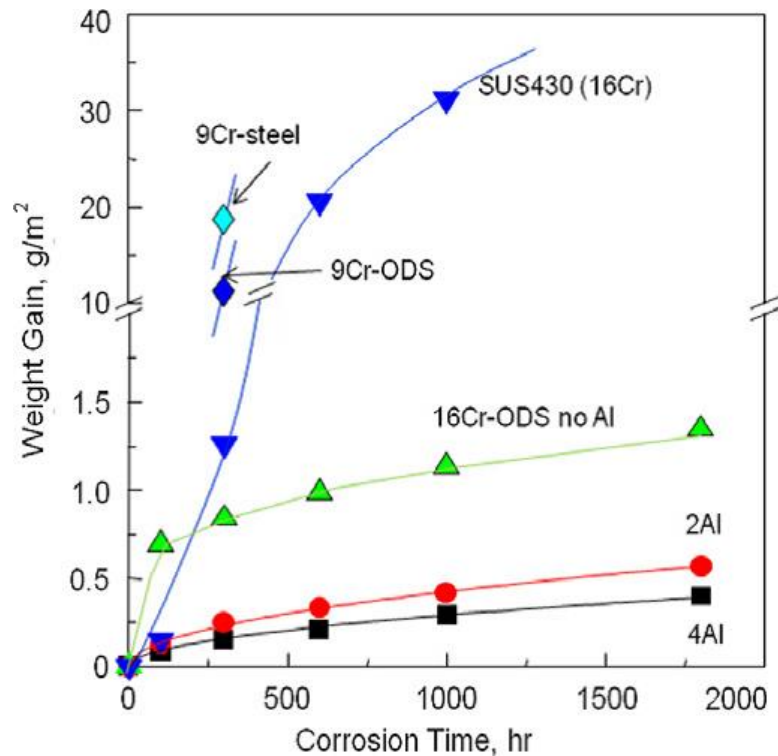


Figure 1-3 Weight gain after corrosion tests in SCPW (510 °C, 25 MPa) up to 1800 h.

The corrosion resistance of ODS steels increases with increasing chromium concentration. The effect of Al on corrosion resistance depends on Cr concentration. In 19Cr-ODS steel, the addition of 4 wt. % Al did not remarkable influence the corrosion resistance [19]. However, in 16Cr-ODS steel, the addition of Al improved corrosion resistance. The suppression of corrosion by Al addition in 16Cr-ODS steel is due to formation of very thin alumina film on the surface [20]. Most serious problem of Al addition is a loss of strength. In the Al added steel, the average diameter of the oxide particles was about 7 nm but less than 3 nm in the Al free ODS steel [21]. The number density of the oxide particles was reduced by almost one order of magnitude.

Although alumina and yttria are well known as thermally stable oxides, the possible other sort of fine oxide particles are searched for their application to strengthening of the ODS steels with Al and Y. The addition of small amount of Hf and Zr is very effective to increase the strength at 700 °C [22, 23]. TEM observation revealed that the addition of Hf and Zr reduced and increased the size and the number density of oxide particles, respectively [23]. Furthermore, the number density of grain boundary precipitates, such as carbides and oxides were increased remarkably by addition of Hf or Zr. Grain boundary precipitates are well

known as obstacles for grain boundary sliding that is a typical deformation mode at elevated temperatures. This effect also resulted in a significant increase in long term creep properties of the ODS alloy at 700 °C.

The stability of nano-sized oxide particles under irradiation is essential for the application of ODS steels to nuclear power plants. In our previous research [7], ion irradiation experiments of 19Cr-4.5Al ODS steel were performed at 300, 500 and 700 °C up to 20 dpa as a reference of high-Cr ODS steels. Microstructure observations revealed that a number of small dislocation loops were observed after irradiation at 300 °C, although no significant change was found for the other defects such as voids and precipitates. Furthermore, at 500 °C, no significant effects such as formation of dislocation loops, voids and secondary phases were observed. While, at 700 °C, the irradiation caused a change of the precipitation behavior, showing that carbides precipitated both in grains and on grain boundaries.

The application of advanced micro-analytical methods has shown the existence of remarkably stable dispersions of nano-sized clusters of oxygen atoms stabilized by elements such as Y and Ti in both commercial and experimental alloys [14]. The most promising performance of the ODS steels is attributed to finely dispersion of nano-sized yttria oxides with size ranging from 1 to 5 nm. They show rather high resistance to neutron irradiation up to 15 dpa at temperatures varied from 300 to 500 °C.

1.3.2.3. Issues of development of high-Cr ODS ferritic steels

For 9-12%Cr ODS ferritic steels, the most critical issue for application to SCWR and LFR is to improve their corrosion resistance. A project to develop corrosion resistant ODS steels started at Kyoto University, where surveillance tests have been carried out for “Super ODS steels [24]” to evaluate irradiation effects, corrosion resistance and stress corrosion cracking (SCC) susceptibility. It is demonstrated that high-Cr ODS steels, which have a high strength at elevated temperature and high-resistance to corrosion and irradiation embrittlement, are very promising for fuel cladding materials for SCWR and LFR as well as SFR. While long-term experiments, such as neutron irradiation experiments, creep tests, corrosion and aging tests, are necessary to assess the performance of high-Cr ODS steels as

fuel cladding of advanced nuclear systems with high efficiency and high burn-up.

A “trade-off” between corrosion resistance and aging embrittlement caused by increasing Cr content is one of the critical issues for high-Cr ODS steels [24]. Therefore, it is very important to investigate the effect of aging on high-Cr ODS steels.

1.4. Literature survey

Fe-Cr based steels are regarded as good candidates for the design of various structural components in advanced nuclear energy installations such as Generation IV and fusion reactors. However, binary Fe-Cr alloys and ferritic & F/M steels undergo Fe/Cr (α/α') phase separation if the Cr content x_{Cr} exceeds $\sim 9\%$ in the region of temperatures potentially important for technological applications ($>300\text{ }^{\circ}\text{C}$) [25-28]. The formation of nano-sized Cr-rich precipitates in the bulk during operation has long known to be the cause of the hardening and embrittlement of ferritic & F/M steels with $x_{Cr} > 14\%$ after thermal aging, as well as under irradiation, which is found to accelerate the phase-separation process at even lower temperature and Cr content [29-32]. This embrittlement, known for decades as 475 $^{\circ}\text{C}$ embrittlement, is related to the microstructural evolution occurring in the ferrite or martensite of Fe-Cr based alloys. After long-term service, loss of impact toughness and ductility is often observed, which may lead to the ruin of the component.

1.4.1. Aging effect on high-Cr ferritic alloys

Two phenomena, having their origin in the crystallographic phase diagram of the Fe-Cr systems, viz. (1) the phase decomposition (or phase separation) into the Fe-rich (α) and the Cr-rich (α') phases at $T < 500\text{ }^{\circ}\text{C}$ leads to the so-called miscibility gap, and (2) the precipitation of the σ phase that at $T > 500\text{ }^{\circ}\text{C}$ occur [33]. Both phenomena cause an enhancement of embrittlement, hence a severe deterioration of the mechanical materials properties. An interest in (1) is fourfold: (a) underlying mechanisms, (b) borders of the miscibility gap i.e. the composition of α and α' phases, (c) kinetics of the decomposition, and (d) short-range ordering (SRO). Concerning (a), two different mechanisms viz. nucleation and growth (NG) and spinodal decomposition (SD) have been proposed [34].

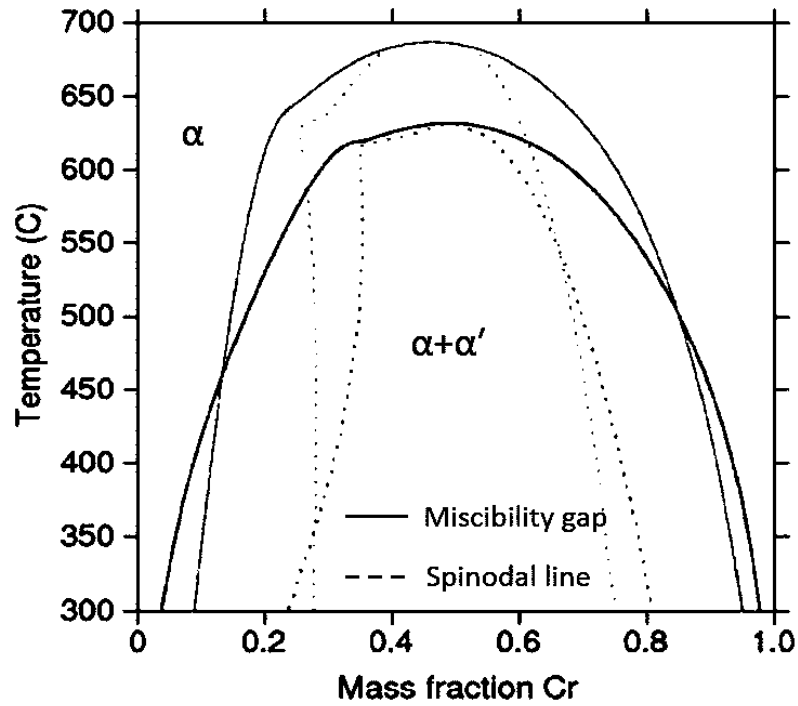


Figure 1-4 Miscibility gap of Fe-Cr systems.

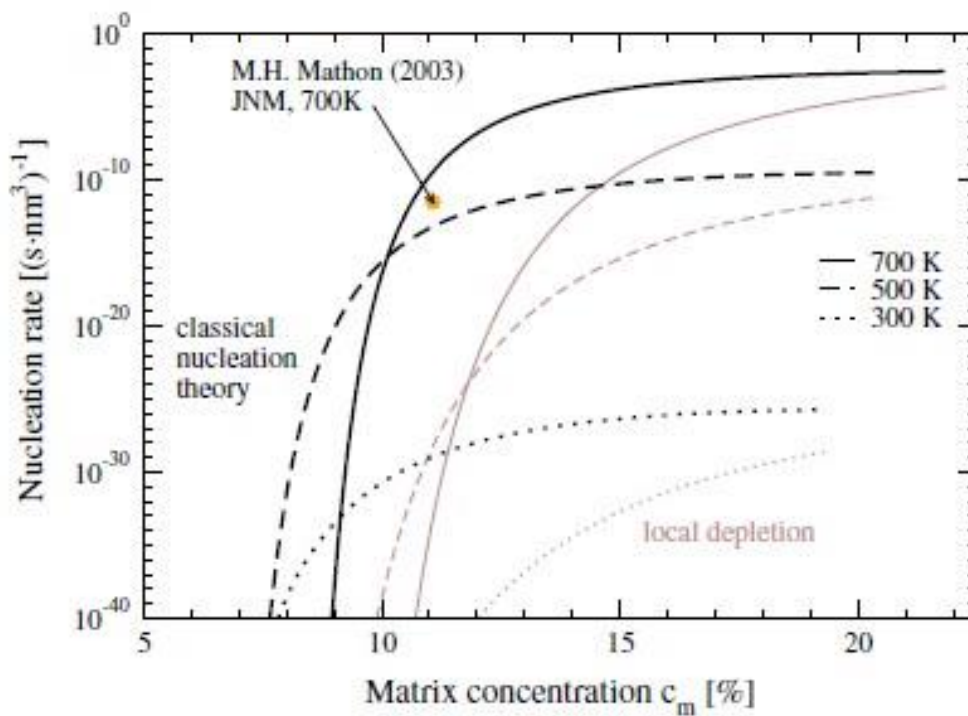


Figure 1-5 Nucleation rates pre unit volume for classical nucleation theory (black) and local depletion (gray) cases as a function of solute concentration in the matrix (c_m) at 300, 500 and 700 K.

According to calculations, the spinodal decomposition should be responsible for the decomposition of the alloys with Cr content, x , within the inner part of the miscibility gap viz. $0.2-0.3 < x < 0.75-0.8$, while the nucleation and growth for those with $x < 0.2-0.3$ and $x > 0.75-0.8$. The existence of the miscibility gap, as shown in figure 1-4, has been experimentally confirmed by using different techniques among which small-angle neutron scattering (SANS), Mössbauer spectroscopy [35] and atom probe analysis played the key role [36]. Yet, there is no unique evidence in favor of the exact position of the spinodal lines and the upper temperature limit of its existence. The borders of the miscibility gap are still not known with a good enough precision.

The phase separation process in Fe-rich Fe-Cr alloys was studied by means of the aging of a diffusion-couple formed between Fe and Fe-40 at% Cr [37]. Diffusion-couples were solution treated at 1050 °C for 3.6 ks and subsequently aged at 500 °C for 3.6-3600 ks. The EDS-SEM analysis of solution treated, water-quenched and then aged diffusion-couple permitted to obtain the equilibrium composition of miscibility gap at 500 °C to be 14 at% Cr. The high resolution (HR)-TEM analysis of the aged diffusion-couple showed that the change in size of Cr precipitates decreased with the increase in Cr content as expected by the Gibbs-Thomson effect [38].

The rate of 475 °C embrittlement increases with increasing Cr content and appears to decrease with increasing purity. D. Schwen [39] presented a calculation of the critical sizes and nucleation rates for the nucleation of α' precipitates in a Fe-Cr alloy. The resulting nucleation rates as a function of solute concentration in the matrix, c_m , are given in figure 1-5. At certain temperature, with increasing c_m , nucleation rates increase; while critical nucleus sizes decrease.

Embrittlement at 475 °C was mapped by S. Kobayashi [40] in ferritic ternary alloys with a wide composition range of Fe-(10-30) Cr-(0-20) Al (at. %) using a diffusion multiple technique. In this work, a diffusion multiple sample was fabricated by coupling pieces of Fe, Fe-Cr binary alloy and Fe-Al binary alloy. Results showed that a large solid solution of Al suppresses the 475 °C embrittlement, while a small solid solution of Al (less than 2 at. %) promotes embrittlement. It was shown that the age-hardening was negligible when the Al content was greater than 10 and 11 at. % and the Cr content was 12.5 and 15.0 at. %. TEM

observations on aged samples suggest that suppression of the embrittlement due to Al addition can be attributed to the suppression of phase separation of the ferrite phase into α and α' phases.

T. Angeliu et al. [41] have investigated the long-term (up to 50k h) aging embrittlement of Fe-12Cr steels below 500 °C. Results showed that, after aging at 450 °C, conventional M152 contained large quantities of α' phase in addition to Cr-rich $M_{23}C_6$ carbides and complex Cr-Fe-Mo-Ni-Si-rich precipitates. The degradation in the toughness of M152 is primarily due to the combination of α' phase formation and Sn segregation. They concluded that improvements in the long-term aging embrittlement resistance required ultralow levels of harmful elements, especially Sn, and a reduction of Cr content to prevent α' phase formation.

Atomistic simulations [42] were carried out by D.A. Terentyev to study the interaction of dislocation with Cr precipitate in body-centered cubic (BCC) Fe and Fe-10%Cr at 0 K. Generally, precipitation strengthening is the consequence of dislocations being pinned by a row of precipitates. Models based on the assumption of different mechanisms, namely size misfit strengthening (SMS), chemical strengthening (CS) and modulus misfit strengthening (MMS), are of use in the case of pure, coherent precipitates. Neither of the above models accounts for the important effect of self-interaction between the two dislocation arms that emerge from the precipitate, if the critical angle is close to zero, while an expression derived from continuum model simulation by Scattergood and Bacon (SB) accounts for this effect. For large precipitates (with diameter above 3 nm), there is a good agreement with the atomistic data using the SB model. It is shown that solute hardening (in Fe-Cr matrix) and precipitate hardening can be considered, as a good approximation, to be additive effects.

1.4.2. Aging effect on high-Cr ODS ferritic steels

One of the common key issues for the use of high ODS ferritic steels as structural material for advanced fission and fusion nuclear systems, is to improve its fracture toughness, as it is lower than conventional ferritic steels. Until now, there are few reports [43-48] about thermal aging effect on high-Cr ODS steels, particularly for the range of compositions (<20 wt. % Cr).

Effect of α - α' phase separation on notch impact behavior of ODS Fe20Cr5Al alloy has been studied by J. Chao [43], who showed that a significant increase in ductile-brittle transition temperature (DBTT) and decrease in upper shelf energy (USE) were recorded due to α - α' phase separation with an apparent activation energy measured in the range of 214-240 KJ/mol. The aging embrittlement is associated generally with intergranular failure that arises from the grain boundary segregation and precipitation of arrays of coarse yttrium-aluminum garnets (YAGs) along the extrusion direction and the consequent loss of grain boundary cohesion. These arrays of oxides shift the DBTT to higher temperatures and play an important role in the non-hardening embrittlement. They reported that the morphology of brittle features in the ODS ferritic steels depended on not only oxide morphology and distribution, but also microstructural factors, such as microtexture, effective grain size, and plastic anisotropy.

Effect of aging on DBTT behavior of recrystallized high-Cr ODS ferritic steels were investigated using small-punch test [44]. ODS steels were recrystallized and cold rolled to reduce the anisotropy. The ODS steel without Al hardly recrystallized at 1200 °C for 90 min, while the ODS steel with Al significantly recrystallized. Aging at 450 °C for 1440 h degraded the impact properties of ODS steel with Al, while no degradation occurred for the ODS steel without Al.

Further studies [45] by atom probe tomography (APT) showed that the age-hardening of PM2000 ODS alloy was found to be linear dependent on the chromium content of the α' regions, as shown in figure 1-6. The APT has been shown to be an effective technique to study the ultrafine scale phase separation because it provides both atomic scale microstructure and micro-chemical analysis of the observed phases. The APT results revealed that both the scale and concentration amplitude of the α' regions increase with aging time. The aluminium and titanium were found to be preferential partition to the iron-rich α phase, as shown in figure 1-7. The hardness values reach a plateau at ~1000 h for PM2000; the time to reach maximum hardness was significantly shorter than that observed during the isothermal annealing of an Fe-30% Cr binary alloy at 470 °C [46]. However, APT can only reveal quite small fraction of the material and is often hard to illustrate the microstructure changes.

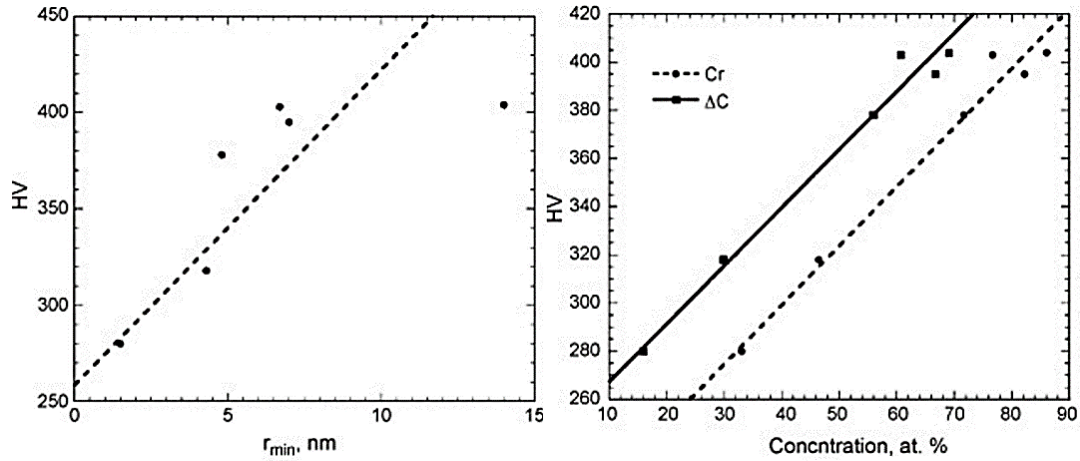


Figure 1-6 A linear relationship between hardness and the size and chromium content of the α' phase and composition amplitude, ΔC .

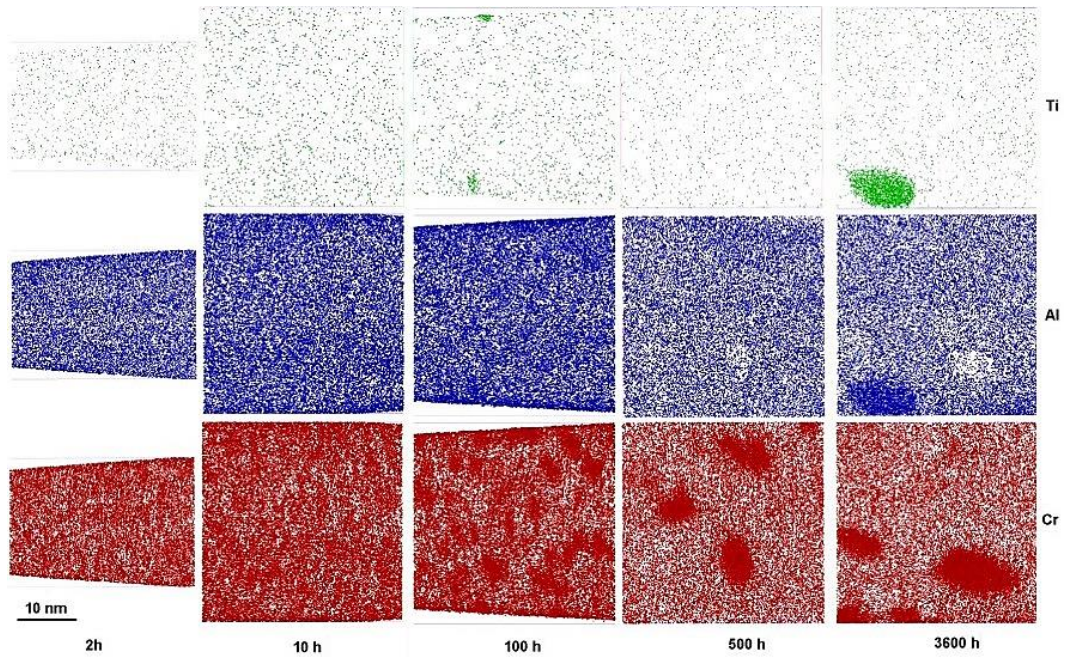


Figure 1-7 Atoms map of PM 2000TM after aging at 748 K showing the evolution of the Cr-enriched and Al-depleted α' phase and a Ti- and Al-enriched phase.

The effects of thermal aging treatment on the microstructural stability and mechanical property changes of ODS steels, which were produced by varying Cr contents from 14 to 22 wt.% but keeping yttria contents within 0.36-0.38 wt.%, were investigated by using microhardness and small punch (SP) tests [47]. Results showed that SP-ductile to brittle

transition temperature and microhardness were significantly increased as a function of Cr contents, aging time and temperature, as presented in figure 1-8.

The generalized hardening formula (1.4) as a function of Cr, aging temperature and time was obtained as follow:

$$\Delta H_v = (23.7Cr - 3.02) \times T(20 + \log t) \times 10^{-3} - (34.8Cr - 31.5) \quad (1.4)$$

where T is the aging temperature [K] ($703 \leq T \leq 748$), t is the aging time [hour] ($5 \leq t \leq 1000$), and Cr is the weight percent of chromium ($14 \leq Cr \leq 22$).

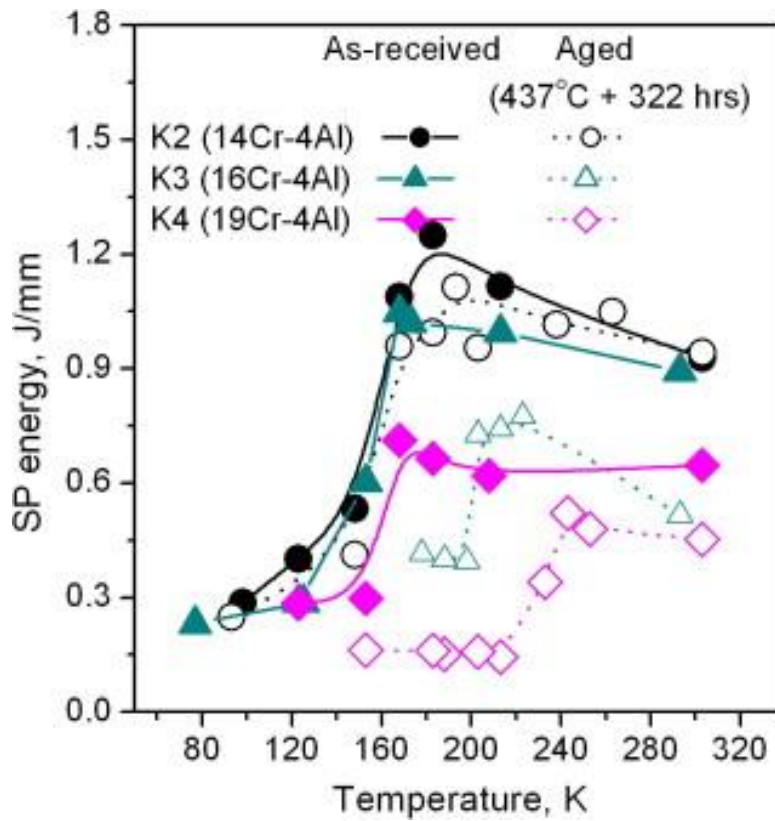


Figure 1-8 Effects of thermal aging treatment on the specific SP energy of the ODS steels as a function of test temperature, for samples thermally aged at 437 °C for 322 h.

Influence of recrystallization on phase separation kinetics of Al added ODS alloy was investigated by C. Capedvila [48] using APT and thermo-electric power (TEP) measurements. A low volume fraction (below 10%) of coarse, incoherent precipitates has a negligible influence on the TEP, whereas coherent and semi-coherent precipitates, such as the α' phase, may have a strong intrinsic effect on the TEP of the alloy. The results revealed that the high

recrystallization temperature necessary to produce a coarse grained microstructure in Fe-base ODS alloys affects the randomness of Cr-atom distributions and defect density, which consequently affect the phase separation kinetics at low annealing temperatures.

Figure 1-9 shows TEM micrographs of 19Cr-ODS steel observed before and after aging at 500 °C for 1000 h [19]. At as-received condition, fine oxide particles were observed in the matrix, while many larger structures as well as oxide particles were observed after the aging. Since the diffraction patterns of the aged samples did not show any extra spots besides oxide particles, the structures were estimated to be Cr-rich phases which had BCC structure with almost similar lattice parameter to iron. However, it's an issue to characterize Cr-rich phases in ODS steels.

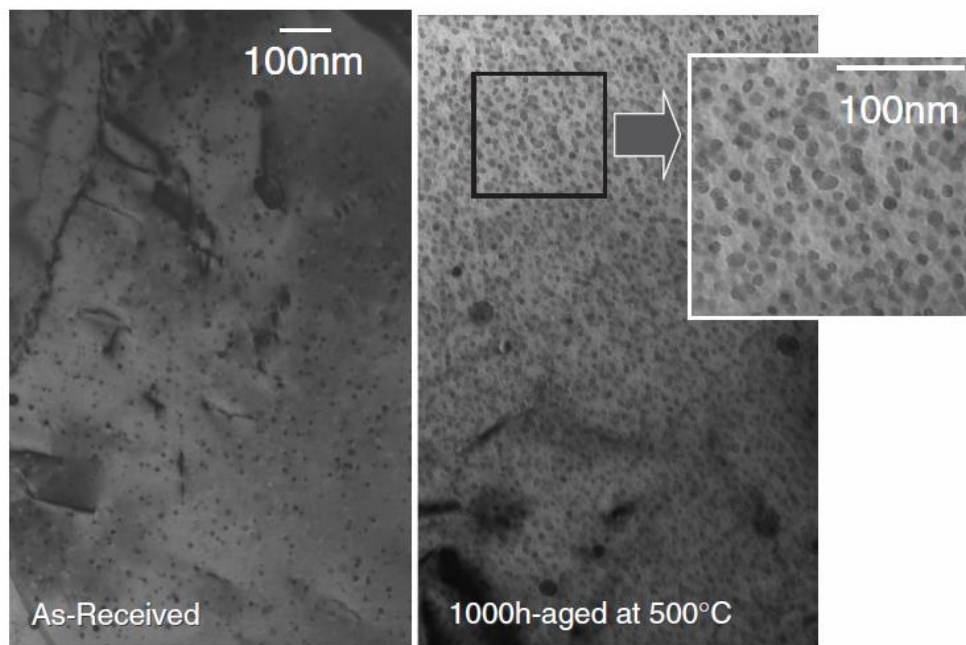


Figure 1-9 TEM micrographs of 19Cr-ODS steel observed before and after aging at 500 °C for 1000 h [19].

1.5. Objectives of this research

As described above, ODS ferritic steels are candidate structural materials for advanced GEN-IV fission and fusion reactors. The high-Cr ODS steels have good performances, such as high resistance to irradiation embrittlement and hydrogen embrittlement, high resistance to corrosion in supercritical pressurized water, and high strength at elevated temperature. Since ODS steels have been developed for the use of high temperature applications in the range from ~400 to 700 °C, they will inevitably experience thermal aging related problems at prolonged service times.

475 °C aging embrittlement is critical for the application of high-Cr ODS steels for advanced nuclear systems. It is well known that thermal aging of high Cr ferritic steels can result in the formation of Cr-rich phases, which harden the steels and make them brittle at room temperature and unsuitable for many engineering applications. Therefore, long-term aging tests are necessary to assess the performance of high-Cr ODS steels as fuel cladding of advanced nuclear systems with high efficiency and high burn-up.

Until now, few studies provide the microstructure evolution of Cr-rich phase and quantitative research of Fe/Cr phase decomposition on age-hardening in high Cr ferritic alloys with Cr content below 18 wt. %, especially in ODS ferritic steels. In addition, there has been few reports about the effects of alloying elements, such as C, Si, Mn and Ni on the age-hardening of high Cr ferritic steels. Nevertheless, no research has been done to investigate the roles of oxide particles in age-hardening behavior of ODS ferritic steel. Detailed information concerning the change in tensile strength and microstructure, especially Cr-rich phases, and factors affecting age-hardening in high-Cr ODS steels are still unclear.

In this research, therefore, the effects of long-term thermal aging on microstructure and mechanical properties of high Cr ODS ferritic steels are investigated with focusing on the Fe/Cr phase decomposition characteristic, alloying elements effect and roles of oxide particles in the age-hardening/embrittlement behavior.

References

- [1] International energy outlook 2014, <http://www.eia.gov/forecasts/aeo>
- [2] International energy outlook 2014, <http://www.eia.gov/forecasts/ieo/pdf/04>
- [3] Generation IV international forum web site, <http://www.gen-4.org/technology>
- [4] P. Yvon, F. Carre, “Structural materials challenges for advanced reactor systems”, *J. Nucl. Mater.*, **385** (2009) p. 217-222
- [5] P. Norajitra, L. buhler, U. Fischer, S. Gordeev, S. Malang, G. Reimann, “Conceptual design of dual-coolant blanket in the frame of the EU power plant conceptual study”, *Fusion Eng. Des.*, **69** (2003) p. 669-673
- [6] N. Baluc, K. Abe, J.L. Boutard, V.M. Chernov, E. Diegele, S. Jitsukawa, A. Kimura, R.L. Klueh, A. Kohyama, R.J. Kurtz, R. Lasser, H. Matsui, A. Moslang, T. Moroga, G.R. Odette, M.Q. Tran, “Status of R&D activities on materials for fusion power reactors”, *Nucl. Fusion*, **47** (2007) p. 696.
- [7] A. Kimura, R. Kasada, N. Iwada, H. Kishimoto, C.H. Zhang, J. Isselin, P. Dou, J.H. Lee, N. Muthukumar, T. Okuda, M. inoue, S. Ukai, S. Ohnuki, T. Fujisawa, T.F. Abe, “Development of Al added high-Cr ODS steels for fuel cladding of next generation nuclear systems”, *J. Nucl. Mater.*, **417** (2011) p. 176-179
- [8] C. Zener, as quoted by C.S. Smith, *Trans. Am. Inst. Mech. Eng.*, **175** (1948) p. 47
- [9] J.W. Martin, R.D. Doherty, “Stability of microstructure in metallic systems”, *Cambridge University Press, Cambridge*, (1976) p. 298
- [10] I. Shibahara, “Development of in-core materials for fast breeder reactors”, *Radiat. Eff. Defects Solids*, **144** (1998) p. 233
- [11] A. Kohyama, A. Hishinuma, D.S. Gelles, R.L. Klueh, W. Dietz, K. Ehrlich, “Low activation ferritic and martensitic steels for fusion application”, *J. Nucl. Mater.*, **233-237** (1996) p. 138-147
- [12] S. Ukai, M. Fujiwara, “Perspective of ODS alloys application in nuclear environments”, *J. Nucl. Mater.*, **307-311** (2002) p. 749
- [13] R.H. Jones et al., “Promise and challenges of SiC_f/SiC composites for fusion energy applications,” *J. Nucl. Mater.*, **307-311** (2002) p.1057-1072

- [14] M.K. Miller, K. F. Russell, D.T. Hoelzer, "Characterization of precipitates in Ma/ODS ferritic alloys", *J. Nucl. Mater.*, **351** (2006) p. 261-268
- [15] Shigeharu Ukai, Toshio Nishida, Hirokazu Okada, "Development of oxide dispersion strengthened ferritic steels for FBR core application, (I) Improvement of mechanical properties by recrystallization processing", *J. Nucl. Sci. Technol.*, **34** (1997) p. 256-263
- [16] Shigeharu Ukai, Toshio Nishida, Takanari Okuda, Tunemitsu Yoshitake, "Development of oxide dispersion strengthened ferritic steels for FBR core application, (II) Morphology improvement by martensite transformation", *J. Nucl. Sci. Technol.*, **35** (1998) p. 294-300
- [17] T. Yoshitake, T. Ohmori, S. Miyakawa, "burst properties of irradiated oxide dispersion strengthened ferritic steel claddings", *J. Nucl. Mater.*, **307-311** (2002) p. 788-792
- [18] A. Kimura, S. Ukai, M. Fujiwara, "R&D of oxide dispersion strengthening steels for high burn-up fuel claddings", *Proc. Int. Cong. Advances in Nuclear Power Plants, (ICAPP-2004) ISBN: 0-89448-680-2, CD-ROM file*, (2004) p. 2070-2076
- [19] Akihiko Kimura, Han-Sik Cho, Naoki Toda, Ryuta Kasada, Kentaro Yutani, Hirotsu Kishimoto, Noriyuki Iwata, Shigeharu Ukai, Masayuki Fujiwara, "High burn-up fuel cladding materials R&D for advanced nuclear systems: Nano-sized oxide dispersion strengthening steels", *J. Nucl. Sci. and Tech.*, **44** (2007) p. 323-328
- [20] H.S. Cho, A. Kimura, S. Ukai, M. Fujiwara, "Corrosion properties of oxide dispersion strengthened steels in super-critical water environment", *J. Nucl. Mater.*, **329-333** (2004) p. 387-391
- [21] P. Dou, A. Kimura, R. Kasada, T. Okuda, M. Inoue, S. Ukai, S. Ohnuki, T. Fujisawa, F. Abe, "TEM and HRTEM study of oxide particles in an Al-alloyed high-Cr oxide dispersion strengthened steel with Zr addition", *J. Nucl. Mater.*, **444** (2014) p. 441-453
- [22] R. Gao, T. Zhang, X.P. Wang, Q.F. Fang, C.S. Liu, "Effect of zirconium addition on the microstructure and mechanical properties of ODS ferritic steels containing aluminum", *J. Nucl. Mater.*, **444(1)** (2014) p. 462-468
- [23] A. Kimura, R. Kasada, N. Iwata, J. Isselin, P. Dou et al., in: Proceeding of International Workshop on 2nd Structural Materials for Innovative Nuclear Systems, OECD Nuclear Energy Agency, *J. Nucl. Mater.*, **417** (2009) p. 896-899

- [24] A. Kimura, R. Kasada, N. Iwata, H. Kishimoto, C.H. Zhang et al., “Super ODS steels R&D for fuel cladding of next generation nuclear systems: 1) Introduction and alloy design”, *Proceedings in ICAPP*, Tokyo, (2009) p. 9220
- [25] G.E. Lucas, “The Evolution of Mechanical Property Changes in Irradiated Austenitic Stainless Steels”, *J. Nucl. Mater.*, **206** (1993) p. 287-305
- [26] P.J. Grober, “The 885 °F (475 °C) embrittlement of ferritic stainless steels”, *Metall. Trans.*, **4** (1973) p. 251-260
- [27] T.J. Nichol, A. Datta, G. Aggen, “Embrittlement of ferritic stainless steels”, *Metall Trans. A*, **11A** (1980) p. 573-585
- [28] G. Bonny, D. Terentyev, L. Malerba, D. Van Neck, “Early stages of α - α' phase separation in Fe-Cr alloys: An atomistic study”, *Phys. Rev. B*, **79** (2009) p. 104-207
- [29] P.J. Grobner, R.F. Steigerwald. “Effect of cold work on the 885 °F (475 °C) embrittlement of 18Cr-2Mo ferritic stainless steels”, *J. Metals*, **29** (1977) p. 17-23
- [30] G.R. Odette, M.J. Alinger, B.D. Wirth, "Recent Developments in Irradiation Damage Resistant Steels", *Annu. Rev. of Mater. Res.*, **38** (2008) p. 471
- [31] F. Danoix, P. Auger, “Atom probe studies of the Fe-Cr system and stainless steels aged at intermediate temperature: a review”, *Mater. Charact.* **77** (2000) p. 177-201
- [32] S. Novy, P. Pareige, C. pareige, “Atomic scale analysis and phase separation understanding in a thermally aged Fe-20 at. %Cr alloy”, *J. Nucl. Mater.*, **384** (2009) p. 96-102
- [33] M.E. Wilms, J.M. Krougman, F.P. Jsseling, “The effect of σ -phase precipitation at 800°C on the corrosion resistance in sea-water of a high alloyed duplex stainless steel”, *Corros. Sci.*, **36** (5) (1994) p. 871-881
- [34] J.C. Lasalle, L.H. Schwartz, “Further studies of spinodal decomposition in Fe-Cr”, *Acta Metall.*, **24** (1986) p. 989-1000
- [35] D. Chandra, L.H. Schwartz, “Mossbauer effect study of the 457 °C decomposition of Fe-Cr”, *Mat. Trans.*, **2** (1971) p. 511-519
- [36] P. Auger, F. Danoix, A. Menand, S. Bonnet, J. Bourgoïn, M. Guttman, “Atom probe and transmission electron microscopy study of aging of cast duplex stainless steels”, *Mater. Sci. technol.*, **6** (1990) p. 301-313

- [37] Victor M. Lopez-Hirata, Nicolas Cayetano-Castro et al., “Phase separation in aged diffusion-couples Fe/Fe-40 at% Cr alloy”, *Mater. Trans.*, **12** (2011) p. 2155-2158
- [38] F. Hernandez-Santiago, V.M. Lopez-Hirata, M.L. Saucedo-Munoz, H.J. Dorantes-Rosales, “Gibbs-Thomson relationship for the precipitation in Cu-Ti alloys”, *Mater. Charact.*, **58** (2007) p. 303-306
- [39] D. Schwen, E. Martinez, A. Caro, “On the analytic calculation of critical size for alpha prime precipitation in FeCr”, *J. Nucl. Mater.*, **439** (2013) p. 180-184
- [40] S. Kobayashi, T. Takasugi, “Mapping of 475 °C embrittlement in ferritic Fe-Cr-Al alloys”, *Scripta Mater.*, **63** (2010) p. 1104-1107
- [41] T. Angeliu, R.L. Hall, M. Larsen, A. Linsebigler, C. Mukira, “The long-term aging embrittlement of Fe-12Cr steels below 773 K”, *Metall. Mater. Trans. A*, **34A** (2003) p. 927-934
- [42] D.A. Terentyev, G. bonny, L. Malerba, “Strengthening due to coherent Cr precipitates in Fe-Cr alloys: Atomistic simulations and theoretical models”, *Acta Mater.*, **56** (2008) p. 3229-3235
- [43] J. Chao, C. Capdevila, M. Serrano, A. Garcia-Junceda, J.A. Jimenez, M.K. Miller, “Effect of α - α' phase separation on notch impact behavior of oxide dispersion strengthened (ODS) Fe₂₀Cr₅Al alloy”, *Mater. Des.*, **53** (2014) p. 1037-1046
- [44] J. Isselin, R. Kasada, A. Kimura, T. Okuda, M. Inoue, S. Ukai, S. Ohnuki, T. Fujisawa, F. Abe, “Evaluation of fracture behavior of recrystallized and aged high-Cr ODS ferritic steels”, *J. Nucl. Mater.*, **417** (2011) p. 185-188
- [45] C. Capdevila, M.K. Miller, K.F. Russell, J. Chao, J.L. Gonzalez-Carrasco, “Phase separation in PM2000TM Fe-base ODS alloy: Experimental study at the atomic level”, *Mater. Sci. Eng. A*, **490** (2008) p. 277-288
- [46] S.S. Brenner, M.K. Miller, W.A. Soffa, “Spinodal decomposition of iron- 32 at.% chromium at 470°C”, *Scripta Metall.*, **16** (1982) p. 831-836
- [47] J.S. lee, C.H Jang, I.S. Kim, A. Kimura, “Embrittlement and hardening during thermal aging of high Cr oxide dispersion strengthened alloys”, *J. Nucl. Mater.*, **367-370** (2007) p. 229

[48]C. Capdevila, M.K. Miller, G. Pimentel, J. Chao, “Influence of recrystallization on phase separation kinetics of oxide dispersion strengthened Fe-Cr-Al alloy”, *Scripta Mater.*, **66** (2012) p. 254-257

Chapter 2

Effects of Alloying Elements on Age-hardening Behavior of Fe-15Cr Alloys

2.1. Introduction

The 475 °C embrittlement is well known to occur in ferritic, dual phase and ferritic/martensitic stainless steels with chromium contents higher than ~12wt.% [1-3]. Aging embrittlement is always attributed to the phase decomposition of ferrite to iron-rich ferrite (α) and chromium-rich ferrite (α') phases [4, 5]. While, the effects of alloying elements on the embrittlement of high-Cr ferrite steels are still unclear.

There are some reports on alloying effect on aging embrittlement of high-Cr ferritic steels. According to Mueller [6], who investigated the effect of varying carbon contents on the impact energy of Fe-17wt.% Cr alloys, and they reported that there was a small increase in DBTT and significant decrease in upper shelf energy as the carbon content increased. The embrittling effect of interstitials may be controlled by the addition of stabilizing elements, such as titanium, niobium, zirconium and tantalum. Grobner [2] believes that the addition of stabilizers (e.g. Ti and Nb) slow down the aging process, while Courtinall and Pickering [7] reported that Ti and Nb also increased the rate of α' precipitation. The amount of stabilizer added is critical, since above a certain level they will cause the toughness to decrease [8, 9].

Trindade and Vilar [10] reported that the ferrite decomposition was more pronounced after aging at 475 °C with the addition of 2-4 wt.% Ni to Fe-25Cr and Fe-45Cr. Solomon and Levinson [11] studied a series of duplex and single phase ferritic alloys to investigate the effects of Ni, Cu, Si, Mn and Mo on the phase separation via Mössbauer spectroscopy and transmission electron microscopy. They found that both Ni and Cu promote phase separation, but no effects of Mn, Si, and Mo on the phase separation kinetics could be found. Courtinall and Pickering [12], however, did report that the addition of 0.96 wt.% Mo to a ferritic steel with 25 wt.% Cr did increase the rate of phase separation.

However, the effect of simultaneous additions of carbon and alloying elements on the 475 °C embrittlement is still not thoroughly understood. Limited data are available for the thermal aging effect on mechanical properties and the microstructural changes of Fe-15wt.% Cr alloys with focusing on the impurity and alloying effects. In this study, the effects of both alloying elements and carbon on age-hardening behavior of Fe-15Cr alloys have been investigated.

2.2. Experimental

2.2.1. Materials

The materials used in this study were three kinds of Fe-15Cr alloys, named Fe-15Cr, Fe-15Cr-C and Fe-15Cr-Xs, where Xs refers to Si, Mn and Ni to simulate a ferritic steel. The fabrication process of arc-melted Fe-15Cr alloys is shown in figure 2-1. High purity Fe and Cr metals (>99.99%) were first melted in an arc-melting furnace at a high vacuum ($\sim 8 \times 10^{-4}$ Pa). To homogenize the distribution of alloying elements, the normalizing treatment was performed at 1100 °C for 72 h, and then the button ingots were cold rolled with an area reduction of 80%. The cold-worked specimens were annealed at 900 °C for 2h followed by ice water quenching. According to ideal Fe-Cr phase diagram, as shown in figure 2-2, we can get a single α phase after the above fabrication process. While for Fe-15Cr-C alloy, one more process was to prepare Fe-C pre-alloy by arc-melting because controlling carbon content is quite difficult. After analyzed the carbon content, the Fe-C alloy together with other metals were arc-melted using the same fabrication process, as presented in figure 2-1. The final compositions of these alloys are shown in Table 2-1.

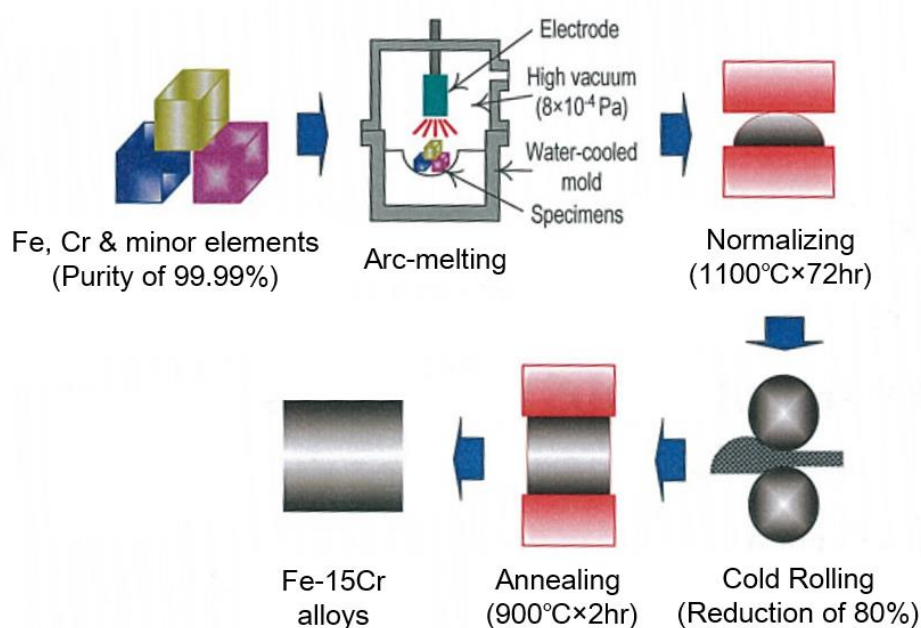


Figure 2-1 Fabrication process of Fe-15Cr alloys prepared by vacuum arc-melting.

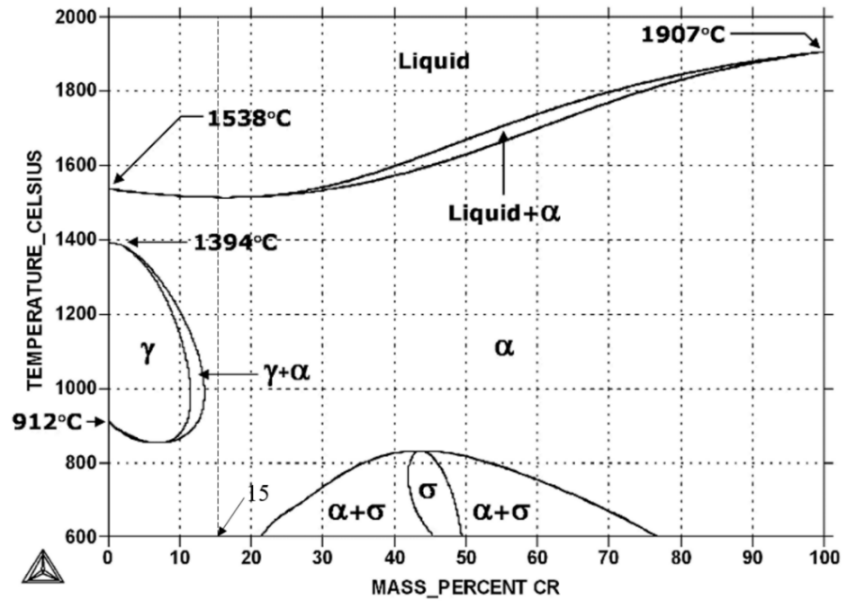


Figure 2-2 Fe-Cr phase diagram in ideal condition.

Table 2-1 Chemical compositions of Fe-15Cr alloys (wt.%).

Material	Cr	C	Mn	Si	Ni	Fe
Fe-15Cr	14.55	0.001	-	-	-	Bal.
Fe-15Cr-C	14.83	0.022	-	-	-	Bal.
Fe-15Cr-Xs	14.96	0.002	0.83	0.51	0.49	Bal.

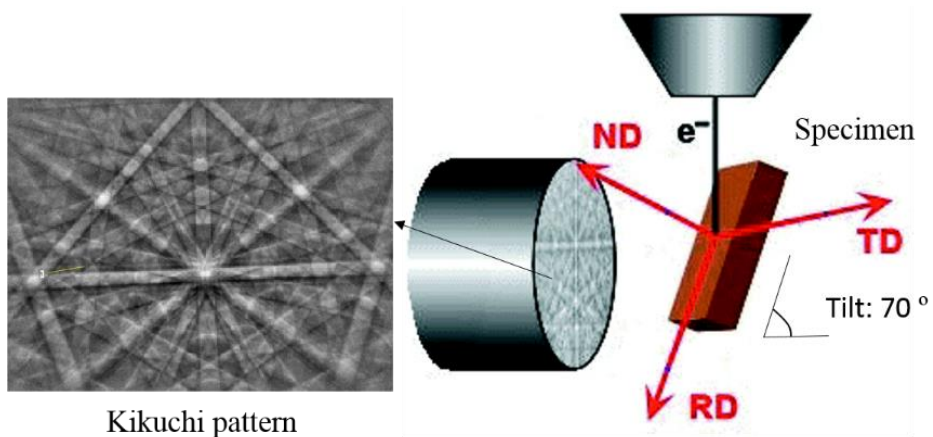


Figure 2-3 Electron backscattering diffraction pattern (EBSD) system.

2.2.2. Microstructural observation

Specimens for microstructural observation were mechanically polished with a wet grinder using 800, 1200 and 2400 emery SiC papers. And then they were buff-polished with diamond paste in order of 6, 3, 1 and 0.25 μm diameters. Finally, colloidal silica (0.04 μm) polishing was performed [13].

The grain morphology was examined by the optical microscopy (BX51M, OLYMPUS OPTICAL co., Japan). Before optical microscopy (OM) observation, the samples were etched with a metallographic erosion liquid ($\text{CH}_3\text{COOH} : \text{HNO}_3 : \text{HCl} = 1 : 1 : 3$) for 10~12 seconds.

Disk-type specimens of 3 mm diameter for transmission electron microscopy (TEM) observation were punched out from a 0.3 mm thick plate and mechanically grounded to about 100 μm in thickness. Final TEM specimens were prepared by electrolytic polishing with HClO_4 and CH_3OH (1:9) using a twin-jet polisher at a voltage of 20 V at room temperature. Before TEM observation the oxide layer was removed by the argon ion beam milling using a Gentle milling machine. The grain boundaries and precipitates were by examined by the TEM (JEM 2010, JEOL co., Japan) and FE-TEM (JEM 2200FS, JEOL co., Japan) with an acceleration voltage of 200 kV.

The ruptured surface after tensile testing was observed by the scanning electron microscope (SEM) (VE-9800, KEYENCE co., Japan). Electron backscattering diffraction pattern (EBSD, Ultra-55, Zeiss co., Germany) technique was employed to analyze the rupture manner and phase characterization. EBSD is known as an electron backscatter diffraction method for lattice structure determination using the Kikuchi pattern induced by back-scattered X-ray. To collect these patterns, the same sample is tilted in SEM to approximately 70° as presented in figure 2-3. The observed surface is TD-RD surface, where the orientation of tensile specimens is defined as: RD (rolling direction), TD (transverse direction) and ND (normal direction). The collected data was analyzed by TEL OIM software.

2.2.3. Hardness measurements and tensile tests

The hardness measurements were performed using a Micro Vickers Hardness tester (HM-102, Akashi co. Japan), which has a square-based diamond-pyramid indenter with an included angle of 136° between opposite faces. The load range is usually between 1~50 kgf, meanwhile, it is between 0.05~1000 gf in the case of micro Vickers hardness measurement. Due to the shape of the indenter, an impression on the surface of the specimen will be a square. The Vickers hardness, H_v , can be expressed as:

$$H_v = (2P/d^2) \sin(\theta/2) = 1.8544 P/d^2 \quad (2.1)$$

In current study, micro Vickers hardness was measured with a load of 1kgf for 10 seconds. At least ten measurements were obtained and averaged. The surface of samples for hardness measurements was finally polished with a diamond paste of $1\mu\text{m}$.

Miniaturized tensile tests were performed at room temperature using a tensile test machine (205XK-KC, INTESCO co. Japan). Tensile samples were punched from a 0.3 mm thick plate paralleling to cold-rolling direction and mechanically ground to about 0.25 mm in thickness. The surface of specimens for tensile tests was finally polished using a 2400 emery SiC paper. The dimensions of tensile specimens are 16 mm length \times 4 mm width \times 0.25 mm thickness, as shown in figure 2-4.

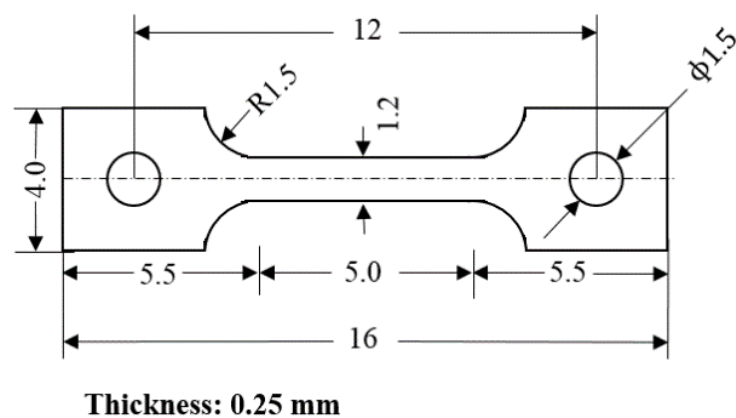


Figure 2-4 Specimen geometries for miniaturized tensile tests.

2.2.4. Thermal aging condition

Figure 2-5 shows the sketch map of thermal aging experimental details and process. All the samples were punched from TD-RD plane. Some specimens for thermal aging experiments were sealed in ampoules in high vacuum conditions (10^{-4} Pa) and isothermally aged at 475 °C for up to 10,000 h. 475 °C is chosen as aging temperature because age-hardening will be most remarkable at this temperature [2]. After thermal aging, samples were taken out from isothermal furnace and quenched immediately into iced water. Before and after aging, microstructure and mechanical properties, such as microhardness and room temperature tensile properties, were evaluated to investigate the effect of alloying elements on age-hardening behavior of Fe-15Cr alloys.

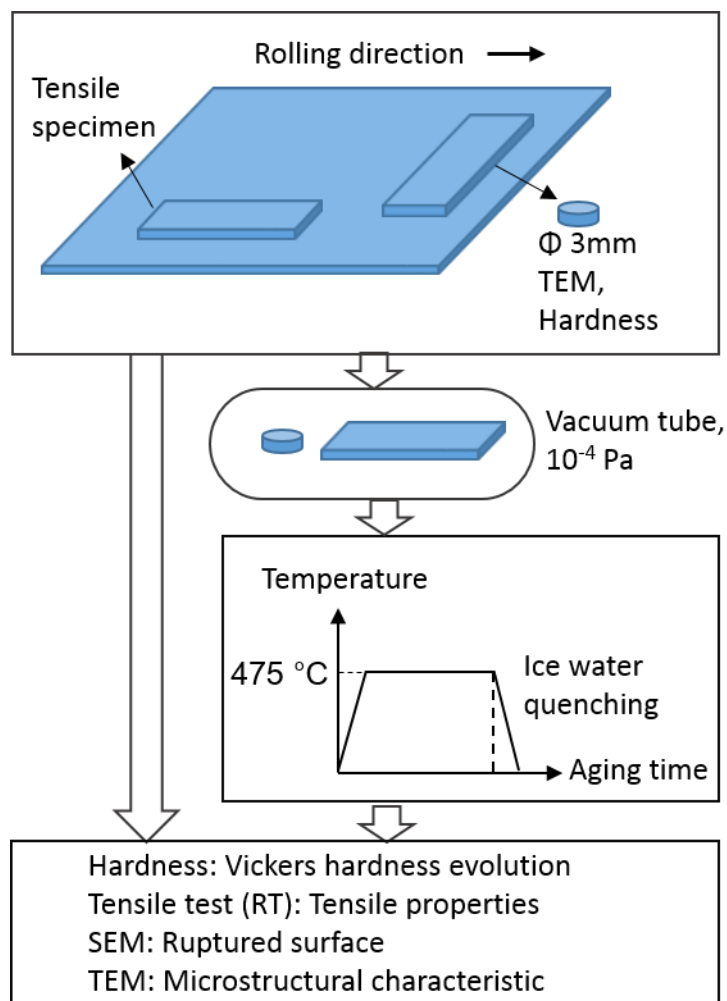


Figure 2-5 Sketch map of thermal aging experimental details and process.

2.3. Results

2.3.1. Microstructural changes

2.3.1.1. Alloying effect

Figure 2-6 provides the metallographic microstructures of Fe-15Cr alloys fabricated by arc-melting. For the pure Fe-15Cr alloy, the average grain size is about 200 μm . With the addition of carbon, the average grain size becomes much smaller ($\sim 30 \mu\text{m}$). With the addition of Mn, Si and Ni, grain refining can also be observed; while, other than ferritic phase, there are some other phases along grain boundaries and in matrix of Fe-15Cr-Xs.

TEM was used to examine grain boundaries and precipitates as well as phase structure. There is almost no precipitates in un-aged Fe-15Cr and Fe-15Cr-C, as presented in figures 2-7(a) and 2-7(b). In contrast, the addition of Mn, Si and Ni leads to some lath shaped structures in the ferrite matrix of Fe-15Cr-Xs, as shown in figure 2-7(c). In addition, a large number of dislocation can be observed in these structures or along their interfaces with ferrite.

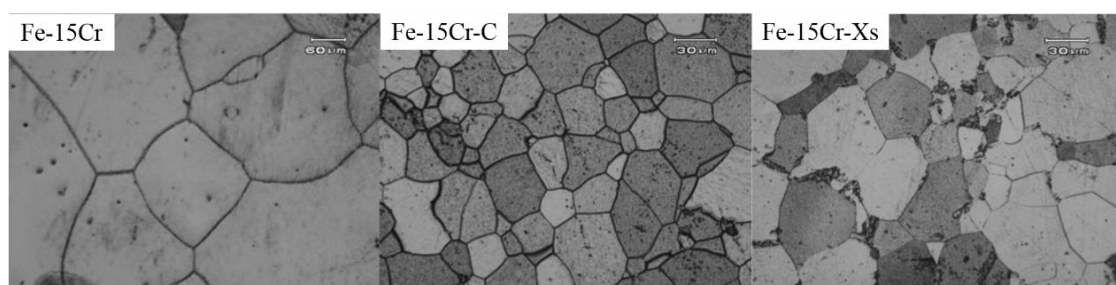


Figure 2-6 Metallographic microstructures of Fe-15Cr alloys fabricated by arc-melting.

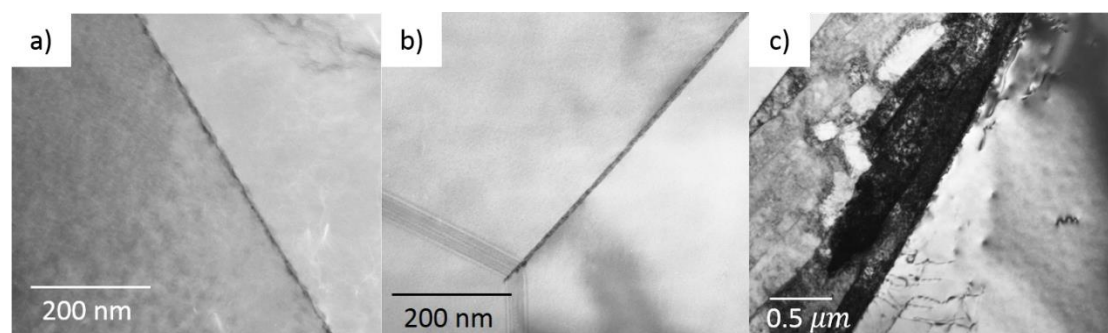


Figure 2-7 Transmission electron microscopy bright field images of (a) Fe-15Cr, (b) Fe-15Cr-C, and (c) Fe-15Cr-Xs, before thermal aging.

2.3.1.2. Thermal aging effect

Figures 2-8(a-i) provide the microstructural evolution of Fe-15Cr alloys during aging at 475 °C. After aging, many different precipitates can be observed both in the matrix and on the grain boundaries of each alloy after aging. The precipitation morphology, such as, the size and number density depends on the aging period, and the TEM observation results are summarized in Table 2-2.

Table 2-2. Summary of the TEM microstructural observation results.

Material	Aging at 475 °C for 500 h		Aging at 475 °C for 2000 h		
	Carbides	α'	Carbides	α'	G phase
Fe-15Cr	Less Fe ₂ C, M ₂₃ C ₆	quite few	M ₂₃ C ₆	yes	no
Fe-15Cr-C	Fe ₂ C, M ₂₃ C ₆	yes	M ₂₃ C ₆	yes	no
Fe-15Cr-Xs	Less M ₂₃ C ₆	yes	M ₂₃ C ₆	yes	less

For pure Fe-15Cr, even a trace amount of carbon (~0.001wt. %) can lead to some needle-like precipitates formed nearby grain boundaries and large precipitates on grain boundaries after aged for 500 h, as shown in figure 2-8(a).

To know the composition information about the precipitates, TEM energy dispersive X-ray (EDX) line analyses were used. Figure 2-9(a) and 2-9(b) provide the EDX line analysis of one grain boundaries (GB) precipitate in Fe-15Cr aged for 2000 h and the chemical components of the precipitate and the nearby matrix. Three points analysis was performed to obtain relative compositions of the precipitates. Results indicate that these precipitates on grain boundaries are Cr enriched M₂₃C₆ carbides. The needle-like precipitates are expected to be ϵ -Fe₂C carbides [14], which become coarsening after aging for 2000 h, as shown in figure 2-8(g).

In addition, after aging for 2000 h, there is a uniform distribution of spherical-shaped precipitates, of which the wavelength of decomposition is ~5-8 nm, in the matrix of Fe-15Cr. H. Peter and. B. Saeed [15] investigated the Fe/Cr phase decomposition in the binary Fe-Cr system and they found a modulated structure in Fe-25 wt. % Cr alloy after 1000 h of aging.

Therefore, it seems like that these spherical-shaped precipitates in Fe-15Cr alloy are Cr-rich (α') phase caused by Fe/Cr phase decomposition. However, the formation of α' phase in Fe-15Cr alloy during aging at 475 °C seems via nucleation and growth of α' particles, other than spinodal decomposition. Figure 2-8(b) shows the microstructure of the sample Fe-15Cr-C aged for 500 h. A large amount of needle-like ϵ carbides are seen nearby grain boundaries with a number density of $\sim 10^{21} \text{ m}^{-3}$. In addition, $M_{23}C_6$ carbides are also observed on grain boundaries. There are a few of α' particles in the matrix, as shown in figure 2-8(e). After aging for 2000 h, ϵ carbides cannot be observed anymore. The matrix seems to be free of carbides. The aggregation and coarsening of $M_{23}C_6$ carbides are limited on grain boundaries, as presented in figure 2-8(h).

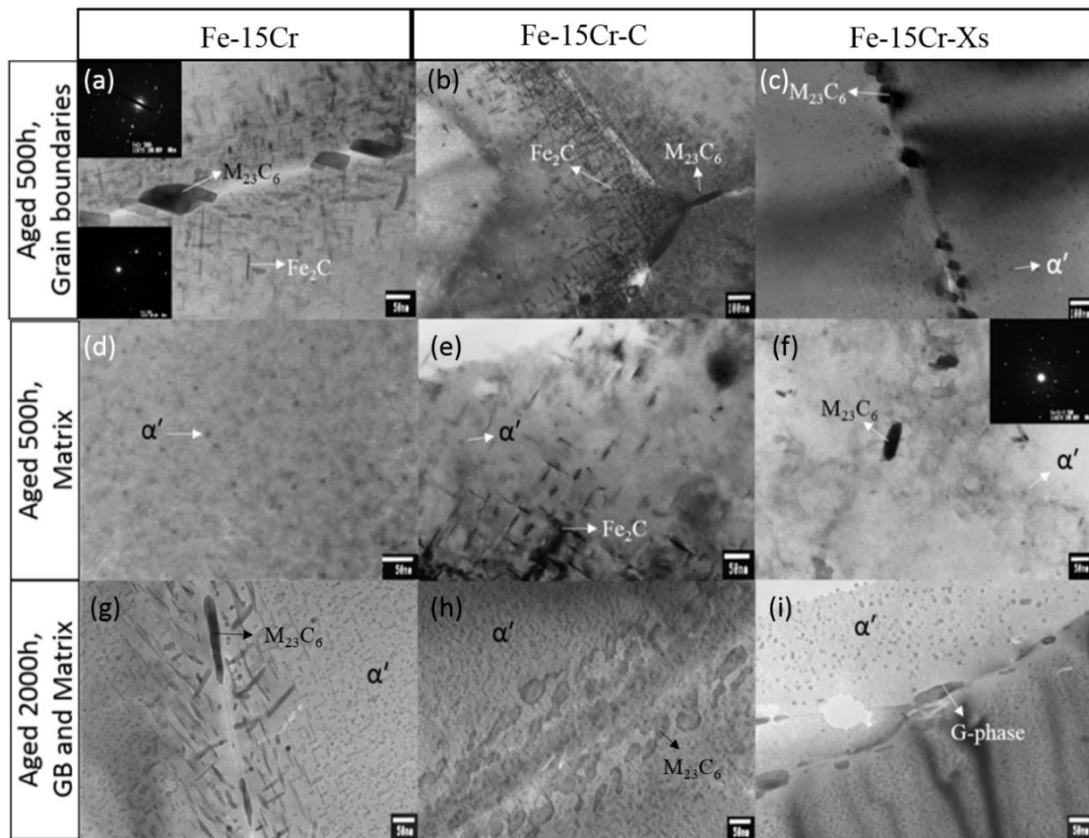


Figure 2-8 TEM microstructural evolution of Fe-15Cr alloys during aging at 475 °C.

It seems that the addition of alloying elements, such as Si, Mn and Ni, accelerates the formation of α' phase, as shown in figure 2-8(c); there are a number of α' particles in the matrix and nearby the grain boundaries of Fe-15Cr-Xs after aged for 500 h. And after 2000h aging, a large number of α' particles are presented in the matrix (figure 2-8(i)). The wavelength of decomposition is about $\sim 7\text{-}10$ nm, which is larger relative to Xs free alloys. Most of precipitates on grain boundaries of Fe-15Cr-Xs are identified as $M_{23}C_6$, as shown in figure 2-10.

A few large precipitates, with size around 100-150 nm, were also observed on grain boundaries of Fe-15Cr-Xs alloy after aged for 2000 h. Figure 2-11 shows the result of TEM EDX line analyses of one large precipitate and the nearby matrix, which indicate that this precipitate is Mn-Si-Ni rich G phase. Recent aging experiments showed that the ferrite-phase decomposition was often accompanied by the precipitation of an intermetallic compound that is known as G phase [16-18]. The chemical composition of the G phase is based on $Ni_{16}Si_7Ti_6$, where iron, chromium, manganese and molybdenum may substitute to nickel and titanium [19]. For Fe-15Cr-Xs, only few G phases are observed on grain boundaries after aging for 2000 h.

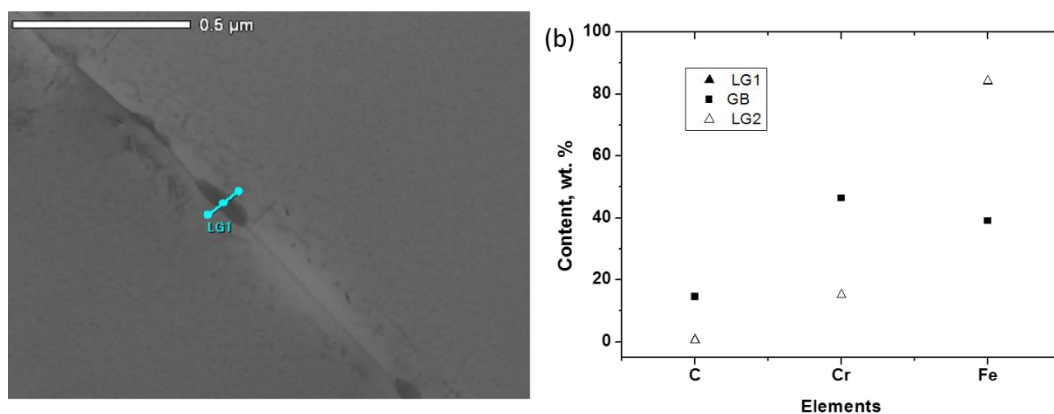


Figure 2-9 (a) TEM bright field image of Fe-15Cr aged for 2000 h, and (b) EDX line analysis result showing the difference in chemical components of GB precipitates and the nearby matrix (LG1 and LG2).

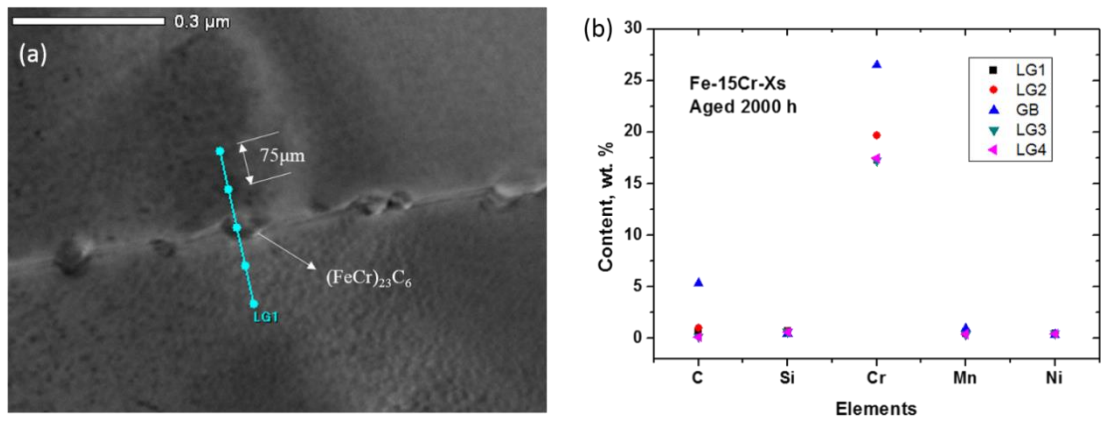


Figure 2-10 (a) TEM bright field image of Fe-15Cr-Xs aged for 2000 h showing EDX line analysis process, and (b) relative components of the GB precipitate and the nearby matrix.

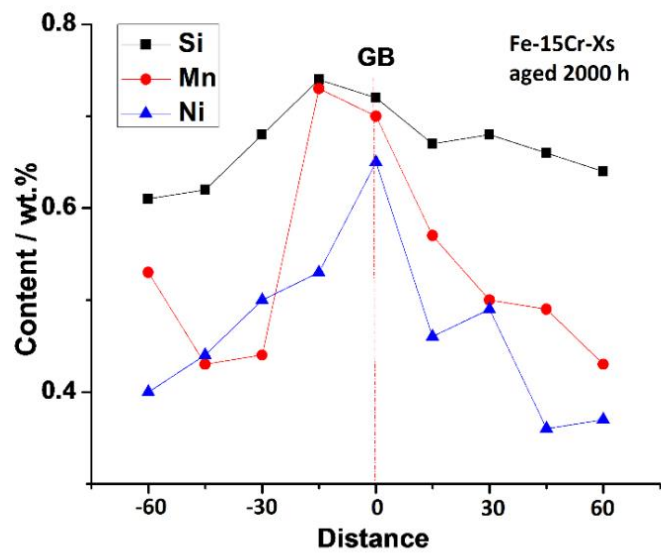


Figure 2-11 TEM EDX line analyses of one large GB precipitate and the nearby matrix showing the relative compositions of Si, Mn and Ni the precipitate.

2.3.2. Mechanical property changes

2.3.2.1. Vickers hardness evolution

Figure 2-12 shows the evolution of Vickers hardness (HV) and increment in Vickers hardness ($\Delta HV = HV - HV_0$, HV_0 is the hardness before aging) during aging at 475 °C. Before aging, the Vickers hardness of the alloy increases with increasing alloying elements as expected. For example, Vickers hardness of Fe-15Cr-C is about 12 HV higher than Fe-15Cr. The alloy hardening can be sum of each effect of carbon or the other alloying elements. As aging time increases up to 5000 h, the Vickers hardness values increase abruptly after an incubation period for all the materials. In order to know the alloying effect on hardening, it's better to divide the aging time to several parts. The difference between the alloys added with alloying elements and pure Fe-15Cr alloy is marked in the gray area in figure 2-11. For aging times up to 2000 h, larger hardness increase values are observed in Fe-15Cr-C and Fe-Cr-Xs than Fe-15Cr, with the largest difference (about 40 HV) at an aging time of around 1000 h.

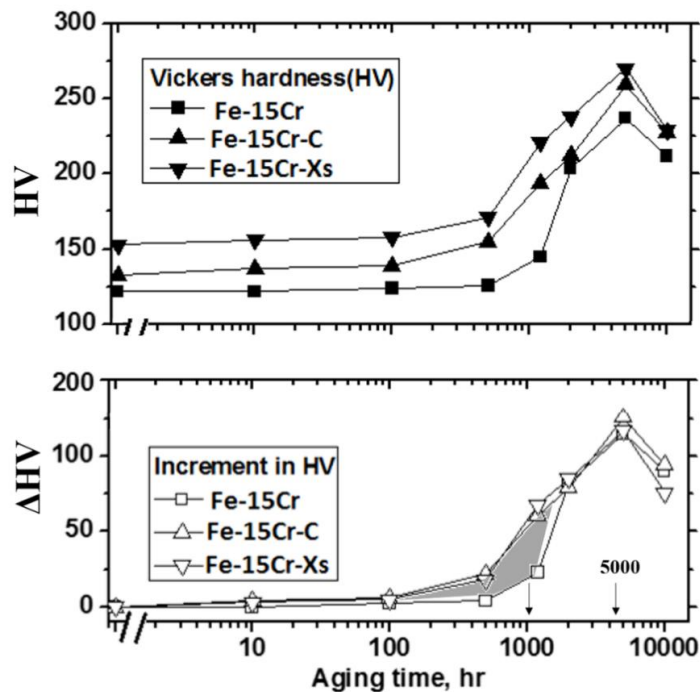


Figure 2-12 Vickers hardness (HV) and increment in Vickers hardness ($\Delta HV = HV - HV_0$, HV_0 is the hardness before aging) as a function of aging time during aging at 475 °C.

2.3.2.2 Tensile property changes

Figure 2-13 shows the change in yield stress (YS), ultimate tensile stress (UTS) and total elongation as a function of aging time. Thermal aging leads to a significant increase in yield stress and ultimate tensile stress with a remarkable reduction of total elongation. For example, for Fe-15Cr, aging for 5000 h results in about 200 MPa increase in yield stress with a reduction of total elongation from 30 % to 11 %. As aging time increases to 5000 h, yield stresses also increase after an incubation period for all the materials. While after aging for 10,000 h, the yield stresses decrease slightly as compared to the peak values. This result agrees with hardness measurements, which may indicate that over-aging may occur.

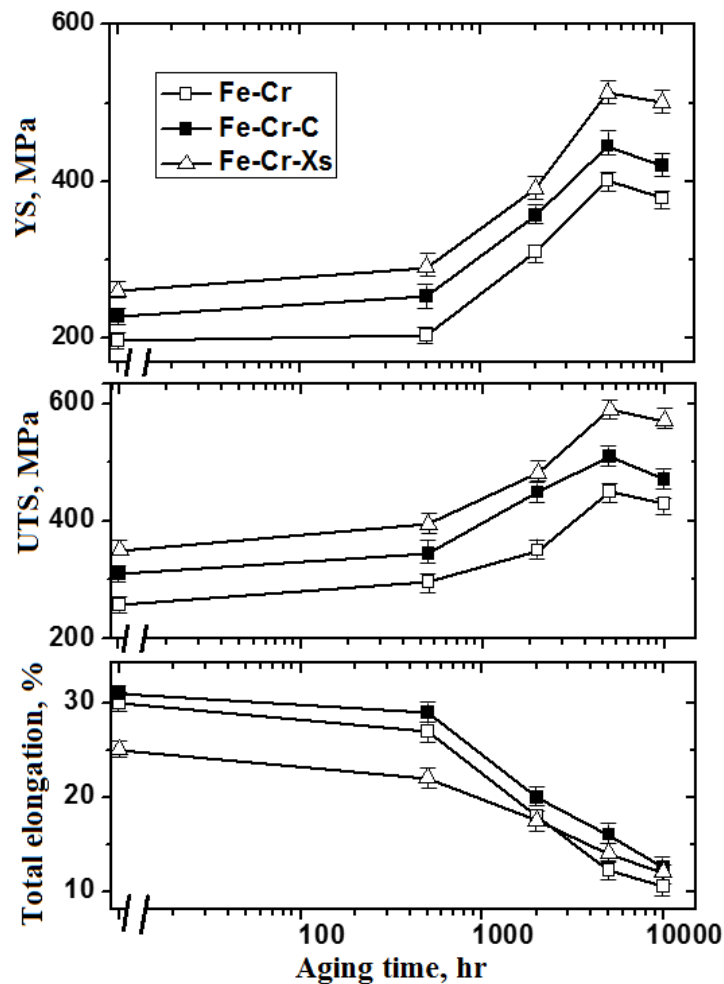


Figure 2-13 Evolution of yield stress (YS), ultimate tensile stress (UTS) and total elongation during aging at 475°C.

To know the effect of age-hardening on ductility loss, figure 2-14 is summarized to show the relations between the change in yield stress, $\Delta\sigma_y$ ($\Delta\sigma_y = \sigma_y - \sigma_{y0}$, $\Delta\sigma_{y0}$ is the yield stress before aging), and the change in total elongation, $\Delta\varepsilon$ ($\Delta\varepsilon = \varepsilon - \varepsilon_0$, ε_0 is the total elongation before aging), of each alloy during aging for different times. There is a linearity between $\Delta\sigma_y$ and $-\Delta\varepsilon$ for all the alloys. This means age-hardening is main reason for ductility loss. However, there is a little difference of the slopes of the plots, $\Delta\sigma_y/-\Delta\varepsilon$ of each alloy, which can be classified into two groups, one is Fe-15Cr and Fe-15Cr-C and the other is Fe-15Cr-Xs. It is considered that the ductility loss of Fe-15Cr-Xs needs a larger age-hardening than Fe-15Cr and Fe-15Cr-C.

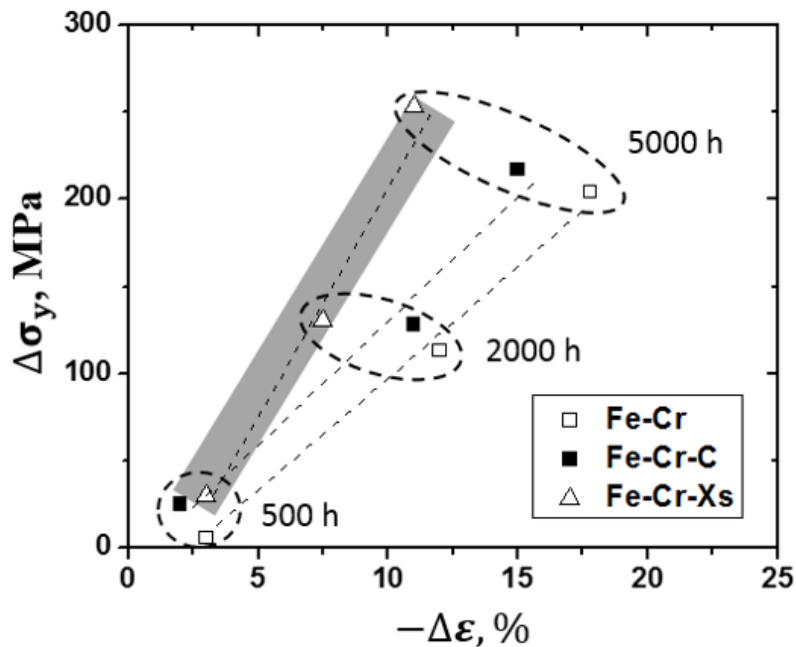


Fig. 2-14 Linear relations between the change in yield stress, $\Delta\sigma_y$, and the change in total elongation, $-\Delta\varepsilon$, of each alloy.

2.3.3. Rupture manners

Figure 2-15 shows the ruptured surfaces of the model alloys deformed at room temperature before and after aging at 475 °C for 10,000 h. Before and after aging, all the alloys rupture in a ductile manner, indicating that the DBTTs of all the specimens are below room temperature even after aging up to 10,000 h. While there are some differences in the

ruptured surfaces between the alloys added with alloying elements and pure Fe-15Cr alloy. As shown in figure 2-15(d), the ruptured surface of Fe-15Cr-C alloy after aged for 10,000 is observed with some delamination structures, which should be attribute to the formation of coarsened carbides along grain boundaries. While for Fe-15Cr-Xs alloy aged for 10,000, there is some brittle ruptured surface observed, as presented in figure 2-15(f).

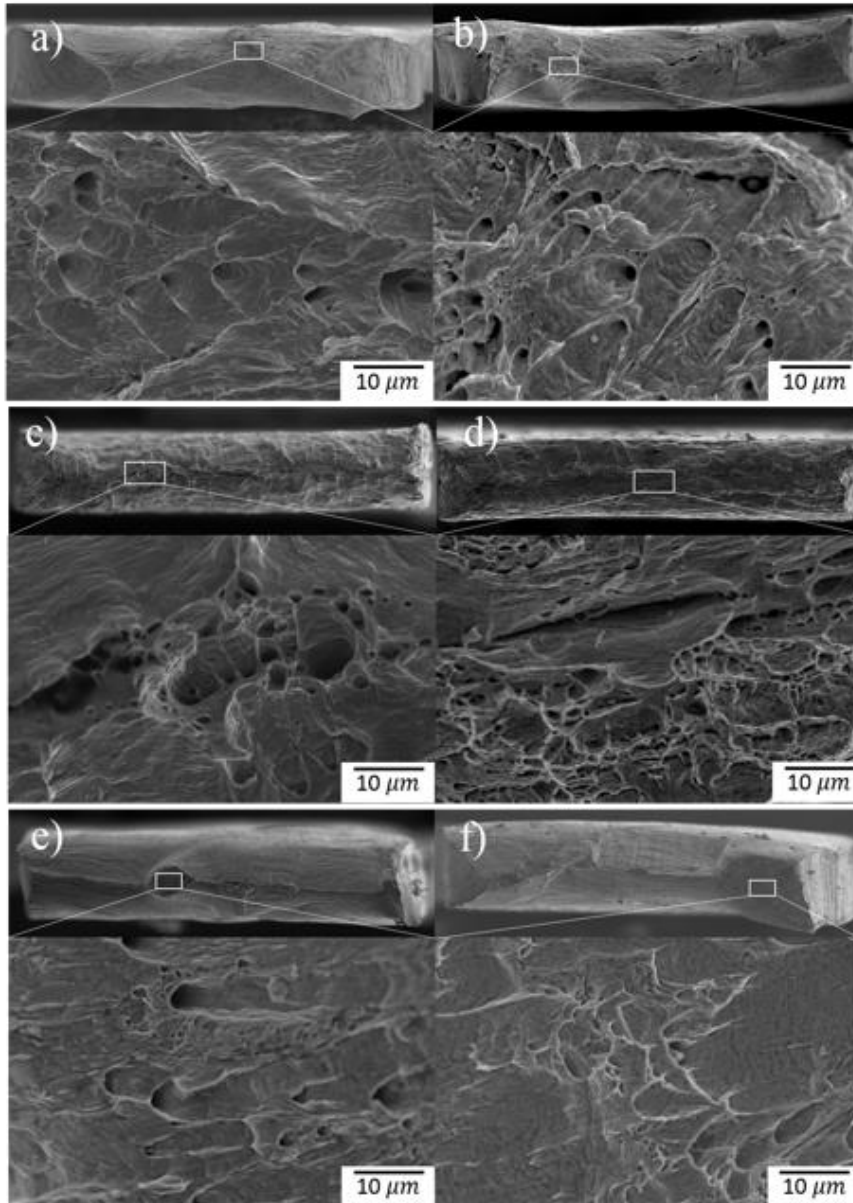


Figure 2-15 Ruptured surfaces of (a) Fe-15Cr, unaged; b) Fe-15Cr, aged for 10,000 h; c) Fe-15Cr-C, unaged; d) Fe-15Cr-C, aged for 10,000 h; e) Fe-15Cr-Xs, unaged; f) Fe-15Cr-Xs, aged for 10,000 h.

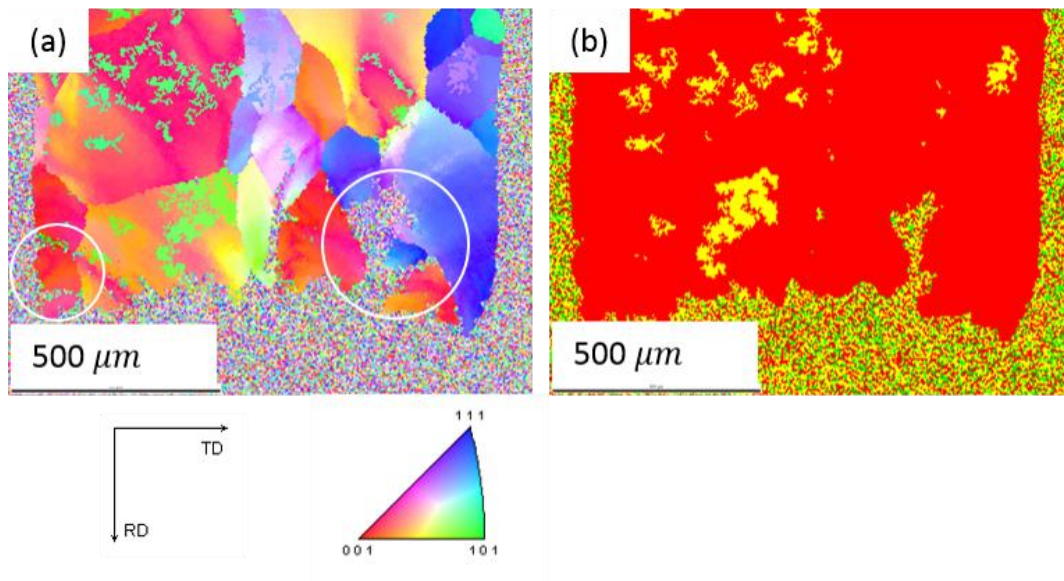


Figure 2-16 Fe-15Cr-Xs alloy after aging for 5000 h: (a) grain morphology of the ruptured region; (b) phase characterization, ferrite (red color) and martensite (yellow).

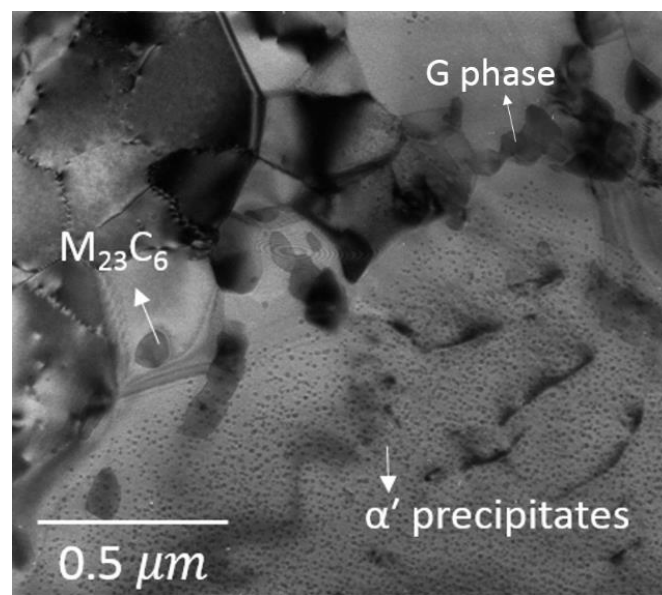


Figure 2-17 TEM bright field images of Fe-15Cr-Xs alloy after aging for 5000 h, showing that the Fe/Cr phase decomposition is observed in ferrite phase but not in martensite phase.

EBSD technique is attractive for showing grain morphologies and strain field. Therefore after tensile testing of Fe-15Cr-Xs alloy aged for 5000 h, the grain morphology and ruptured region were examined by EBSD, as presented in Figure 2-16. The EBSD maps were acquired from the side surface paralleling to RD&TD plane by removing 0.1 mm thickness.

Transgranular ruptures can be found in Fe-15Cr-Xs alloy after RT tensile testing, as shown in the marked areas in Figure 2-16(a). In contrast, this kind of transgranular ruptures were not observed in Fe-15Cr and Fe-15Cr-C alloys. Some phases in ferrite matrix are characteristic of tempered martensite, as presented in figure 2-16(b). But EBSD is not a good technique for characterizing martensitic phase.

Detailed observation by TEM is necessary to know the mechanism why transgranular ruptures occurred only in Fe-15Cr-Xs alloy. Figure 2-17 shows the TEM images of Fe-15Cr-Xs alloy after aging for 5000 h. A lot of large Cr enriched $M_{23}C_6$ carbides and few G phases can be observed on the grain boundaries of ferrite. Based on OM, EBSD and TEM, the structure with very small grains and many carbides should be martensite. Usually, chromium is a ferrite-stabilizing element and as the chromium level is increased, the tendency to form martensite is reduced. In current study, however, it is possible that these martensitic structures were formed due to the inhomogeneous fabrication process. The α' precipitates are finely dispersed in the matrix, but martensite phases show no α/α' phase decomposition structure, which is a big difference with the ferrite matrix.

2.4. Discussion

Both of hardness measurements and tensile tests are in good agreement with microstructure observation. Hardness measurements together with TEM microstructural observation suggest that the early stage of age-hardening of Fe-15Cr-C and Fe-15Cr-Xs is attributed to the addition alloying elements. For example, after aging for 500 h, a large number of $Fe_2C-\epsilon$ carbides are found nearby grain boundaries of Fe-15Cr-C alloy, showing additional hardening relative to Fe-15Cr alloy.

The formation of carbides on or nearby grain boundaries may influence the stability of ferrite by increasing the probabilities of nucleation and growth of α' phase. And the addition of alloying elements, such as Mn, Si and Ni, may increase the number of possible phase separation paths leading to the equilibrium state of the solid solution. The effect of nickel on the aging behavior of Fe-Cr alloys has been investigated by J.E. Brown [20], who showed that the addition of nickel increases the rate of spinodal decomposition upon aging in the

temperature range of 300-450 °C.

However, when aging time increases to 5000 h, the ΔHV of each alloy became similar with an average increment about 120 HV. This result indicates that the addition of alloying elements has a small effect on the total age-hardening. Therefore, although the addition of alloying elements seems to accelerate age-hardening, while the main age-hardening mechanism is due to α/α' phase decomposition. These results are in agreement with those of Grobner [2], who reported that Cr was much detrimental to the embrittlement of high-Cr ferritic alloys due to α' formation than the other alloying elements. The results of current research also show that age-hardening of Fe-15Cr alloys is attributed primarily to the formation of α' phase and the segregation of alloying elements.

The loss of elongation during aging is mainly due to α/α' phase decomposition. Thus, the reason why Fe-15Cr-Xs alloy shows smaller ductility loss than other alloys can be attributed to the formation of martensitic phase, in which α/α' phase decomposition is not observed. TEM EDX analysis shows that the Cr content in martensite is lower than 12 wt. %, which is around the solution limitation of Cr in the Fe enriched matrix. This result can explain why there is no α/α' phase decomposition occurred in martensite. The formation of Cr enriched carbides along the interfaces of martensite and ferrite can reduce the Cr concentration in martensite. However, along the interface of ferrite and martensitic phase, there are some carbides and few Si-Cr-Mn enriched G phases, which can increase the embrittlement of the material. It is considered that the transgranular fracture characterized by EBSD is due to the formation of Cr rich α' precipitates as well as carbides and G phases in Fe-15Cr-Xs alloy.

Another issue beyond 10,000 h is the continuous effect of G-phase precipitation. The investigations of F. Danoix [21] demonstrated that G-phase precipitation was induced by the spinodal decomposition of the ferrite phase. F. Danoix's study [21] indicated that the precipitation rate of G phase mainly depended on the nickel, and possibly silicon, content of the material. Since Figure 2-13 indicates that the reduction of strength after 5000 h is a little bit smaller in Fe-15Cr-Xs alloy than the others, it can be expected that G-phase precipitation starts to contribute to the hardening. The alloys without Ni, Mn and Si additions only show so-called Ostwald ripening of Cr rich phases. Further longer aging period is necessary to confirm the effect of G-phase precipitation on the age- hardening.

2.5 Summary

The effects of long-term isothermal aging (up to 10,000 h, at 475°C) on microstructure and mechanical property changes in Fe-15Cr alloys have been investigated. The main results are summarized as follows:

- (1) Thermal aging at 475 °C for 5000 h resulted in a significant increase in the hardness and tensile strength accompanied by a remarkable decrease in total elongation of Fe-15Cr alloys. Even after 10,000 h aging, all the materials still rupture in a ductile manner at room temperature.
- (2) TEM observation revealed that the addition of carbon and other alloying elements, such as Si, Mn and Ni, caused the formation of some $M_{23}C_6$ carbides and few Mn-Si-Ni enriched G phases on or nearby grain boundaries.
- (3) The formation of isolated Cr-rich precipitates and $M_{23}C_6$ carbides as well as G phases, contributes to the significant age-hardening accompanied by α/α' phase decomposition in Fe-15Cr alloys.
- (4) Age-hardening is mainly caused by Fe/Cr phase decomposition, while alloying elements play a small role in the total age-hardening.

References

- [1] A. Kimura, R. Kasada, N. Iwata et al., “Super ODS Steels R&D for Fuel Cladding of Next Generation Nuclear Systems 1) Introduction and alloy design”, *Proc. Int. Cong. Advances in Nuclear Power Plants, (ICAPP-2009) CD-ROM file*, (2009) p. 9220
- [2] P.J. Grober, “The 885 °F (475 °C) Embrittlement of Ferritic Stainless Steels”, *Metall. Trans.*, **4(1)** (1973) p. 251-260
- [3] T.J. Marrow, “The Fracture Mechanism in 475°C Embrittled Ferritic Stainless Steels”, *Fatigue & Fracture of Engineering Materials & Structures*, **19** (1996) p. 919-933
- [4] S. Kobayashi, T. Takasugi, “Mapping of 475 °C Embrittlement in Ferritic Fe-Cr-Al Alloys”, *Scripta Mater.*, **63** (2010) p. 1104-1107
- [5] G. Bonny, D. Terentyev, L. Malerba, D. Van Neck, “Early stages of α - α' phase separation in Fe-Cr alloys: An atomistic study”, *Phys. Rev. B*. **79** (2009) p. 104-207.
- [6] E. Mueller, “Influence of Carbon and Nitrogen on the Toughness of Ferritic Chromium Steels”, *Neue Heute*, **22(5)** (1977) p. 273-276
- [7] M. Courtnall, F. B. Pickering, “The Effect of Alloying on the 485 °C Embrittlement”, *Metal Sci.*, **10** (1976) p. 273-276
- [8] R.F. Steigerwald, H.J. Dundas, J.D. Redmond, R.M. Davison, “The physical metallurgy of Fe-Cr-Mo ferritic stainless steels”, *Stainless Steel*, **77** (1977) p. 57-72
- [9] H. Abo, T. Nakazawa, S. Takemura, M. Onoyama, “The role of carbon and nitrogen on the toughness and intergranular corrosion of ferritic stainless steels”, *Stainless Steel*, **77** (1977) p. 35-47
- [10] A. Thomas, L. Ernest, M. Hall, “The Long-Term Aging Embrittlement of Fe-12Cr Steels Below 773K”, *Metall. Mater. Trans. A*, **34(A)** (2003) p. 927
- [11] H.D. Solomon, L.M. Levinson, “Mössbauer effect study of 475°C embrittlement of duplex and ferritic stainless steels”, *Acta Metall.*, **26** (1978) p. 429-442
- [12] M. Courtnall, F.B. Pickering, “The effect of alloying on the 485°C embrittlement”, *Met. Sci.*, **10** (1976) p. 273-276
- [13] S.H. Noh, B.J. Kim, R. Kasada, A. Kimura, “Diffusion bonding between ODS ferritic steel and F82H steel for fusion applications”, *J. Nucl. Mater.*, **426** (2012) p. 208-213

- [14] Y. Ohmori, I. Tamura, "Epsilon carbide precipitation during tempering of plain carbon martensite", *Metall. Trans. A*, **23A** (1992) p. 2737
- [15] H. Peter, B. Saeed, P. Liu, O. Joakim, "A Phase-field and Electron Microscopy Study of Phase separation in Fe-Cr alloys", *Mater. Sci. Eng. A*, **534** (2012) p. 552-556
- [16] F. Danoix, P. Auger, "Atom Probe Studies of the Fe-Cr System and Stainless Steels Aged at Intermediate Temperature: A Review", *Mater. Charact.*, **44** (2000) p. 177-201
- [17] J.M. Vitek, S.A. David, D.J. Alexander, J.R. Keiser and R.K. Nanstad, "Low Temperature Aging Behavior of Type 308 Stainless Steel Weld Metal", *Acta Metall. Mater.*, **39** (1991) p. 503
- [18] T. Yamada, S. Okano, H. Kuwano, "Mechanical property and microstructural change by thermal aging of SCS14A cast duplex stainless steel", *J. Nucl. Mater.*, **350** (2006) p. 47
- [19] I. Shuroa, H.H. Kuo, T. Sasaki, K. Hono, Y. Todaka, M. Umemoto, "G-phase precipitation in austenitic stainless steel deformed by high pressure torsion", *Mater. Sci. Eng. A*, **552** (2012) p. 194–198
- [20] J. E. Brown, "An atom probe study of the spinodal decomposition in Fe-Cr-Ni", *Thesis, Department of Materials, University of Oxford, Oxford, UK* (1990)
- [21] F. Danoix, P. Auger, D. Blavette, "An atom-probe investigation of some correlated phase transformations in Cr, Ni, Mo containing supersaturated ferrites", *Surf. Sci.*, **266** (1992) p. 364-369

Chapter 3

Correlation of Fe/Cr Phase Decomposition Process and Age-hardening in Fe-15Cr Alloy

3.1. Introduction

One of the critical issues in the use of the ferritic steels is the 475 °C aging embrittlement, which is caused by the decomposition of the ferrite phase to α and α' phases in the temperature range of 300–550 °C [1-3]. The α' precipitation leads to a progressive hardening and deterioration of fracture toughness. Williams [4] carried out Mössbauer measurements on the effect of 475 °C aging in a series of iron-chromium binary alloys with a varying the chromium content, and concluded that the alloys with chromium content 12–30 at.% decomposed via nucleation and growth mechanisms. An atomistic study [5] on the hardening behavior of iron-chromium alloys under thermal aging has been done by G. Bonny et al. showing the different stages of α/α' unmixing, but this technique provides no information about the morphology of precipitates in real space.

Quantitative study of the α/α' phase decomposition is of interest recently, while no study have been done to discuss the α' size dependence of strengthening factor for evaluation of the age-hardening. In this study, strengthening factor of the α' precipitates and the evolution of microstructure of α/α' phase decomposition have been investigated.

3.2. Experimental

The material used in this work is pure Fe-15wt. % Cr alloy. The fabrication process of Fe-15Cr alloy has been introduced in Chapter 2. Chemical compositions of Fe-15Cr alloy is shown in Table 3-1. Miniaturized tensile tests were performed at room temperature. Tensile samples were punched from a 0.3 mm thick plate parallel to the cold-rolling direction and mechanically ground to about 0.25 mm in thickness. The dimensions of tensile specimens are 16 mm length \times 4 mm width \times 0.25 mm thickness. At least three tensile tests were carried out and the averaged values were obtained.

Disk-type TEM specimens of 3 mm diameter were punched out from a 0.3 mm thick plate and mechanically grounded to about 100 μ m in thickness. Final thin foils for TEM observation were prepared by electrolytic polishing with HClO₄ and CH₃OH (1:9) using a twin-jet polisher at a voltage of 20 V at room temperature. The thickness of thin foils was

measured using convergent-beam techniques. Convergent beam electron diffraction (CBED) is a diffraction technique in which the electron beam is converged in to a small probe on the specimen, rather than using parallel illumination as for selected area diffraction [6]. CBED is a good method for navigating reciprocal space while tilting the specimen and aligning on zone axes, by way of the strong Kikuchi lines present in the off-axis CBED pattern. The on-axis CBED pattern consists of diffraction disks analogous to the spots in a SAD pattern (with the size of those discs determined by the convergence angle of the beam). The size and number density of α' particles were measured to investigate the effect of α' phase on the age-hardening behavior.

The chemical compositions of precipitates were measured using a TEM JEM-2200FS equipped with an energy-dispersive X-ray (EDX) spectroscopy system.

Some specimens were sealed in ampoules in high vacuum conditions (10^{-4} Pa) and isothermally aged at 475 °C for up to 10,000 h.

Table 3-1 Chemical compositions of Fe-15Cr alloy (wt.%).

Material	Cr	C	Fe
Fe-15Cr	14.55	0.001	Bal.

3.3. Results

3.3.1. Age-hardening behavior

The yield stress was measured to characterize the age-hardening behavior of Fe-15Cr alloy. The evolution of yield stress, YS, and the increment in yield stress, $\Delta YS = YS - YS_0$, during aging at 475 °C is shown in figure 3-1, where YS_0 is the YS before aging. The evolution of age-hardening, namely the increment in yield stress, experiences three stages: (1) incubation (<500 h), (2) strengthening (500-5000 h), and (3) softening (5000-10,000h). As aging time increases up to 5000 h, the yield stress value increases abruptly after an incubation period. After aging for 10,000 h, however, there is a slight decrease in yield stress as compared to the peak value. It seems that 5000 h is a turning period of under-aging and over-aging caused by thermal aging.

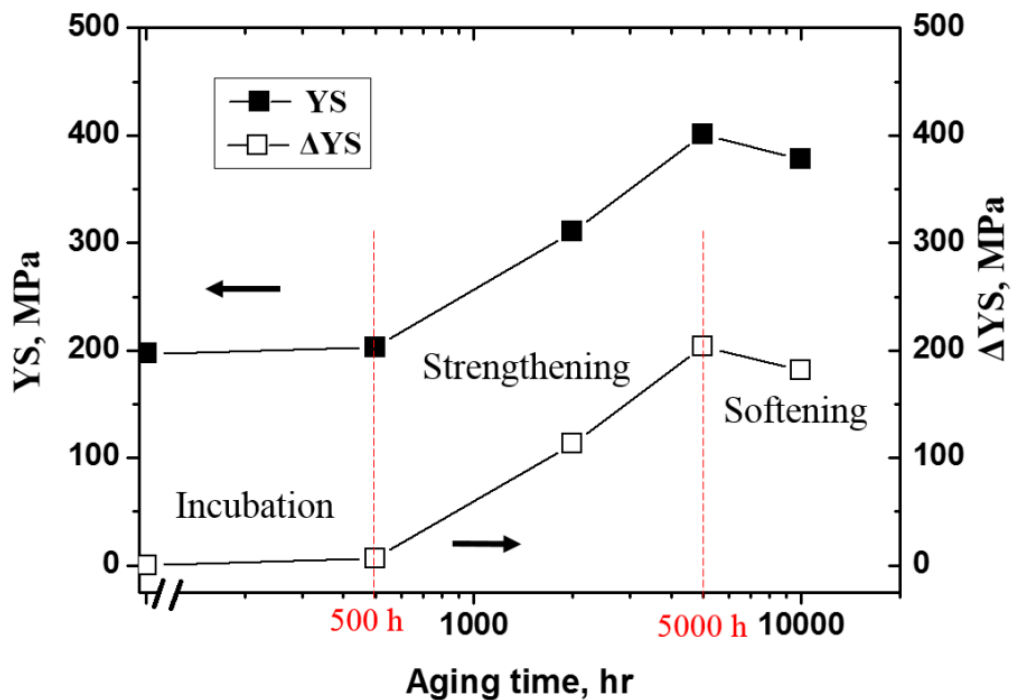


Figure 3-1 Yield stress, YS, and the increment in yield stress, $\Delta YS = YS - YS_0$, as a function of aging time during aging at 475 °C.

3.3.2. Microstructure changes

TEM observations were performed to show the microstructure changes corresponding to each age-hardening period. Phase decomposition of the ferrite to α' and α phases is also identified by TEM EDX line analysis, as shown in figure 3-2, which shows the composition fluctuation of Cr in the matrix.

As is shown in figure 3-2, finely-dispersed, nanometer size α' particles can be observed after 5000 h aging. The fluctuation amplitude of α' particles is about 8 wt.%, with a minimum value of 11 wt.% and maximum 19 wt.%, although the EDX analyses can only provide an average component of a region [7], thus the result cannot be used as real component of α' particles.

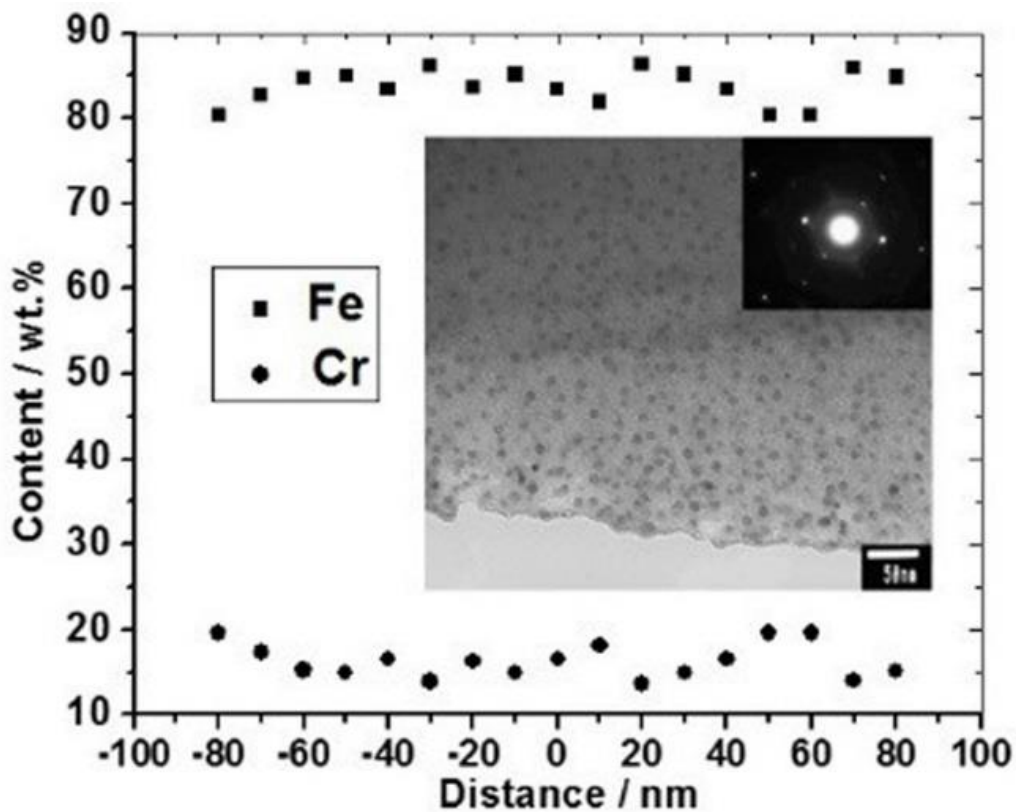


Figure 3-2 FE-TEM EDX line analysis of Fe and Cr in Fe-15Cr alloy after aging for 5000 h, and bright field images showing finely-dispersed, nanometer size α' particles in matrix.

Figure 3-3 presents the evolution of α' precipitates observed by TEM in this research and simulated results by the other researcher [8]. The TEM bright field images were obtained when aging time reaches 0 h, 500 h, 2000 h, and 5000 h. The simulation results were provided by I. Dopico [8], who was interested in our work and used a computational model to reproduce the α/α' phase decomposition behavior of the Fe-15Cr alloy. The bright field TEM images show a good agreement with the simulation results, which are based on density functional theory (DFT), provided by I. Dopico.

The Cr-rich α' precipitates, which have a lattice parameter $a_{\text{Cr}} = 0.288$ nm, are found to be coherent body-centered cubic (bcc) particles [9]. The strain field of the interfaces between α' precipitates and the Fe-rich matrix is quite low due to the similar lattice parameter of Cr and Fe. Therefore, there is a difficulty to observe the early stage of α/α' phase decomposition by conventional TEM.

From the TEM images, only a few α' particles are found after aging for 500 h, while larger size and higher number density of α' particles are observed as aging time increases. The underlying α/α' phase decomposition process of Fe-15Cr alloy is via nucleation and growth of α' precipitates. This mechanism agrees with a Mössbauer spectroscopy study by S.M. Dubiel [10], who reported that nucleation and growth mechanism worked in Fe-15 at.% Cr alloy during annealing at 415 °C. They also calculated the activation energy of the phase decomposition in Fe-14Cr alloy, which is about 122 kJ mol⁻¹ [11]. The nucleation of α' particle, thus, requires a certain thermal aging time to gain enough nucleation energy. This agrees with the present results of tensile tests because there is almost no change of yield stress until aging for 500 h.

The simulation work provided additional information about the process of nucleation and growth, as well as the composition information of α' precipitates. As shown in the marked areas, some α' precipitates grow to larger size, while some small α' precipitates disappear. This indicates that the precipitation process occurs via nucleation, growth and coarsening. The color bar on the right side of simulation maps refers to the real chemical component of α' precipitates. With increasing aging time, the concentration of Cr in α' precipitates increases.

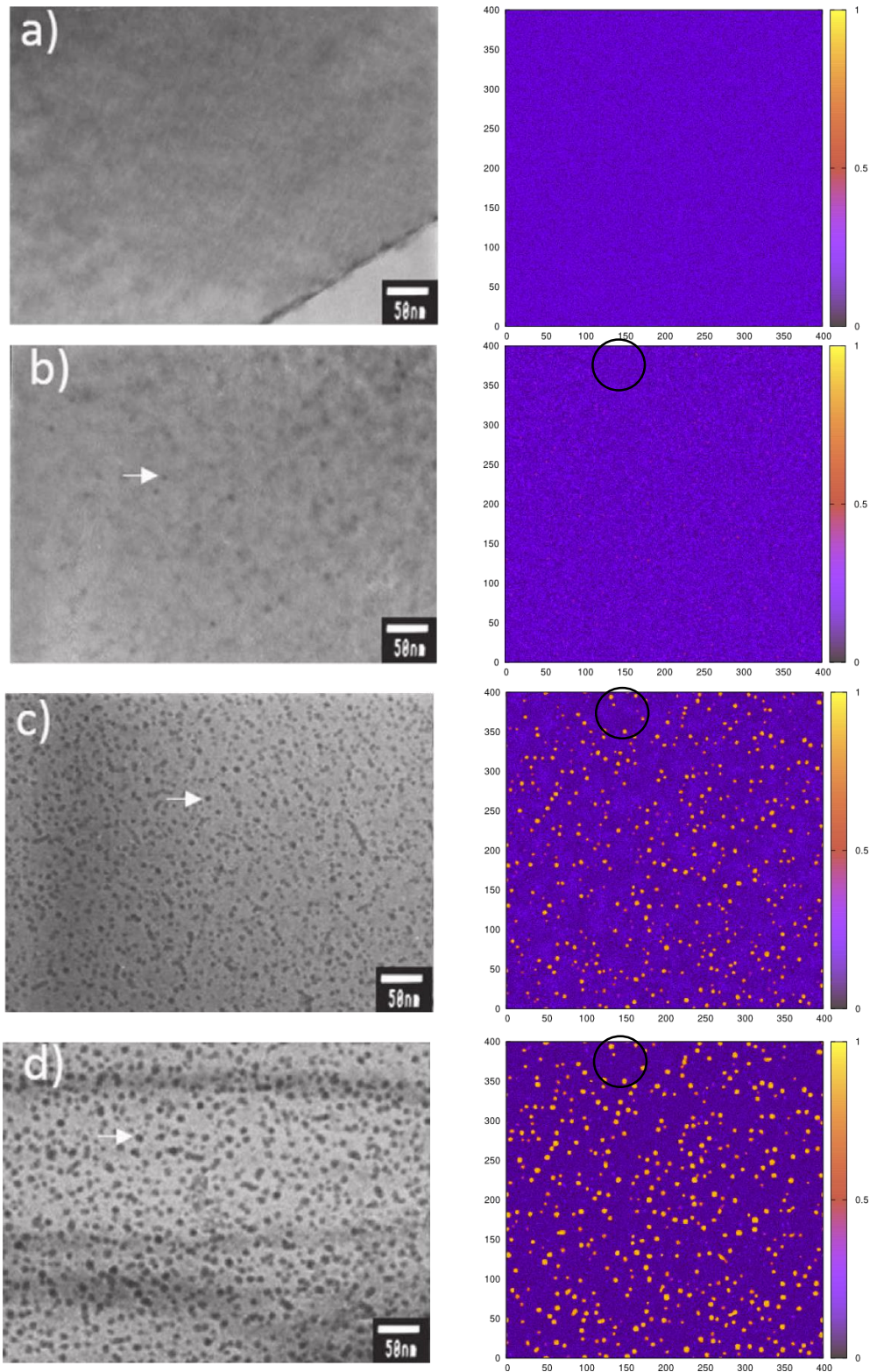


Figure 3-3 Bright field TEM images (left) and simulation results (right), showing a microstructure evolution of Fe-15Cr alloy after aging for (a) 0 h, (b) 500 h, (c) 2000 h, and (d) 5000 h, black dots indicate Cr-rich α' particles.

3.4. Discussion

3.4.1. Phase decomposition characteristic

Phase decomposition process can be described in terms of the average diameter, d , and number density, N , of α' particles. Figure 3-4 shows the average diameter and number density of α' particles as a function of aging time, which were estimated from TEM observations. There is a linear relation of the size of α' particles with thermal aging time. With increasing aging time, the average diameter of α' particles becomes larger, while the number density of α' particles experiences a rapid growth followed by a progressively decrease.

There are quite few α' particles in Fe-15Cr alloy after aging for 500 h. Thermal aging for 2000 h results in formation of quite a large number of α' particles in matrix, with an average diameter of 5.2 nm and a number density of $4.9 \times 10^{22} \text{ m}^{-3}$. After aging for 5000 h, however, the α' precipitates coarsen to an average diameter of 8.3 nm, and the number density of α' particles decreases, to a number density of $3.8 \times 10^{22} \text{ m}^{-3}$. When aging time reaches up to 10,000 h, the averaged diameter of α' precipitates increases to about 11 nm with a number density decreasing to $1.2 \times 10^{22} \text{ m}^{-3}$.

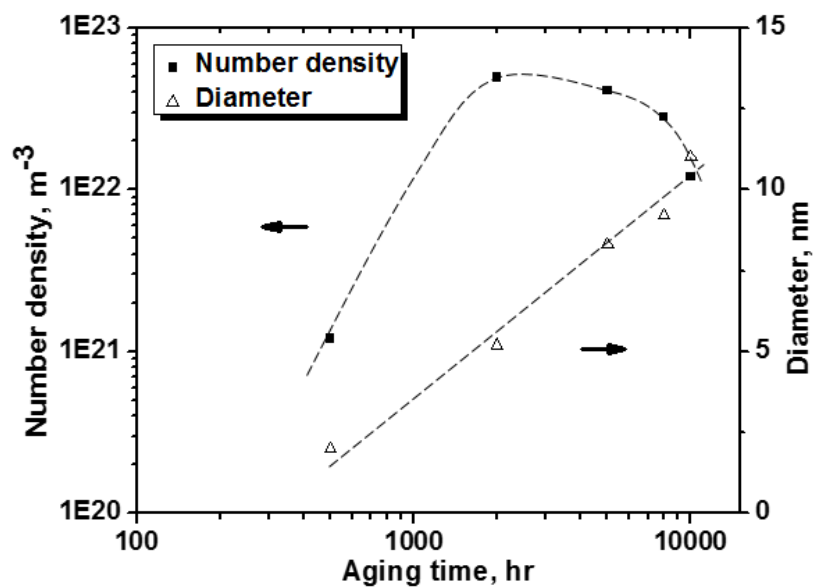


Figure 3-4 Average diameter and number density of α' particles as a function of aging time in Fe-15Cr alloy.

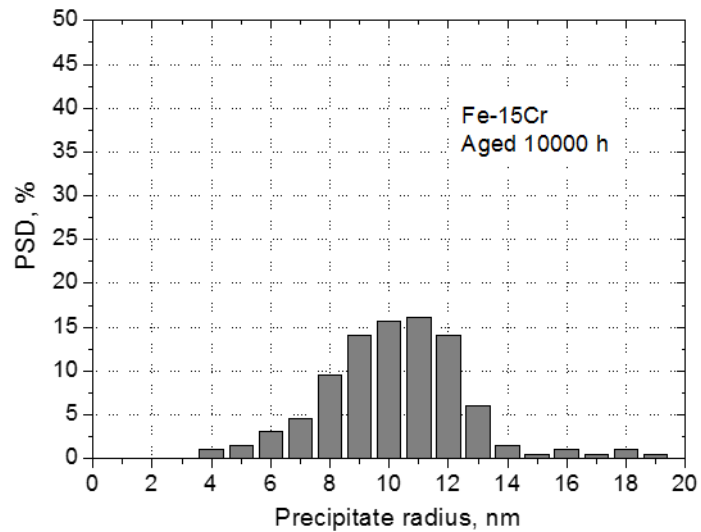
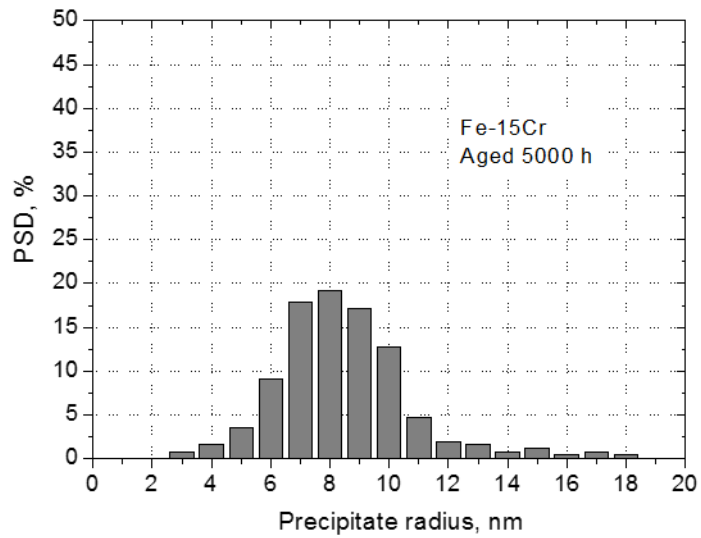
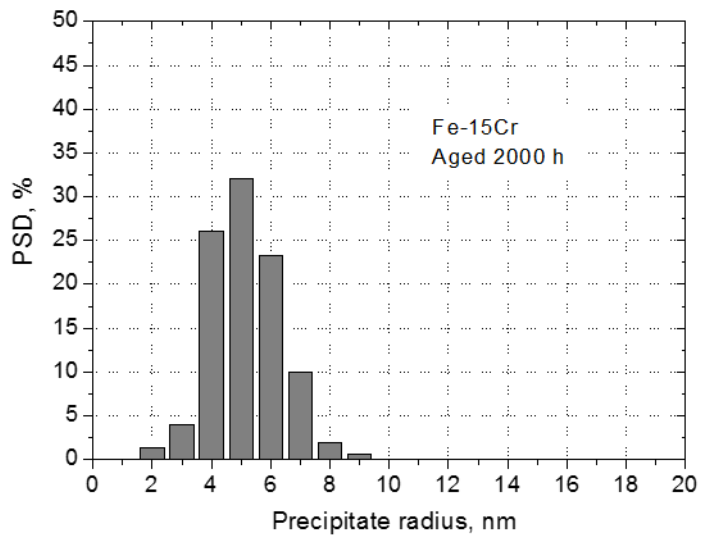


Figure 3-5 Particle size distribution (PSD) of α' precipitates in Fe-15Cr alloy after aging for 2000 h, 5000 h and 10,000 h.

Figure 3-5 provides the particle size distribution (PSD) of α' precipitates in Fe-15Cr alloy after aging for 2000 h. The narrow distribution observed after 2000 h becomes wider after 5000 h. The evolution of the PSD seems to point out that a non-steady-state of coarsening occurs up to aging for 10,000 h. This result agrees with an atomic scale study by S. Novy [12], who reported that a thermally aged (500 °C) Fe-20Cr alloy showed a transient coarsening regime with an overlap between nucleation, growth and coarsening. This overlap mechanism is proposed by Robson [13] with his modified version of numerical precipitation model based on the initial Langer-Schwartz model [14]. Indeed, if the initial super-saturation is large enough, a significant nucleation rate is retained even when a substantial proportion of the solute has been removed from the matrix, thus leading to an increase in the critical particle size, below which all particles are dissolved. Then, whereas some α' precipitates are yet appearing, coarsening causes dissolving the smallest particles, and consequently leading to a reduction in the number density.

Figure 3-6 shows the phase diagram of Fe-Cr systems with a miscibility gap [15]. When an alloy of composition X_0 is homogenized at T_1 and then quenched to T_2 , originally it has uniform chemical composition and its Gibbs energy is equal to G_0 on the diagram in figure 3-6(b). This alloy is unstable at T_2 because composition fluctuations, creating regions rich in A and rich in B, lead to a decrease in total Gibbs energy of the system.

Subsequently uphill diffusion occurs and continues until a two phase structure with equilibrium compositions of X_1 and X_2 is achieved, as shown in figure 3-7(a). Such transformation occurs at any composition for which free energy-composition curve has negative curvature, mathematically $d^2G/dx_{Cr}^2 < 0$. Therefore the composition should lie between the inflection points of the Gibbs energy-composition curve. Loci of these points on the phase diagram are called the chemical spinodal. When the alloy composition lies outside the spinodal, infinitesimal fluctuations in chemical composition result in an increase in the total Gibbs energy, hence the system would become metastable. In this case reduction in Gibbs energy of the system is possible only when the nuclei composition is very different from that of the matrix. Therefore outside the spinodal, transformation must be conducted through nucleation and growth, as shown in figure 3-7 (b).

In this study, the Cr concentration in Fe-15Cr alloy is 15wt.%, where $d^2G/dx_{Cr}^2 > 0$.

This means that Fe-15Cr alloy is out the spinodal line and follows a nucleation and growth model. TEM observation shows good agreement with phase transformation model provided by D.A. Porter and K.E. Easterling [16].

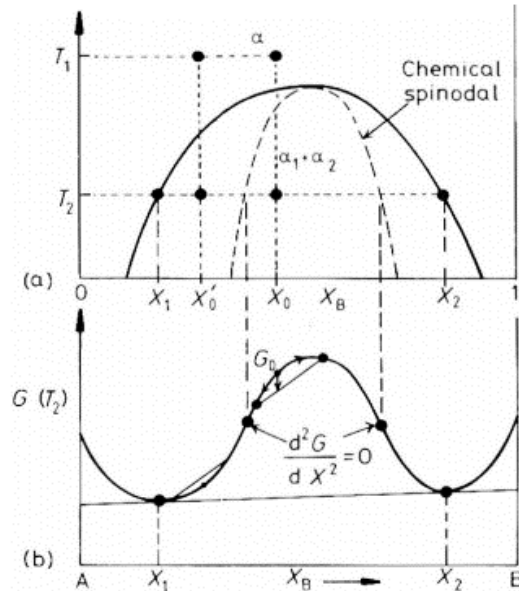


Figure 3-6 (a) The bold line designates the (incoherent) miscibility gap and the dashed line the (chemical) spinodal regions, (b) Gibbs energy-composition curves at T_2 .

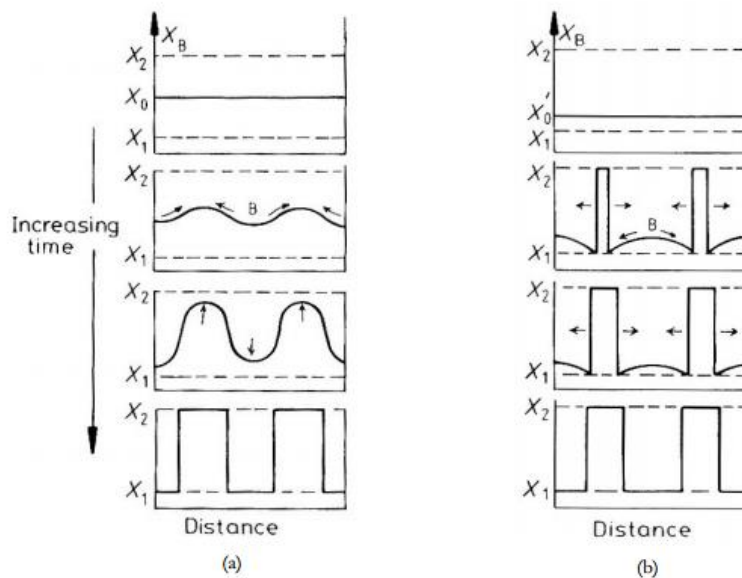


Figure 3-7 Schematic plot of composition-distance at different aging times in alloy (a) inside the spinodal and (b) outside the spinodal.

3.4.2. Age-hardening mechanism

3.4.2.1. Strengthening stage

With increasing aging time, yield stress increase due to the α/α' phase decomposition. Age-hardening is due to the formation of Cr-rich precipitates. Figure 3-8 shows a schematic diagram of a moving dislocation cutting through Cr-rich precipitates, which were a weak barriers to dislocation motion. Before cutting, there are Cr-Cr bonds inside the Cr-rich precipitate and Fe-Fe bonds outside it. After cutting, Fe-Cr bonds appear in the hatched area in the figure 3-8. The energy needed for the formation of one Fe-Cr bond from Fe-Fe and Cr-Cr bonds [17], W , is expressed as follows:

$$W = E_{Fe-Cr} - (E_{Fe-Fe} + E_{Cr-Cr})/2 \quad (3.1)$$

where E is the bonding energy.

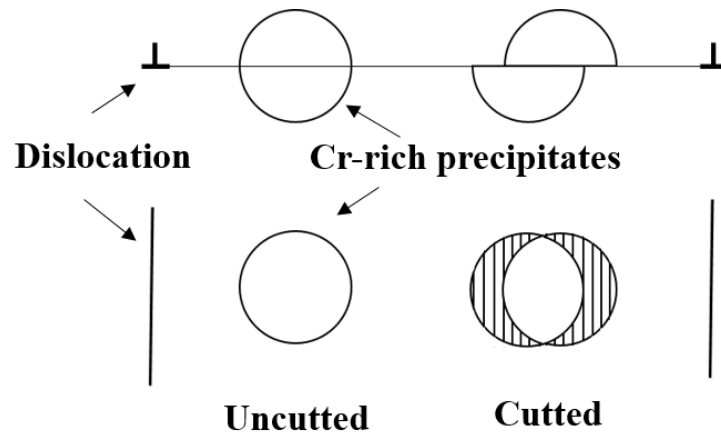


Figure 3-8 Schematic diagram of Cr-rich precipitate cutting process by edge dislocation.

Although Eq. (3.1) may provide the origin of strengthening caused by Cr-rich precipitates, further quantitative research based on the current data is necessary to clear the age hardening mechanism in Fe-15Cr alloy. The increase in yield stress can be given by the following equations as a function of the diameter and number density of α' particles:

$$\Delta\sigma_y = M\alpha Gb(Nd)^{1/2} \quad (3.2)$$

$$\Delta\sigma_y = \alpha M G b (N)^{2/3} d \quad (3.3)$$

Eq. (3.2) is based on the dispersed barrier hardening model [18] and Eq. (3.3) is on the

Friedel-Kroupa-Hirsch (FKH) model [19]. In the two equations, $\Delta\sigma_y$ is the increment in yield stress, M is the Taylor factor (3.06), α is the strengthening factor, G is the shear modulus (75.3 GPa), b is the Burgers vector (0.248 nm). In Eq. (3.2), α is assumed to be varying from 0.11 to 1 depending on barrier type [18]. In Eq. (3.3), α is assumed to be 4/5 for strong obstacles and 1/8 for small dislocation loops [20]. Both models can be applied for weak barriers. Another model for impenetrable obstacles is an expression derived from continuum model simulations by Scattergood and Bacon (SB) [21]:

$$\Delta\sigma_y = \frac{\mu b}{2\pi L} \left[\ln \left(\frac{1}{\frac{R_1}{L} + \frac{R_1}{d}} \right) + 0.7 \right] \quad (3.4)$$

where R_l is cut-off radius of the dislocation core (taken to be equal to b) and L is the free passage distance ($L = L_y - 2R_{PRP}$, R_{PRP} is radius of precipitates). However, Eq. (3.4) should be only applied for reaction satisfying the Orowan bypass model (the presence of a screw dislocation dipole drawn out from the obstacle).

As for the strength factor, α , of obstacles, a molecular dynamics (MD) simulation work [22] provided those values of the coherent Cr precipitate of 2 nm diameter, dislocation loops and voids as a function of temperature in bcc Fe, and the obtained values were in the range 0.17-0.37 at room temperature. In this research, the strength factor α of Cr precipitates at room temperature is assumed to be 0.2 that is similar to the estimated value of Cr precipitates estimated in the resent MD work [22].

The relationships between the calculated increment in yield stress, $\Delta\sigma_y^{cal.}$ and the measured increment in yield stress, $\Delta\sigma_y^{mea.}$, are shown in figure 3-5. Precipitation hardening was often interpreted in terms of the Orowan type dispersed barrier hardening model, although no dislocation loop was left surrounding precipitates. In this work, however, Orowan type model does not reproduce the monotonic increase in the hardness with increasing aging time. The same trend is observed for the FKH model, which is considered to be applied to rather weak obstacles for dislocation motion. Although no linear relationship is observed for any of the models, both Orowan type model and SB model can be applied to explain the age-hardening caused by α/α' phase separation after a longer aging time (~5000 h). More detailed experimental works are necessary to clear the hardening mechanism.

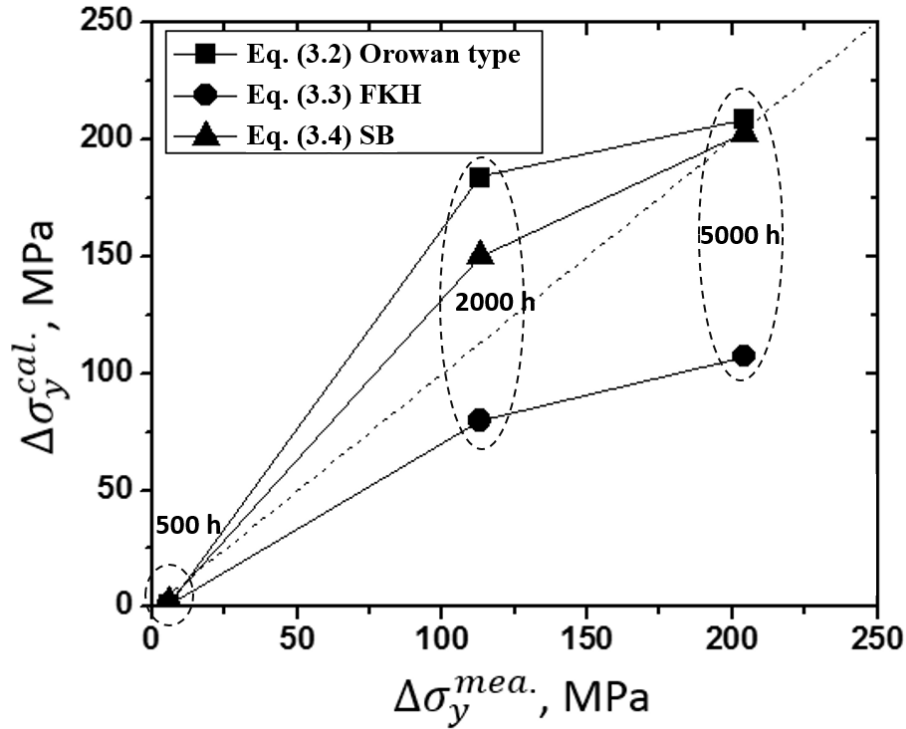


Figure 3-9 Relationships between the calculated increment in yield stress $\Delta\sigma_y^{cal.}$ and the measured increment in yield stress $\Delta\sigma_y^{mea.}$ in Fe-15Cr alloy.

3.4.2.2. Softening stage

Figure 3-10 provides the evolution of α/α' phase decomposition in Fe-15Cr alloy after aging for 5000 h, 8000 h and 10,000 h. As increasing aging time, the α' precipitates continue coarsening with a decrease of number density. Because of the lower strain field of the interface of Cr-rich phase and Fe-rich matrix, TEM observation must be at under focus condition. It seems that there is no orientation dependence of the contrast of α' precipitates. Figure 3-10(c) shows the TEM bright field images of Fe-15Cr alloy with $g = [11\bar{2}]$ after aging for 10,000 h; the average diameter of α' precipitates grows to 11 nm with a density decreased to $1.6 \times 10^{22} \text{ m}^{-3}$. This result indicates that the strength decreases slightly, although α' precipitates continue to grow up.

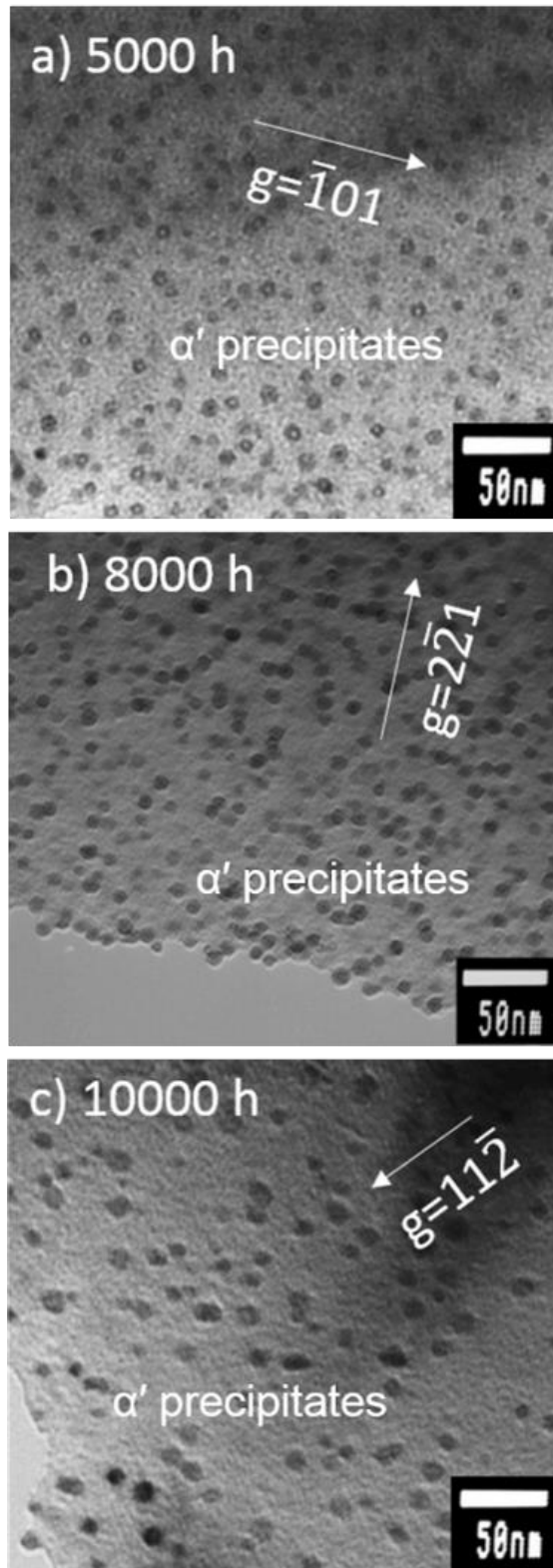


Figure 3-10 TEM bright field images showing microstructure evolution of Fe-15Cr alloy after aged for (a) 5000 h, (b) 8000 h, and (c) 10, 000 h.

When aging time reaches 10,000 h, thermal aging undergoes an over-aging, which leads to a decreasing strength. The coarsening of the precipitates is usually accompanied by a loss of coherency in the matrix and an increase in the interfacial energy is expected [23]. This increase goes from a lower value for small coherent particles to a higher value for larger coherent particles. Figure 3-11 shows a sketch map of precipitation strengthening curve of Fe-15Cr alloys. We may define the critical particle size as d_c , then:

- (1) when $d < d_c$, coherency strengthening increases with increasing particle size;
- (2) when $d > d_c$, coherency strengthening decreases with increasing particle size.

At small sizes, the dislocation cuts through the particle at a lower stress than the Orowan bowing stress. While, large particles need higher cutting stresses. At large sizes, the dislocation bows around the particle more easily than it cuts through it.

Such a relationship between strengthening effect and particle size gives a maximum strengthening at a critical particle size d_c . According to the current data, the critical d_c for Fe-15Cr alloy is about 8 nm. It is considered that dislocation looping can take place whenever the precipitates is too big/strong for dislocation to cut through, regardless of the coherency nature of the interface between the precipitate and matrix.

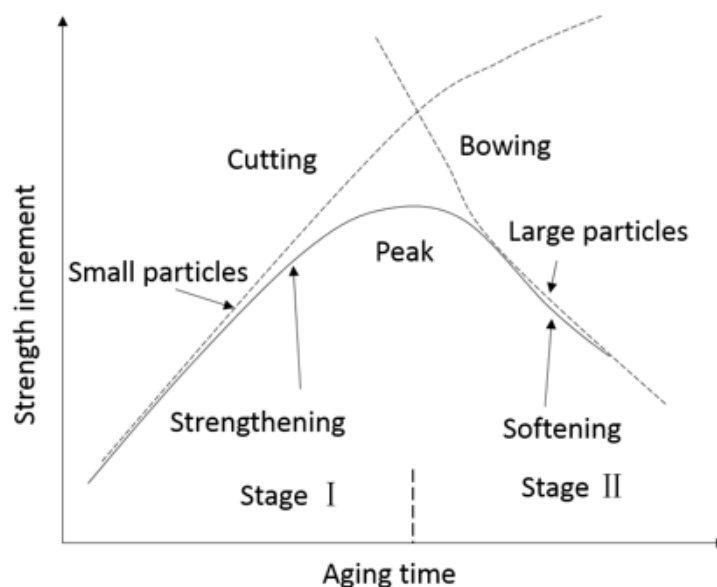


Figure 3-11 Age-hardening curve and sketch diagram for precipitation hardening mechanism.

3.5. Summary

Quantitative evaluation research on the correlation of age-hardening and α/α' phase decomposition process has been carried for Fe-15Cr alloys. The following results have been obtained:

- (1) Based on the TEM observation, the age-hardening is mainly due to the formation of isolated Cr-rich α' precipitates. TEM observations of evolution of α' precipitates show a good agreement with the density functional theory (DFT) calculation results.
- (2) The formation of α' precipitates in Fe-15Cr alloys during 475 °C is via nucleation and growth. The growth of α' precipitates is characterized as non-steady-state of coarsening, where the overlap of nucleation, growth and dissolution processes of α' particles is observed by TEM.
- (3) As aging time increases, the mean size of α' precipitates increases linearly with the aging time. The number density of α' precipitates shows a rapid increase followed by a progressive decrease.
- (4) The age-hardening in strengthening period is interpreted in terms of the dispersed barrier strengthening models with α' precipitates. The strengthening factor of α' precipitates is assumed to be 0.2 at room temperature. Both the Orowan type dispersed strengthening model and the Scattergood and Bacon (SB) continuum model can be applied to explain the age-hardening caused by α/α' phase decomposition after a longer aging time.
- (5) Age-hardening shows two stages, increasing (strengthening) and decreasing (over aging), showing a peak in the strength with increasing aging period. The over aging after aging beyond 5000 h is associated with the reduction of number density and the increase in the size of α' precipitates. The critical size of α' precipitates for the transient form strengthening to softening is around 8 nm.

References

- [1] R.M. Fisher et al., "Identification of the Precipitate Accompanying 885 °F Embrittlement in Chromium Steels", *Trans. AIME*, **197** (1953) p. 690-695
- [2] P.J. Grober, "The 885 °F (475 °C) Embrittlement of Ferritic Stainless Steels", *Metall. Trans.*, **4(1)** (1973) p. 251-260
- [3] T.J. Marrow, "The Fracture Mechanism in 475°C Embrittled Ferritic Stainless Steels", *Fatigue & Fracture of Engineering Materials & Structures*, **19** (1996) p. 919-933
- [4] R.O. Williams, "Further studies of the iron-chromium system", *Trans. TMS-AIME*, **212** (1958) p. 497-502
- [5] G. Bonny, D. Terentyev, L. Malerba, D. Van Neck, "Early stages of α - α' phase separation in Fe-Cr alloys: An atomistic study", *Physical Review B*, **79** (2009) p. 104-207
- [6] J.A. Eades, "Convergent-beam techniques in transmission electron microscopy", *Applied Surf. Sci.*, **26** (1986) p. 280-293
- [7] J. Goldstein, "Scanning Electron Microscopy and X-Ray Microanalysis", *Springer. ISBN 978-0-306-47292-3.*, (2012)
- [8] I. Dopico, ignacio.dopico@imdea.org, Spanish Scientific Institution IMDEA Materials of Madrid, Spain
- [9] J. Ribis, S. Lozano, "Orientation relationships and interface structure of α' -Cr nanoclusters embedded in α -Fe matrix after α - α' Demixing in neutron irradiated Oxide Dispersion Strengthened material", *Mater. Lett.*, **74** (2012) p. 143-146
- [10] S.M. Dubiel, J. Zukrowski, "Fe-rich border of miscibility gap and activation energy of phase decomposition in a Fe-Cr alloy", *Mater. Chem. Phys.*, **141** (2014) p.18-21
- [11] S.M. Dubiel, J. Zukrowski, "Phase-decomposition-related short-range ordering in an Fe-Cr alloy", *Acta Mater.*, **61** (2013) p. 6207-6212
- [12] S. Novy, P. Pareige, C. Pareige, "Atomic scale analysis and phase separation understanding in a thermally aged Fe-20 at. %Cr alloy", *J. Nucl. Mater.*, **384** (2009) p. 96-102
- [13] J.D. Robson, "Modelling the overlap of nucleation, growth and coarsening during precipitation", *Acta Mater.*, **52** (2004) p. 4669

- [14] J.S. Langer, A.J. Schwartz, “Kinetics of nucleation in near-critical fluids”, *Phys. Rev. A*, **21** (1980) p. 948-958
- [15] T.B. Massalsky, H. Okamoto, P.R. Subramanian, L. Kacprzac, “Binary alloy phase Diagrams”, *ASM International, Materials Park, OH* (1990) 1273
- [16] D.A. porter, K.E. Esasterling, “Phase Transformations in Metals and Alloys”, *Paperback*, July, (1992)
- [17] Pär Olsson, Janne Wallenius, Christophe Domain, Kai Nordlund, and Lorenzo Malerba, “Two-band modeling of α -prime phase formation in Fe-Cr”, *Phys. Rev. B*, **72** (2005) 214119
- [18] G.E. Lucas, “The Evolution of Mechanical Property Changes in Irradiated Austenitic Stainless Steels”, *J. Nucl. Mater.*, **206** (1993) p. 287-305
- [19] J. Friedel, “On the linear work hardening rate of face-centred cubic single crystals”, *Philosophical Magazine*, **46** (1955) p. 1169-1186
- [20] K. Sukanuma, H. Kayabo, “Irradiation hardening of Fe-Cr alloys”, *J. Nucl. Mater.*, **118** (1983) p. 234-241
- [21] R.O. Scattergood, D.J. Bacon, “The strengthening effect of voids”, *Acta Metall.*, **30** (1982) p. 1665-1677
- [22] S.M. Hafez Haghghat, R. Schaubin, D. Raabe, “Atomistic simulation of the $a(0) \langle 100 \rangle$ binary junction formation and its unzipping in body-centered cubic iron”, *Acta Mater.*, **64** (2014) p. 24-32
- [23] G.M. novotny, A.J. Ardell, “Precipitation of Al_3Sc in binary Al-Sc alloys”, *Mater. Sci. Eng. A: Struct.*, **318** (2001) p. 144-154

Chapter 4

Age-hardening Susceptibility of High-Cr ODS Ferritic Steels and SUS430 Ferritic Steel

4.1. Introduction

Oxide dispersion strengthened (ODS) steels are developed as advanced structural materials for advanced fission and fusion power systems to apply for high operation temperatures [1-3]. For high-Cr ODS ferritic steels, the most critical issue for the application to Supercritical Water Reactor (SCWR) and Lead Cooled Fast Reactor (LFR) is to improve their corrosion resistance [4-6]. The corrosion resistance of ODS steels increases with increasing chromium concentration [7].

However, a “trade-off” corrosion resistance and aging embrittlement is an issue for the practical application of high-Cr ODS ferritic steels. The formation of nano-sized Cr-rich precipitates in the bulk during operation has been known to be the cause of hardening and embrittlement after thermal aging [8-10]. As discussed in Chapter 1, there have been some researches on the effects of aging on high-Cr ODS steels, but still limited data is available for long-term aging effects on high-Cr ODS steels, especially on the correlation of mechanical property changes and microstructures.

In this study, the age-hardening susceptibility of 15Cr-ODS ferritic steel was compared with a conventional SUS430 ferritic steel as well as 12Cr-ODS ferritic steel with focusing on the α/α' phase decomposition behavior, by using TEM observation, tensile and small-punch tests.

4.2. Experimental

4.2.1. Materials

The materials used in this study were 12 wt.% Cr-ODS, 15 wt.% Cr-ODS and SUS430 ferritic steels (16 wt.% Cr). The SUS430 steel was commercially manufactured by the Nilaco Corporation. The fabrication process of ODS steels is represented in figure 4-1. In argon atmosphere, the elemental powders with a particle size of less than 10 μm were first mechanically alloyed with pre-alloyed Y_2O_3 powder of 2 μm mean diameter. During the mechanical alloying, pure titanium was also added to form finer dispersoids in the matrix. The

milling was operated at a 250 rpm rotation speed for 48 hr. The mechanically alloyed powders were then canned and degassed at a temperature of 400 °C in a 10^{-3} Pa vacuum for 3 hr. Hot-extrusion was conducted at 1150 °C to fabricate cylindrical rods of 30 mm diameter. Finally a homogenization heat treatment was performed at 1150 °C for 1hr.

Table 4-1 shows the chemical compositions of SUS430 ferritic steel, and high-Cr ODS ferritic steels produced by mechanical alloying and hot-extrusion.

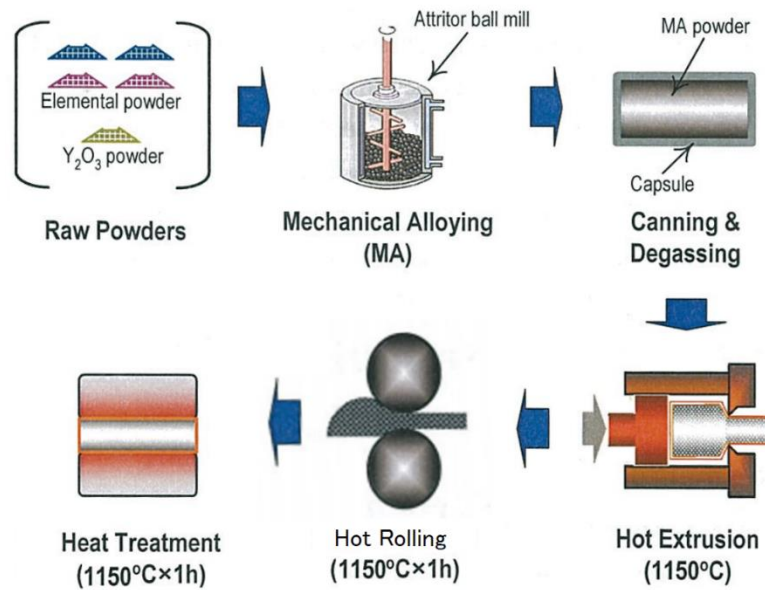


Figure 4-1 Fabrication process of the high-Cr ODS ferritic steels.

Table 4-1 Chemical compositions of the investigated steels (wt.%).

Material	12Cr-ODS	15Cr-ODS	SUS430
C	0.035	0.02	0.018
Cr	11.7	14.9	16
W	1.92	1.92	-
Ti	0.29	0.29	-
Si	-	-	0.15
Mn	-	-	0.74
Ni	-	-	0.28
Y ₂ O ₃	0.23	0.34	-
Fe	Bal.	Bal.	Bal.

4.2.2. Mechanical property tests

Hardness measurements were performed after aging for different periods. The surface of the specimen was mechanically polished with emery SiC papers until #4000, and followed by buff-polished with diamond paste until 1 μm diameter. Tensile tests with miniaturized specimens were performed at room temperature. Tensile specimens were punched from a 0.6 mm thick plate parallel to the cold-rolling direction and mechanically ground to about 0.5 mm in thickness. The dimensions of tensile specimens are 16 mm length \times 4 mm width \times 0.5 mm thickness.

In order to draw a ductile-brittle transition curve, small-punch (SP) test [12, 13] was performed by a fracture and toughness testing machine (Instron8562 type). The specimen geometry selected for this work was a 3 mm diameter, 0.3 mm thick disc. Figure 4-2 shows the sketch map of SP test. The specimens were loaded via a centrally located pushing rod and a steel ball. A new ball was used for each punch test. The load was measured using a 50 kN load cell mounted in the loading trains, and the displacement was obtained from a pair of clip gauges attached to the pushing load. The tests were carried out quasi-statically in displacement control at a cross head speed of 0.2 mm/min. Tests at low temperatures were performed by immersing the punch test dies in an insulated bath of liquid nitrogen. A thermal couple was inserted into the die 5 mm away from the specimen to monitor the temperature to an accuracy of ± 2 $^{\circ}\text{C}$. Punch tests were conducted over the temperature range $+20$ $^{\circ}\text{C}$ to -196 $^{\circ}\text{C}$ in order to generate ductile-brittle transition curve. The fracture energy of the small-punch test was determined by the area under the load-deflection curve per unit thickness of the given specimen.

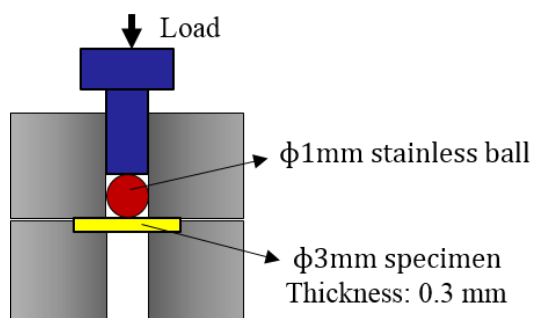


Figure 4-2 Sketch map of small-punch test.

4.2.3. Microstructural observation

Disk-type specimens of 3 mm diameter for TEM observation were punched out from a 0.3 mm thick plate and mechanically grounded to about 50 μm in thickness. And then they were electrolytic polished using a twin-jet polisher. The grain boundaries and precipitates were by examined by the TEM with an acceleration voltage of 200 kV. An FE-TEM (JEOL, 2200FS) was used to obtain high-resolution TEM images of the precipitates. The ruptured surfaces before and after tensile tests were observed by SEM.

4.2.4. Thermal aging condition

Figure 4-3 shows the schematic view of thermal aging experimental details and process. For SUS430 ferritic steel, all the samples were punched from TD-RD plane. For ODS steels, all the specimens were punched from RD-ND plane. The tensile and small punch specimens were sampled from the extruded bar, so that the longitude direction of the specimens is parallel to the extrusion direction. Some of specimens were sealed in ampoules in high vacuum conditions (10^{-4} Pa) and isothermally aged at 475 $^{\circ}\text{C}$ for up to 10,000 hr. After thermal aging, samples were took out from isothermal furnace and quenched immediately into iced water.

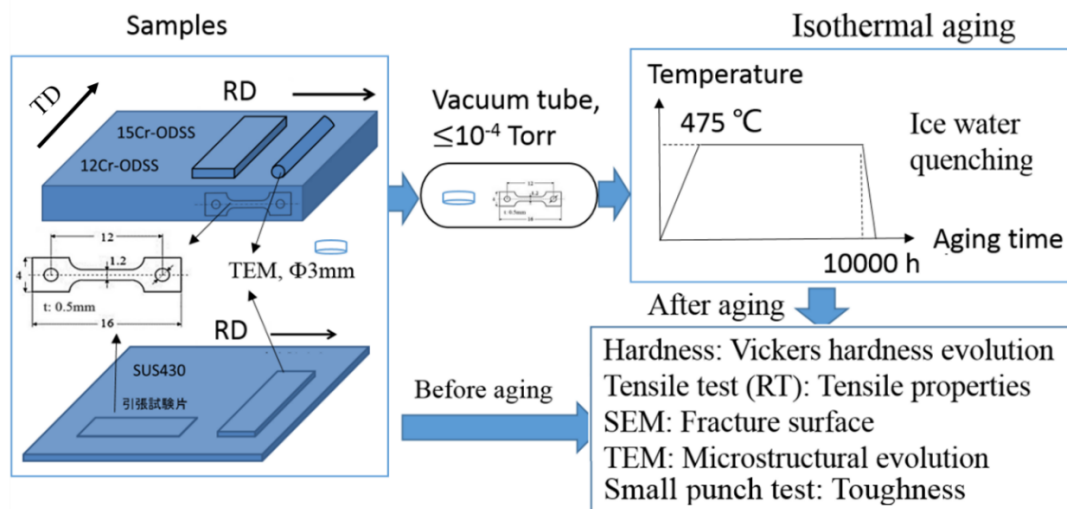


Figure 4-3 Schematic view of thermal aging experimental details and process.

4.3. Results

4.3.1. Mechanical property changes

4.3.1.1. Vickers hardness evolution

Figure 4-4 provides the evolution of Vickers hardness (HV) and the increment in Vickers hardness (Δ HV) of 15Cr-ODS, 12Cr-ODS and SUS430 ferritic steels during aging at 475 °C for up to 10,000 h. Thermal aging leads to an increase of hardness in the order of SUS430, 15Cr-ODS and 12Cr-ODS. Both of SUS430 and 15Cr-ODS show obvious hardness increase, while 12Cr-ODS only shows a small change of hardness. When aging time increases to 10,000 h, the age-hardening of SUS430 seems to be saturated because of almost no hardness change as compared to the peak value. It can be said that there is slight hardness decrease for 15Cr-ODS, which indicates over-aging may occur.

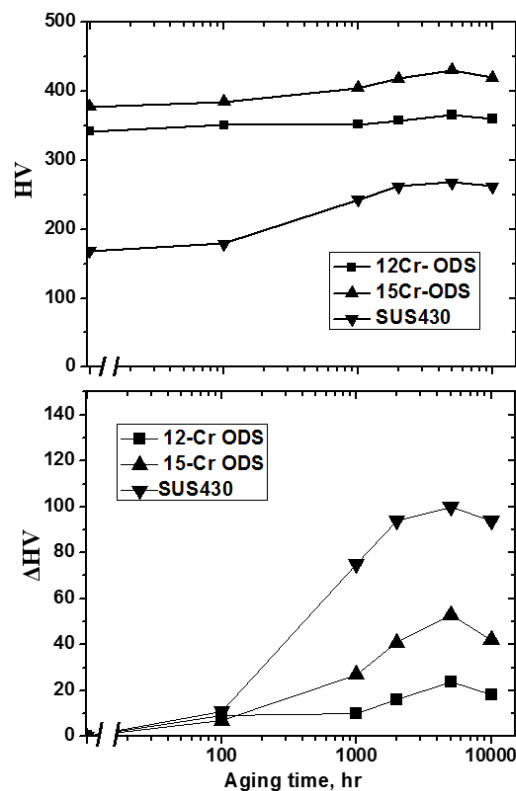


Figure 4-4 Vickers hardness (HV) and the increment in Vickers hardness (Δ HV) of each material as a function of aging time during aging at 475 °C.

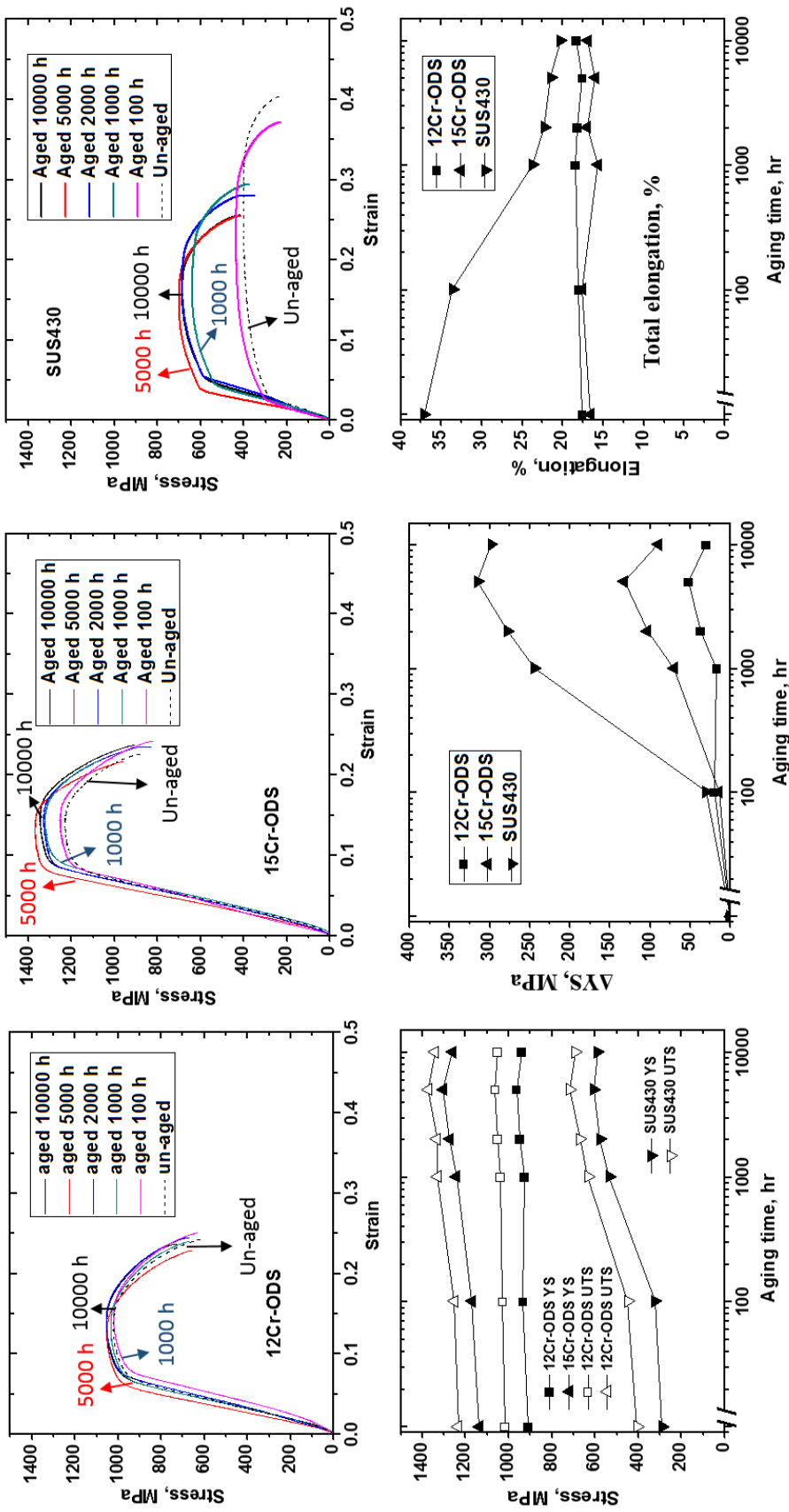


Figure 4-5 Strain-stress curves of 12Cr-ODS, 15Cr-ODS and SUS430 after aged for different time.

4.3.1.2. Tensile property changes

The effects of thermal aging up to 10,000 h on tensile stress-strain curves and tensile property changes are presented in figure 4-5. Before aging, as expected, ODS ferritic steels show excellent strength as relative to SUS430 ferritic steel. As aging time increases to 1000 h, a significant increase in yield stress and a decrease in total elongation can be observed in SUS430, while the change in yield stress is not so remarkable in 15Cr-ODS and there is almost no yield stress change for 12Cr-ODS. The evolutions of yield stress and ultimate tensile stress are in good agreement with micro-hardness measurements results. However, a characteristic of ODS steels is that age-hardening is not accompanied by a significant decrease in total elongation observed in SUS430. For example, as aging time increases to 5000 h, thermal aging of SUS430 results in 315 MPa yield stress increase with total elongation decreasing from 37% to 22%. In contrast, for 15Cr-ODS, aging for 5000 h results in smaller yield stress increase (131MPa) for 15Cr-ODS with only a very small reduction of total elongation.

Age-hardening ratio is defined as: $\Delta\sigma_y/\sigma_0$, the ratio of increment in yield stress ($\Delta\sigma_y$) and initial value of yield stress, σ_0 . Figure 4-6 shows the evolution of age-hardening ratio for each material. Although the Cr concentration is not so different between SUS430 (16 wt.%) and 15Cr-ODS, SUS430 shows a remarkable age-hardening, while 15Cr-ODS shows a small age-hardening. For example, after aging for 5000 h, the yield stress of SUS430 is about twice larger than the initial value. While there is only about 10% change of yield stress of 15Cr-ODS after the same aging time. For 12Cr-ODS, there is almost no change in the yield stress. This means both of 15Cr-ODS and 12Cr-ODS are very resistant to hardening caused by thermal aging. It seems that the difference in age-hardening ratio is due to the different Cr concentration in matrix.

In order to know the relationship between the age-hardening and the loss of ductility, $\Delta\sigma_y/\sigma_0$ as a function of ductility loss ratio, $\Delta\varepsilon/\varepsilon_0$, of each material is shown in figure 4-7. A significant increase in age-hardening with a remarkable decrease in ductility loss can be observed for SUS430 steel. A linear relation can be drawn for SUS430, which suggests that age-hardening is the main reason for the ductility loss. However, there is no this kind of

relation for both of 15Cr-ODS and 12Cr-ODS.

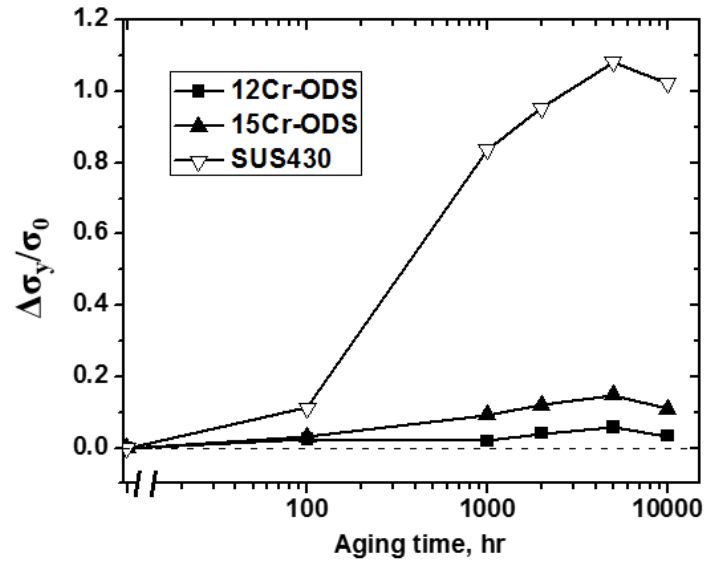


Figure 4-6 Evolution of age-hardening ratio, $\Delta\sigma_y/\sigma_0$, of each materials.

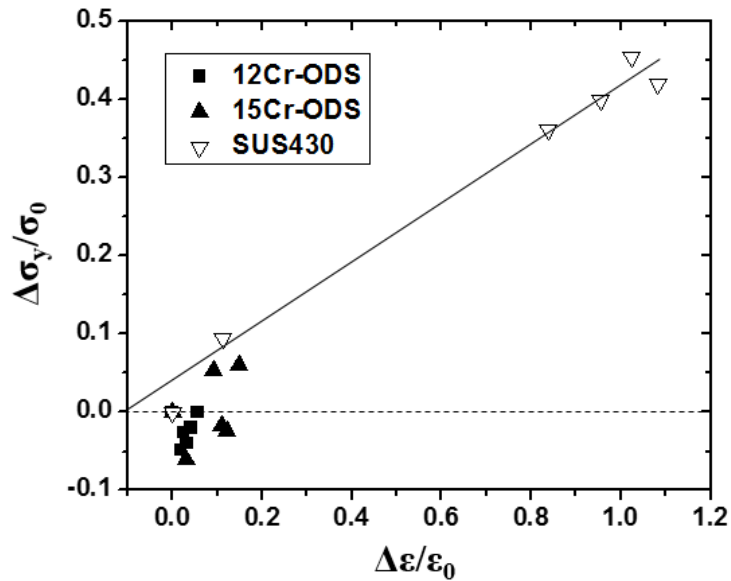


Figure 4-7 Age-hardening ratio, $\Delta\sigma_y/\sigma_0$, as a function of ductility loss ratio, $\Delta\varepsilon/\varepsilon_0$ of each material.

4.3.1.3. Small punch (SP) tests

In order to know the effect of thermal aging on toughness, small-punch tests were performed. The load-deflection curves of SUS430 and 15Cr-ODS before and after aging for 2000 h are presented in figure 4-8. During the test, the deformation mode of the specimen

changes successively. The deformation mode can be described by four stages: (a) elastic bending, (b) plastic bending, (c) plastic membrane stretching, and (d) plastic instability development stages. In addition, when testing temperature decreases, the maximum loads at first increase followed by a decrease for all the material

In order to evaluate the ductile-brittle transition temperature, the absorbed energies of small-punch tests were calculated as an area below the SP curve. The absorbed energy is calculated as:

$$E = A + B \cdot \tanh((T - T_0) / C) \quad (4.1)$$

where E is the absorbed small punch energy; A , B , C are parameters; $A + B$ is upper shelf energy; T is test temperature; T_0 is ductile-brittle transition temperature (DBTT).

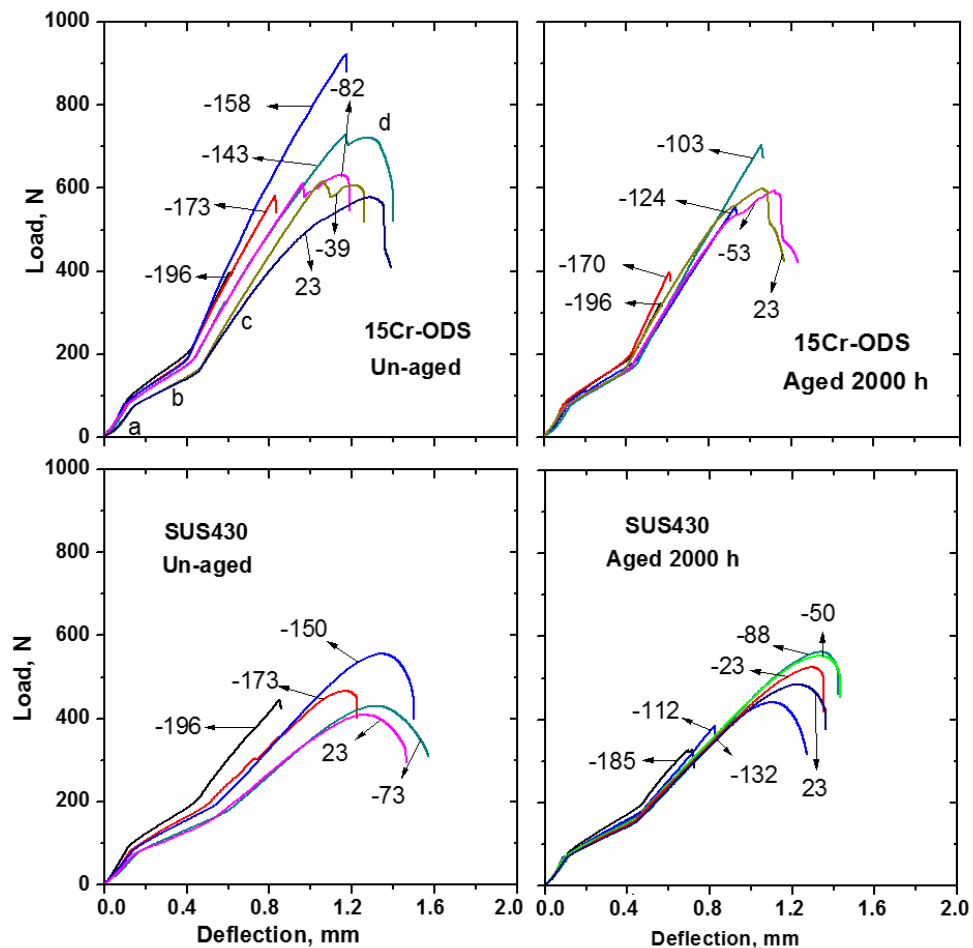


Figure 4-8 Small punch load-deflection curves of 15Cr-ODS and SUS430 before and after aging for 2000 h.

Figure 4-9 shows the ductile-brittle transition curves of SUS430 and 15Cr-ODS at different conditions: unaged and aged at 475 °C for 2000 h. The ductile-brittle transition curves show the same general trends. Firstly, the SP-DBTT was similar between two steels: -174 °C for SUS430 and -175 °C for 15Cr-ODS. Secondly, both of them show aging effects: an increase in SP-DBTT but no or very small reduction in upper shelf energy.

The aged materials show a few differences compared with the unaged materials. Firstly, there is a larger increase of SP-DBTT in aged SUS430. The shifts of SP-DBTT are 62 °C in SUS430 and 40 °C in 15Cr-ODS, respectively. Secondly, the temperature range of ductile to brittle transition in aged 15Cr-ODS appears to be larger than that in aged SUS430.

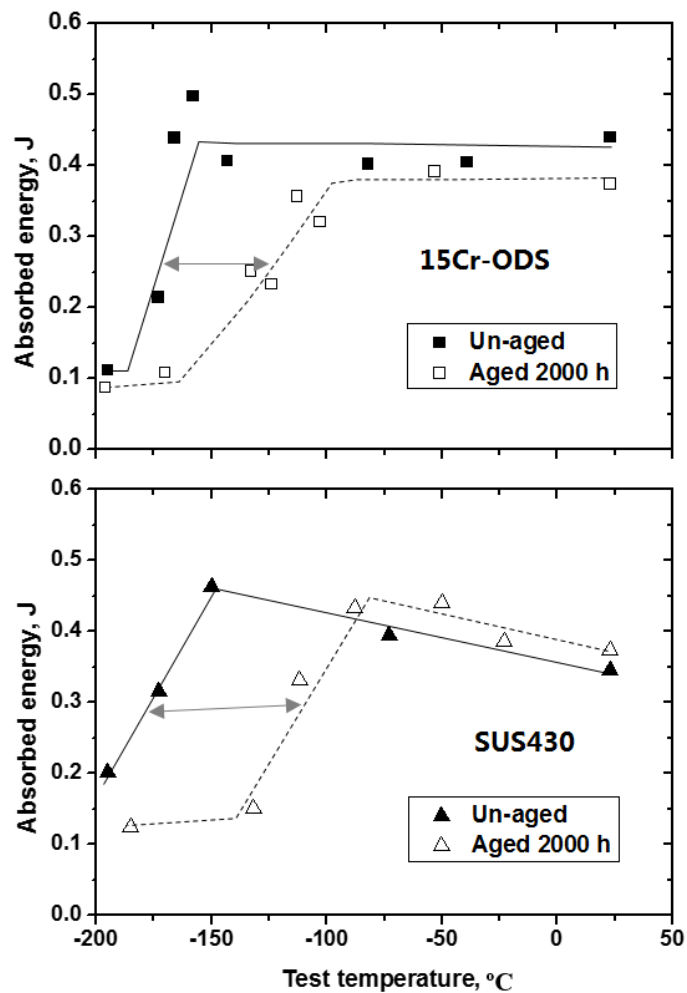


Figure 4-9 Small-punch (SP) absorbed energy as a function of testing temperature showing the ductile-brittle transition curves of SUS430 and 15Cr-ODS before and after aging for 2000 h.

4.3.2. Microstructures

4.3.2.1. TEM microstructures

In order to know the reason why age-hardening occurred in SUS430 and 15Cr-ODS, TEM was used to observe the corresponding microstructural changes. Figure 4-10(a-f) provide the TEM bright field images of SUS430 and 15Cr-ODS before and after aging for 5000 h. Figure 4-10(a) shows the microstructure of as-received SUS430, which contains almost no precipitates and large grain size. In contrast, as-received 15Cr-ODS presents very fine elongated grains and finely dispersed nano-sized oxide particles, as shown in figures 4-10(d) and 4-10(e). 15Cr-ODS has an average grain size of 0.5 μm with shorter grain size 0.2 μm and longer grain size 0.8 μm . As shown in figure 4-10(b), after aging for 2000 h, SUS430 presents a large number of α' precipitates and some amount of dislocations. When aging time increases to 5000 h, the size of α' precipitates becomes larger, with an average size of 10.5 nm and a number density of $6.1 \times 10^{22} \text{ m}^{-3}$, as presented in figure 4-10(c). Some large precipitates were analysed by TEM-EDX showing that they are mainly Cr-Mn-Si rich G phases, as presented in figure 4-11, while most of the precipitates are α' phases; the volume fraction of G phases is quite low with a number density $\sim 10^{18} \text{ m}^{-3}$.

Before aging, 15Cr-ODS contains a finely dispersed oxide particles with an average size of 4.2 nm and a number density of $1.3 \times 10^{23} \text{ m}^{-3}$. Most of the oxide particles in 15Cr-ODS are identified as Y-Ti-O rich particles, as illustrated in figure 4-12, which provides the EDX spectrum of one oxide particle. After aging for 5000 h, a complex precipitation structure can be observed in 15Cr-ODS, as shown in figure 4-10(f). It is considered that oxide particles are quite stable during aging at 475 $^{\circ}\text{C}$ [14].

Figure 4-13 shows the particle distribution in 15Cr-ODS before and after aging for 5000 h. After aging, particle distribution map shows a bio-model distribution in the PSD, which is due to the formation of α' precipitates. The average size and number density of α' precipitates are calculated as 8.1 nm and $1.6 \times 10^{22} \text{ m}^{-3}$, respectively. In addition, there are very few M_{23}C_6 carbides in matrix and some carbides on grain boundaries, as shown in figure 4-10(f). These carbides might form during the early stage of thermal aging.

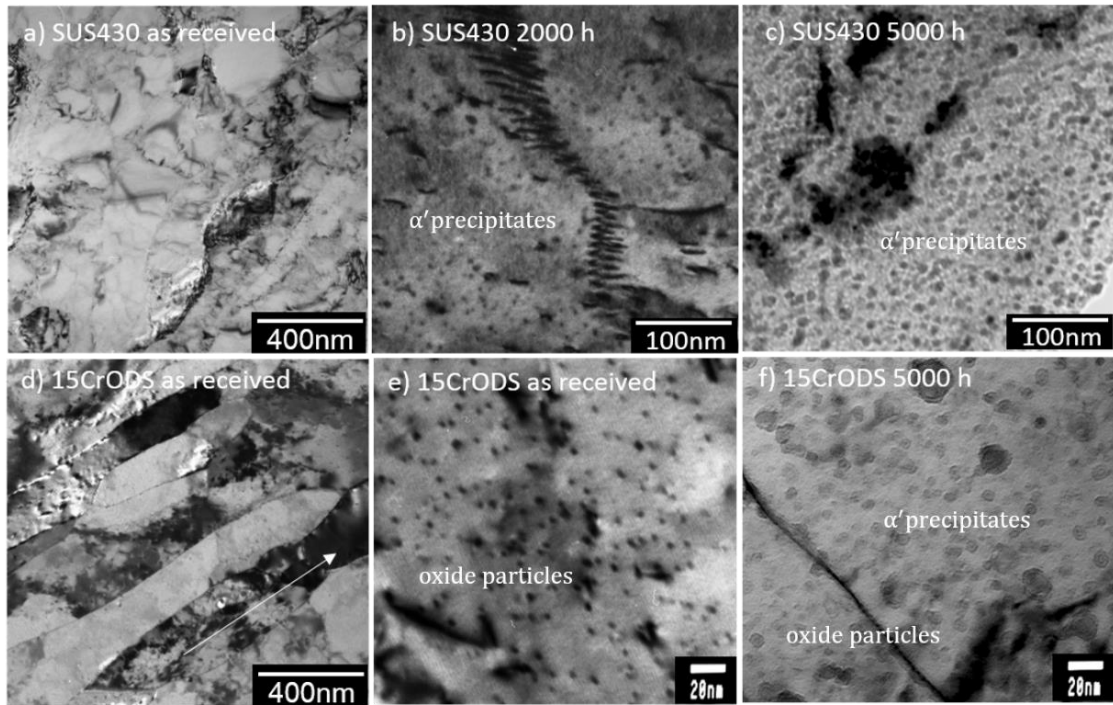


Figure 4-10 TEM bright field images of (a) SUS430, as received; (b) SUS430, aged for 2000 h; (c) SUS430, aged for 5000 h; (d) 15Cr-ODS, as received; (e) 15Cr-ODS, as received showing the dispersion of oxide particles; (f) 15Cr-ODS, aged for 5000 h.

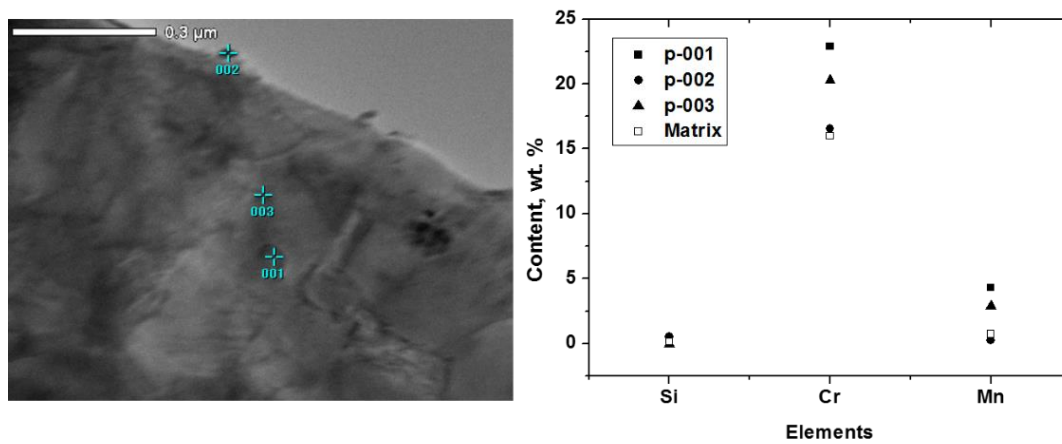


Figure 4-11 TEM EDX point analyses showing chemical components of precipitates in SUS430 after aging for 5000 h.

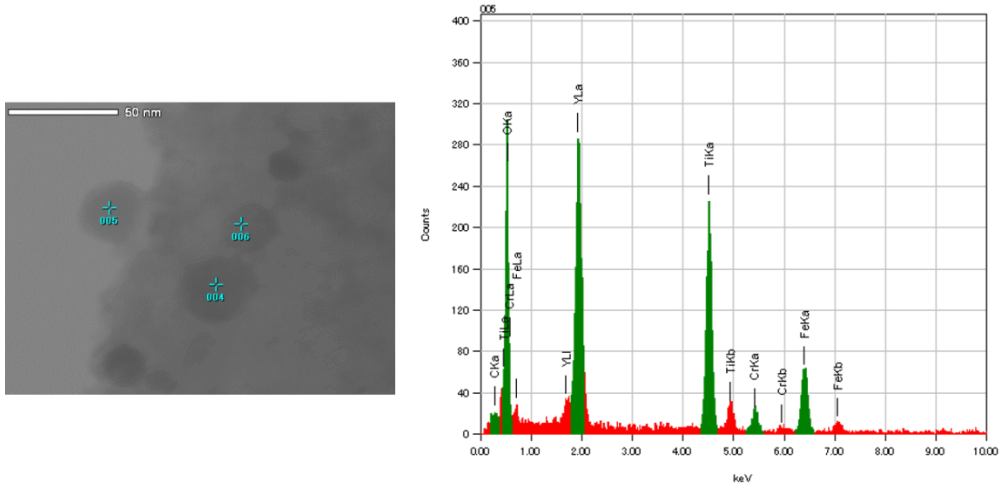


Figure 4-12 TEM EDX spectrum showing Y-Ti-O enriched oxide particle in as-received 15Cr-ODS.

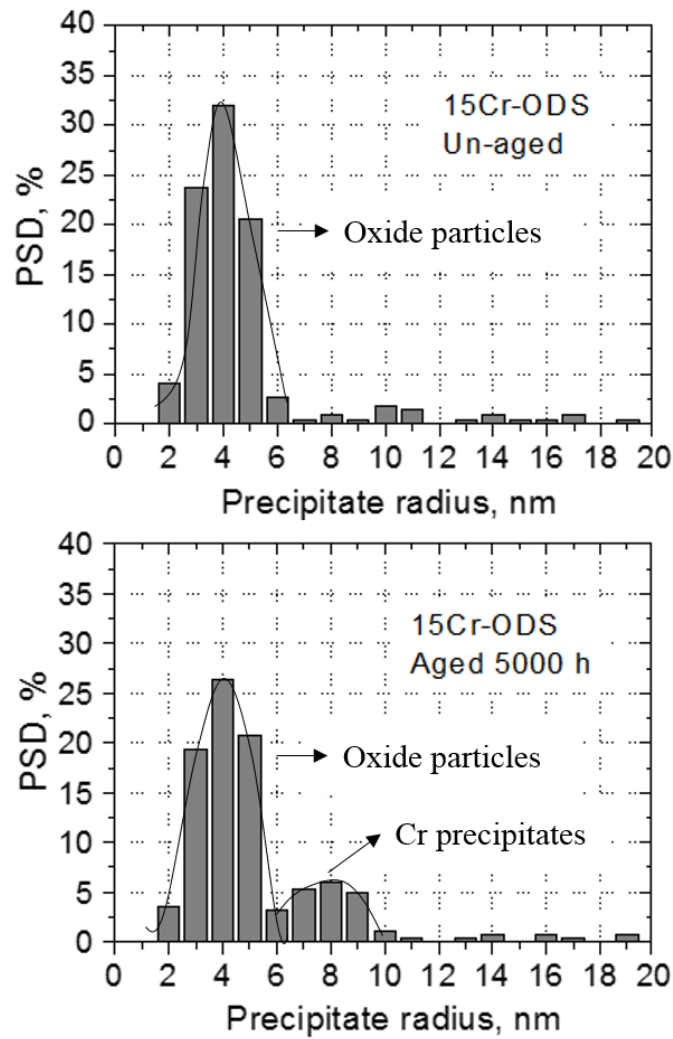


Figure 4-13 Particles size distribution (PSD) in 15Cr-ODS before and after aging for 5000 h.

4.3.2.2. High-resolution TEM images

The α' -rich clusters have a b.c.c. structure with a lattice parameter $a_{Cr}=2.88 \text{ \AA}$. This structure is close to the α -Fe b.c.c. structure with a lattice parameter $a_{Fe}=2.87 \text{ \AA}$. Thus, a misfitting coherent relationship between these two phases is expected. A high-resolution image of a α' precipitate embedded in α matrix is presented in figure 4-14(a-c). There is a cube-on cube orientation relation ($\langle 111 \rangle_{Cr} // \langle 111 \rangle_{Fe}$, $\{111\}_{Cr} // \{111\}_{Fe}$) between the α -Fe lattice and the α' -Cr lattice. The schema represented in figure 4-14(d) shows the strained interface structure between the α' and α phases and highlights the misfit dislocations accommodating the strain due to lattice parameter difference. Thus α' -Cr clusters are semi-coherent at current aging time.

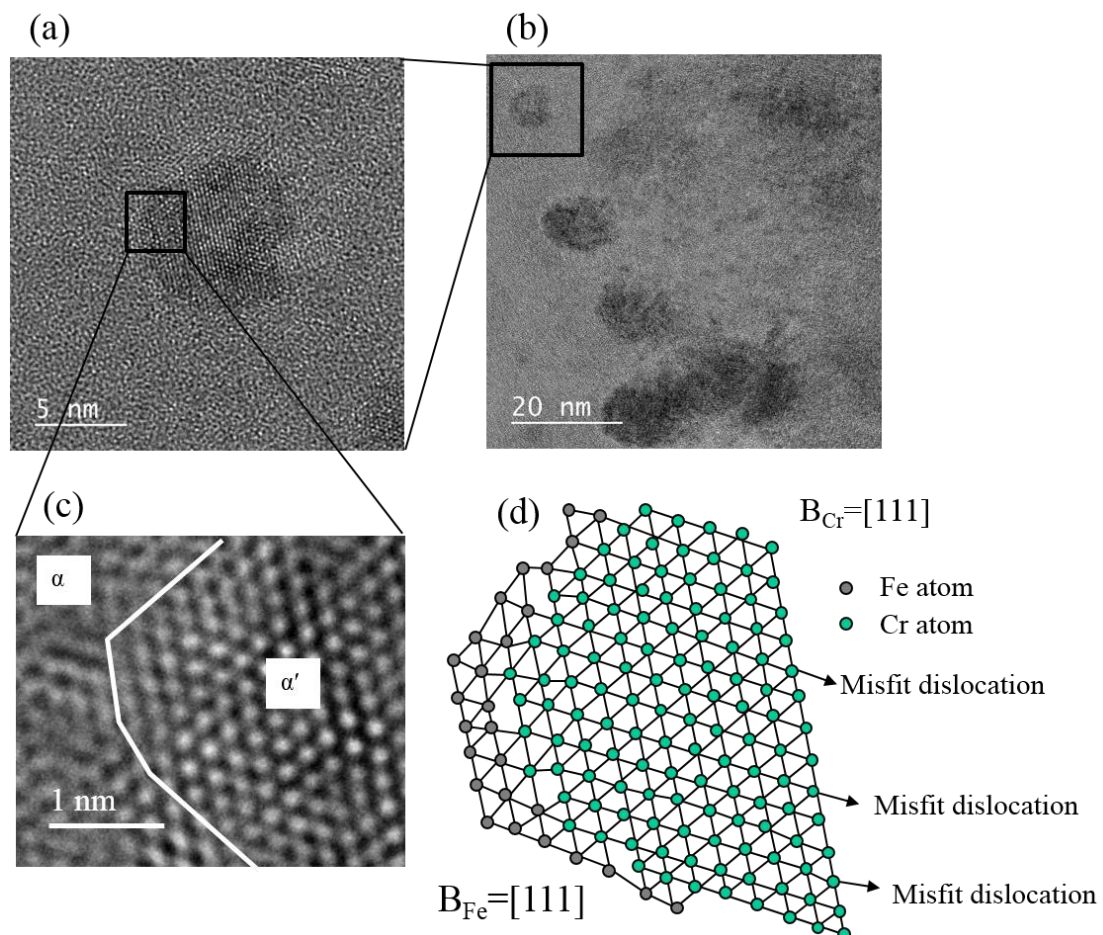


Figure 4-14 (a) and (b) showing high-resolution TEM images of SUS430 after aging for 10,000 h; (c) HR-TEM of the interface between the α matrix and the α' particle; (d) corresponding schema of the interface.

4.3.2.3. Rupture surfaces

To investigate the rupture behavior, SEM observations of the ruptured surface of tensile specimens after RT testing were carried out. Figure 4-15 presents the ruptured surfaces and reduction in area (RA) of 12Cr-ODS, 15Cr-ODS and SUS430 before and after aging for 5000 h. All the steels still show a ductile rupture manner even after aging for 5000 h; a typical dimple rupture surface can be observed for all the materials. The difference between SUS430 and ODS steels is the RA and the change in RA. Before aging, the RA of SUS430 is about 82 %, which is quite larger than that of 12-ODS (68%) and 15Cr-ODS (62%). In contrast, thermal aging results in the change in the RA in the order of SUS430, 15Cr-ODS and 12Cr-ODS, where the reduction is 13%, 8% and 4%, respectively. These results are in good agreement with the change in hardness and yield stress, which also change in the same order. While the change in total elongation does not represent the change in age-hardening. It seems that the change in RA is more sensitive to age-hardening than the change in total elongation.

4.3.2.4. SP Fracture surfaces

The toughness of 15Cr-ODS and SUS430 has been successfully evaluated by small-punch tests. In order to investigate the effect of thermal aging on the fracture behavior, SEM was used to observe the fracture surfaces of 15Cr-ODS and SUS430 tested at different temperatures, which are shown in figure 4-16. There is no big difference in the fracture manner of 15Cr-ODS and SUS430; both of them show a manner of ductile fracture at room temperature and a manner of brittle fracture at liquid nitrogen temperature. However, detailed observations of the fracture surfaces revealed that a delamination fracture was observed in as-received 15Cr-ODS when tested at 100 K. In the crack-arrester mode, the delamination is thought to relax the triaxial stress condition and to blunt the crack tip. In addition, big crack can be observed in the disc sample of as-received 15Cr-ODS when test temperature decreases to 78 K. And the temperature required for the occurrence of cracking increases to 103 K for 15Cr-ODS after aged for 2000 h. The reason why delamination and crack are produced parallel to rolling direction might be related to the strong texture in hot-extruded and rolled 15Cr-ODS steel.

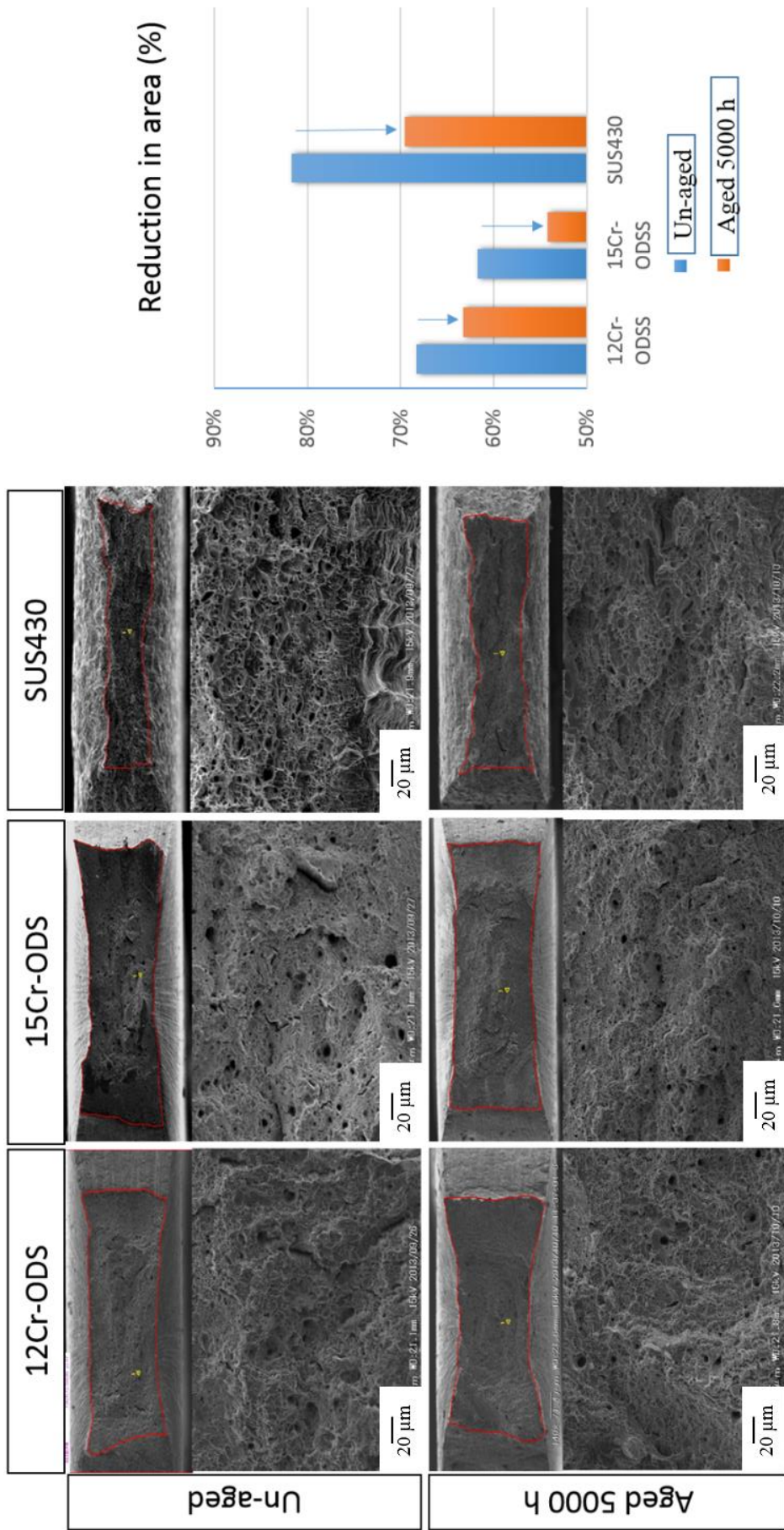


Figure 4-15 Ruptured surface and reduction area of each material before and after aging for 5000 h.

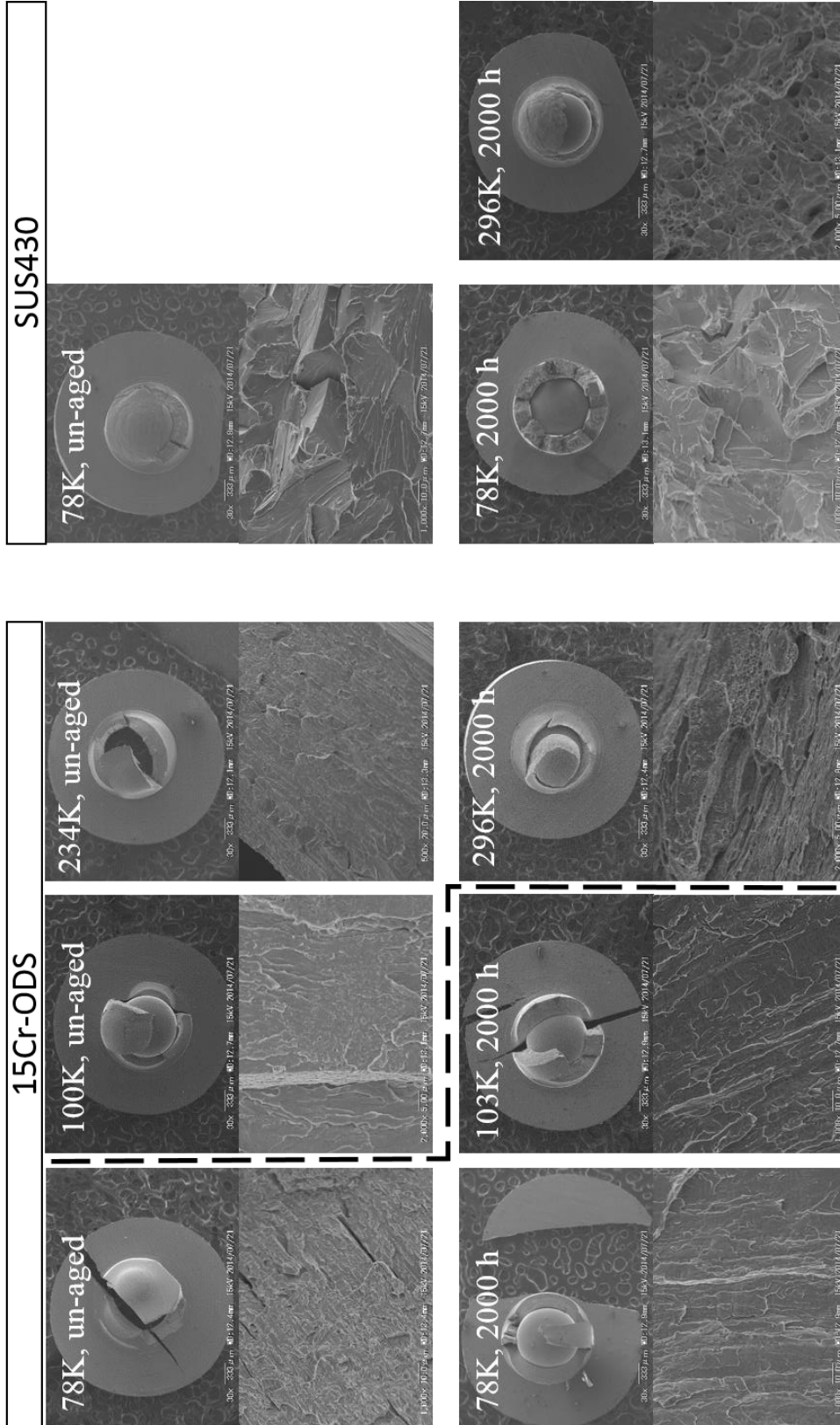


Figure 4-16 Fracture surfaces of 15Cr-ODS and SUS430 before and after aging for 2000 h.

4.4. Discussion

4.4.1. Correlation of age-hardening with microstructure evolution

Thermal aging leads to a significant increase in hardness and strength in SUS430 and 15Cr-ODS, while 12Cr-ODS shows almost no age-hardening. TEM microstructure observations reveals that there are a large amount of α' precipitates formed in SUS430 and 15Cr-ODS. Detailed TEM-EDX analyses suggest that there are few G phases in SUS430 after aging for 5000 h; while the volume of G phases is quite lower than α' precipitates. 15Cr-ODS contains very few amount of carbides, which are expected to have a limited contribution to the age-hardening [15]. Therefore, age-hardening in SUS430 and 15Cr-ODS is mainly due to α/α' phase decomposition.

After aging for 5000 h, SUS430 shows almost twice larger increase in yield stress than 15Cr-ODS. This means SUS430 has a higher age-hardening susceptibility than 15Cr-ODS. There are two factors that may affect the age-hardening behaviors: one is Cr concentration in matrix before aging, the other is trapping effect of oxide particles. As for the first factor, the effect of Cr concentration on nucleation rate of α' precipitates has been studied by D. Schwen [16], who showed that nucleation rates depended on matrix concentration of Cr and thermal aging temperature. In this study, SUS430 has a little higher Cr concentration (16 wt.%) than 15Cr-ODS (15 wt.%), but the influence of this difference in Cr content is not significant. As for the second factor, oxide particles can act as trapping site for defects and may influence Fe/Cr phase decomposition.

4.4.2. Nucleation rate

P.J. Grobner's [17] study indicated that 475 °C embrittlement was evidently determined by the kinetics of α' formation, and the nucleation process was more important of the two processes (nucleation and growth) with respect to the effect on age-hardening. The nucleation process in solid solutions has been studied by many investigators.

According to Becker's theory [18], nucleation rate, J is:

$$J = C \exp - \left(\frac{Q + F_0}{RT} \right) \quad (4.2)$$

where C is constant, R is the gas constant, T is the absolute temperature. Q is the activation energy of diffusion of chromium (81 kJ mol^{-1} [19]), F_0 is the energy to form a nucleus of critical size.

$$F_0 = \frac{4F_2^3}{27F_1^2} \quad (4.3)$$

$$F_2 = A(N_s - N_p)^2 \eta \quad (4.4)$$

F_1 is the driving force of the precipitation of the α' phase and can be derived graphically from a free energy diagram, as demonstrated in figure 4-17. The free energy of the precipitating phase in equilibrium at a given temperature is determined by a common tangent to the free energy-composition curve (point G_p at N_p). F_2 [20] is proportional to the surface of the nucleus, and representative of the surface energy. A is binding energy in the crystal of the solid solution temperature independent (1.07 kJ mol^{-1}). N_s is the atomic fraction of the initial solid solution, N_p is the atomic fraction corresponding to the precipitating phase, η is shape factor (3).

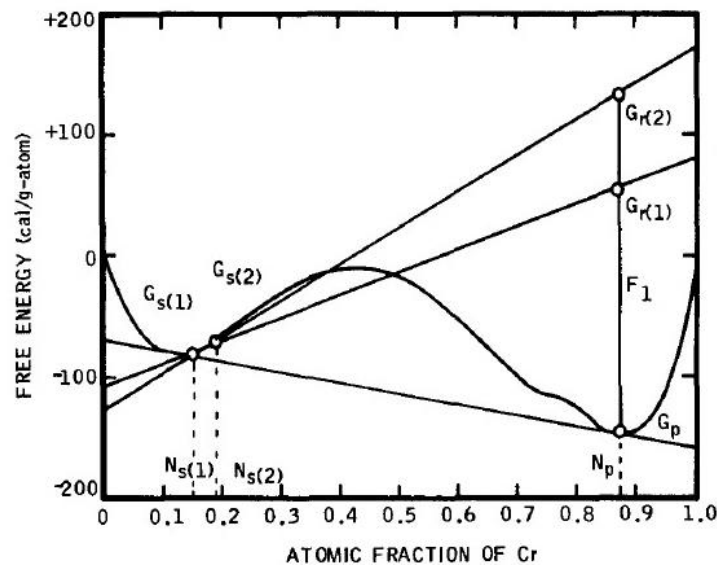


Figure 4-17 Free energy diagram of the Fe-Cr system at 475 °C [21].

The nucleation rate defines the number of nuclei causing embrittlement:

$$J = \frac{n_c}{t_c} \quad (4.5)$$

The time for embrittlement can be defined as:

$$t_c = \frac{n_c}{C} \exp \frac{Q + F_0}{RT} \quad (4.6)$$

Table 4-2 shows the calculation result of the nucleation rate of α' phase in each material. SUS430 has a higher driving force energy and a lower surface energy of nucleus than the ODS steels. The calculation results can only reveal an ideal case without considering other factors that affect α/α' phase decomposition. Thermal aging at 475 °C leads to a nucleation rate in the order of SUS430, 15Cr-ODS and 12Cr-ODS, which shows a good agreement with age-hardening level of the materials. And the time required for embrittlement follows an opposite order of 12Cr-ODS, 15Cr-ODS and SUS430. This means that 12Cr-ODS needs the longest time to become brittle.

Table 4-2. Calculation of the nucleation rate of α' phase of each material.

Materials	N_p	N_s	$(N_s - N_p)^2$	F_1, J	F_2, J	F_0, J	$\exp -\frac{Q + F_0}{RT}$	$\exp \frac{Q + F_0}{RT}$
12Cr-ODS	0.88	0.13	0.56	749	5.05×10^3	3.40×10^4	3.85×10^{-19}	2.60×10^{18}
15Cr-ODS	0.88	0.16	0.52	950	4.76×10^3	1.77×10^4	5.21×10^{-18}	1.92×10^{17}
SUS430	0.88	0.17	0.50	1017	4.62×10^3	1.42×10^4	9.17×10^{-18}	1.09×10^{17}

4.4.3. Age-hardening mechanism

The change in yield stress ($\Delta\sigma_y$) can be interpreted in terms of Orowan-type obstacle mechanism, and it is estimated from a dispersed hardening model [22, 23]:

$$\Delta\sigma_y = M\alpha Gb (Nd)^{1/2} \quad (4.7)$$

where M is the Taylor factor (3.06), α is the strength factor (0.2 [23, 24] for Cr precipitates, at room temperature), G is the shear modulus, b is the Burgers vector (0.248 nm), N and d is the number density and the average diameter of α' particles, respectively.

Table 4-3 summarizes the values of estimated increment in yield stress ($\Delta\sigma_y^e$) and $\Delta\sigma_y^m$, the measured increment in yield stress. 15Cr-ODS shows larger average dislocation passage distance than SUS430. The free dislocation passage distance is defined as $L = (Nd)^{-1/2}$. For the

increment in yield stress, the estimated results agree with measured results, which indicates age-hardening is mainly due to α/α' phase decomposition.

Oxide particles may work as trapping sites for point defects because defect formation energy is lower at interfaces than that in the bulk [25]. It is considered that finely dispersed nano-sized oxide particles in ODS steels can influence the diffusion rate of Cr by trapping vacancies caused by thermal aging. To some extent, oxide particles may influence the α/α' phase decomposition kinetics. Both of phase decomposition evaluation and tensile test results indicate that 15Cr-ODS steel shows a lower age-hardening susceptibility than SUS430. Oxide particles play a role in retarding α/α' phase decomposition process and suppressing the ductility loss.

Table 4-3 Estimated and measured values of increment in yield stress.

Materials	Parameter		Estimated	Measured
	G , MPa	L , nm	$\Delta\sigma_y^e$, MPa	$\Delta\sigma_y^m$, MPa
15Cr-ODS	75.3×10^3	85	122	131
SUS430	77.2×10^3	39.5	290	315

4.4.4. Mechanism of no-loss-of-elongation

The other characteristic feature than the small age hardening observed in ODS steel is no loss of tensile elongation, as shown in figure 4-5. In the case of ferritic steel, the reduction of total elongation is proportional to the amount of age-hardening, that is, age-hardening is accompanied by aging embrittlement. However, the fracture mode is still ductile mode showing many dimples on the fractured surfaces with an enough reduction in area. In general, hardened materials exhibit less work hardening behavior and result in so-called necking with a localized slip. Consequently, total elongation is reduced by age hardening.

However, in ODS steel, age hardening is not accompanied by loss of total elongation. This is interpreted in terms of continuous dislocation source activation model as follows. In poly crystals, triple point of grain boundaries can be the dislocation source because the grain strains are accumulated at the point. ODS steel consists of fine grains less than 0.5 μm ,

indicating that the steel has a number of dislocation sources which are activated continuously and resultantly homogeneous deformation occurs even after age hardening. Thus, in ODS steel, sub-micron sized grains suppress the localized slip that reduces total elongation by offering a number of dislocation sources.

4.5. Summary

The age-hardening susceptibility of 15Cr-ODS steel has been compared with the conventional SUS430 steel and 12Cr-ODS steel after isothermal aging at 475 °C up to 10,000 h. The obtained results are as follows:

- (1) After thermal aging, SUS430 steel shows a larger increase in hardness and strength than 15Cr-ODS steel, while there is almost no hardening for 12Cr-ODS steel. A characteristic of the ODS steels is that the hardening is not accompanied by a remarkable ductility loss that is observed in SUS430 steel.
- (2) The results of small punch test suggest that SUS430 suffers a larger DBTT shift to higher temperature than that for 15Cr-ODS, which is agree with the tensile test results. No remarkable change in fracture mode was observed after aging for 10,000 h, and all the materials still present ductile fracture at room temperature.
- (3) TEM EDX analyses indicate that thermally aged SUS430 contains quite small amount of G phases enriched with Cr-Mn-Si. Very few $M_{23}C_6$ carbides are observed in 15Cr-ODS. After 10,000 h aging, the Cr precipitates are found to be semi-coherent particles and have a partial cube-on-cube orientation with the Fe matrix.
- (4) The main difference of age-hardening behavior in SUS430 and ODS steels may be interpreted in terms of a nucleation rate controlling theory based on Grobner's theory. Results indicate that thermal aging results in the appearance of age-hardening in the order of SUS430, 15Cr-ODS and 12Cr-ODS, which shows a good agreement with the amount of age-hardening of the materials.
- (5) The correlation of age-hardening and α/α' phase decomposition is interpreted in terms of the Orowan type strengthening model, which indicates 15Cr-ODS has a lower age-hardening susceptibility than SUS430.

References

- [1] Kimura, R. Kasada, N. Iwata, H. Kishimoto, C.H. Zhang, J. Isselin, P. Dou et al. “Development of Al added high-Cr ODS steels for fuel cladding of next generation nuclear systems”, *J. Nucl. Mater.*, **417** (2011) p. 176-179
- [2] T. Yoshitake, T. Ohmori, S. Miyakawa, “Burst properties of irradiated oxide dispersion strengthened ferritic steel claddings”, *J. Nucl. Mater.*, **788** (2002) p. 307-311
- [3] S. Ukai, T. Okuda, M. Fujiwara, T. Kobayashi, S. Mizuta, H. Nakashima, “Characterization of high temperature creep properties in recrystallized 12Cr-ODS ferritic steel claddings”, *J. Nucl. Sci. Tech.*, **39** (2002) p. 872
- [4] Akihiko KIMURA, Han-Sik CHO, Naoki TODA, Ryuta KASADA, Kentaro YUTANI, Hitotatsu KISHIMOTO, Noriyuki IWATA, Shigeharu UKAI, Masayuki FUJIWARA, “High Burnup Fuel Cladding Materials R&D for Advanced Nuclear Systems: Nano-sized oxide dispersion strengthening steels”, *J. Nucl. Sci. Tech.*, **44** (2007) p. 323-328
- [5] S. Ukai, T. Nishida, T. Okuda, T. Yoshitake, “Development of oxide dispersion strengthened ferritic steels for FBR core application (II) morphology improvement by martensit by martensite transformation,” *J. Nucl. Sci. Tech.*, **35** (1998) p. 294
- [6] H. Je, A. Kimura, “Stress corrosion cracking susceptibility of oxide dispersion strengthened ferritic steel in supercritical pressurized water dissolved with different hydrogen and oxygen contents”, *Corros. Sci.*, **78** (2014) p. 193-199
- [7] H. S. Cho, A. Kimura, S. Ukai et al., “Corrosion properties of oxide dispersion strengthened steels in super-critical water environment”, *J. Nucl. Mater.*, **329–333** (2004) p. 387–391
- [8] D.A. Terentyev, G. Bonny, L. Melerba, “Strengthening due to coherent Cr precipitates in Fe-Cr alloys: atomistic simulations and theoretical models”, *Acta Mater.*, **56** (2008) p. 3229-3235
- [9] G. Bonny, D.A. Terentyev, L. Melerba, “The hardening of iron-chromium alloys under thermal aging: an atomistic study”, *J. Nucl. Mater.*, **385** (2009) p. 278-283

- [10] Cepdevila, M.K. Miller, K.F. Russell, J. Chao et al., “Phase separation in PM 2000™ Fe-base ODS alloy: experimental study at the atomic level”, *Mater. Sci. Eng. A*, **490** (2008) 277-288
- [11] A. Kimura, R. Kasada, N. Iwata, H. Kishimoto et al., “Super ODS Steels R&D for Fuel Cladding of Next Generation Nuclear Systems 1) Introduction and alloy design”, *Proc. ICAPP 09*, (2009) p. 9220
- [12] J. Isselin, R. Kasada, A. Kimura, T. Okuda, M. Inoue, S. Ukai, S. Ohnuki, T. Fujisawa, F. Abe, “Evaluation of fracture behavior of recrystallized and aged high-Cr ODS ferritic steels”, *J. Nucl. Mater.*, **417** (2011) p. 185-188
- [13] N. Okuda, R. Kasada, A. Kimura, “Statistical evaluation of anisotropic fracture behavior of ODS ferritic steels by using small punch tests”, *J. Nucl. Mater.*, **386-388** (2009) p. 974-978
- [14] J. Ribis, S. Lozano-Perez, “Nano-cluster stability following neutron irradiation in MA957 oxide dispersion strengthened material”, *J. Nucl. Mater.*, **444** (2014) p. 314-322
- [15] Chen, A. Kimura, C. Zhang, W. Han, “Effect of alloying elements on the aging embrittlement of Fe-15Cr ferritic alloys”, in *PRICM: 8 the 8th Pacific Rim International Congress on Advanced Materials and Proceeding*, (2013) p. 529-536
- [16] D. Schwen, E. Martinez, A. Caro, “On the analytic calculation of critical size for alpha prime precipitation in FeCr”, *J. Nucl. Mater.*, **439** (2013) p. 180-184
- [17] P.J. Grobner, “The 475 °C embrittlement of ferritic stainless steels”, *Metall. Trans.*, **4** (1973) p. 251
- [18] R. Becker, *Ann. Phys.*, **32** (1938) p. 128, As referred by H. Morawetz (2002) *Science*
- [19] K. Takano, H. Nitta, H. Seto, C.G. Lee, K. Yamada, Y. Yamazaki, H. Sato, S. Takeda, “Volume and dislocation diffusion of iron, chromium and cobalt in CVD β -SiC”, *Sci. Tech. of Adv. Mater.*, **2** (2001) p. 381-388
- [20] J.W. Christian, “The theory of transformations in metals and alloys”, *Pargamon Press*, (1965) p. 178
- [21] O. Kubaschewski, E.L. Evans, C.B. Alcock, “Metallurgical Thermochemistry”, (1967)
- [22] G.E. Lucas, “The evolution of mechanical property change in irradiated austenitic stainless steels”, *J. Nucl. Mater.*, **206** (1993) p. 287-305

- [23] D. Chen, A. Kimura, W. Han, "Correlation of Fe/Cr phase decomposition process and age-hardening in Fe-15Cr ferritic alloys", *J. Nucl. Mater.*, **455** (2014) p. 436-439
- [24] S.M. Hafez Haghghat, R. Schaubin, D. Raabe, "Atomistic simulation of the $a(0) \langle 100 \rangle$ binary junction formation and its unzipping in body-centered cubic iron", *Acta Mater.*, **64** (2014) p. 24-32
- [25] J. Ribis, S. Lozano-Perez, "Nano-cluster stability following neutron irradiation in MA957 oxide dispersion strengthened material", *J. Nucl. Mater.*, **444** (2014) p. 314-322

Chapter 5

Characteristic age-hardening behavior of 15Cr-ODS Ferritic Steel

5.1. Introduction

Understanding Fe/Cr (α/α') phase decomposition behavior is important for high-Cr ODS steels for application to cladding of GEN IV systems and also structural material of fusion blanket. As shown in Chapter 3 and Chapter 4, there are several factors affecting age hardening behavior in high-Cr ferritic steels, such as Cr concentration in the matrix, alloying elements and aging time. However, the α/α' phase decomposition behavior in high-Cr ODS steels remains unclear.

Helium ion-irradiation experiments of ODS ferritic steels clearly showed that the helium bubbles were formed at the interface of nano-scaled oxide particles and the matrix, indicating that helium and vacancies were easily trapped at the interface [1, 2]. It is expected that nano-scaled oxide particles may contribute to affect the α/α' phase decomposition through affecting vacancy motion that control Fe and Cr diffusion. No research, however, was conducted to investigate the effect of nano-sized oxide particles on the age-hardening behavior, that is, α/α' decomposition during thermal aging.

Because Cr-rich precipitates are coherent with matrix, there is difficulty in using conventional transmission electron microscopy (TEM) to characterize the early stages of α/α' phase decomposition [2]. Energy-filtered TEM (EFTEM) can efficiently reveal element distribution [3, 4], which provides pathway for imaging of nano-sized Cr precipitates and distinguishing Cr precipitates from oxide particles.

The goal of this work was to investigate the effect of oxide particles on α/α' phase decomposition behavior. Both conventional TEM and EFTEM were used to identify the microstructural characteristic of 15Cr-ODS steel during thermal aging. Micro-hardness and tensile tests were performed to reveal the age-hardening behavior. Fe-15Cr model alloys were compared with 15Cr-ODS steel to investigate the role of oxide particles in age-hardening.

5.2. Experimental

The materials used in this study were 15Cr-ODS steel, Fe-15Cr and Fe-15Cr-C model alloys, named 15Cr-ODS, Fe-15Cr and Fe-15Cr-C, hereinafter. The chemical compositions in %

weight are shown in Table 5-1. 15Cr-ODS was produced by mechanical alloying where the Fe-15Cr powders were mixed with the Y₂O₃ powders by a high-energy attritor in an argon atmosphere. The resultant powders were subsequently consolidated by hot extrusion and forged at 1150 °C, then annealed at 1200 °C for 1 hr. Fe-15 Cr model alloys were fabricated by arc melting methods using high purity base metals (>99.995%). The processing details are described in Chapter 2 and Chapter 4. The effect of carbon on age-hardening was also investigated for an ODS steel with addition of carbon, which cannot be easily removed during fabrication process of ODS steels.

Some specimens were sealed in ampoules in a high vacuum condition (10⁻⁴ Pa) and isothermally aged at 475 °C for up to 10, 000 hrs. Specimens for hardness measurements were mechanically grinded and polished with a grinder using SiC paper and finally with a polishing buffer using 1 μm diamond paste. Vickers hardness was measured with a 1 kg load. At least ten measurements were made and averaged. Tensile specimens, which had a dimension of 16 mm length ×4 mm width ×0.5 mm thickness, were fabricated parallel to the rolling direction. Tensile test were carried out by an INTESCO tensile machine at a cross head speed of 0.2 mm/min at room temperature. Three tensile tests were made and averaged. Disk-type specimens of 3mm diameter were punched out from a 0.3 mm thick plate and mechanically grounded to about 50 μm in thickness. Final TEM specimens were prepared by electrolytic polishing in a 10 vol. % perchloric acid and 90 vol. % acetic acid using a twin-jet polisher at a voltage of 20 V at room temperature.

TEM has been performed using a JEOL 2200FS operating at 200 kV equipped with a Gatan Imaging Filter (GIF) for EFTEM. The EFTEM images are processed by selecting a small range of inelastically scattered electrons with an energy-selecting slit in the GIF filter.

Table 5-1 Chemical composition of the investigated alloys (wt. %).

Materials	Cr	C	W	Ti	Y ₂ O ₃	Fe
15Cr-ODS	14.9	0.035	1.92	0.29	0.34	Bal.
Fe-15Cr	14.55	0.001	-	-	-	Bal.
Fe-15Cr-C	14.83	0.022	-	-	-	Bal.

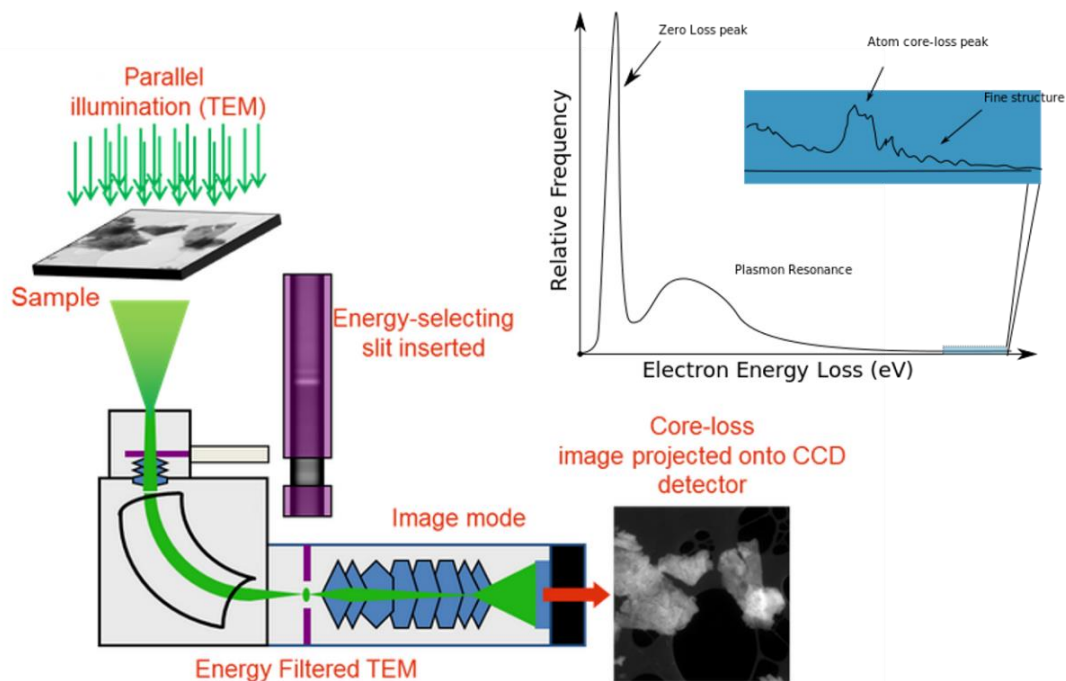


Figure 5-1 Sketch map showing energy-filtered TEM (EFTEM) using an energy selecting slit to allow only a narrow band of energies to form the final image [5].

The three-window method was used to exhibit an inverse power-law behavior [5], as presented in figure 5-2. The two images recorded before the ionization edge corresponding to the chemical element of interest were used to produce an extrapolated background image. Then, the last image was subtracted from the post-edge image to obtain an elemental map. For the chromium $M_{2,3}$ edge elemental map, the two pre-edge energies were 32 eV and 36 eV; while the post-edge energy is 52 eV. Figure 5-3 shows the electron energy loss spectroscopy (EELS) spectrum of Cr $M_{2,3}$ edge [6]. For the titanium $L_{2,3}$ edge elemental map the two pre-edge energies were 406 eV and 441 eV, while the post-edge energy is 476 eV. For the Y $M_{4,5}$ edge elemental map the two pre-edge energies were 109 eV and 139 eV; while the post-edge energy is 172 eV. The chemical compositions of precipitates were measured using the TEM 2200FS equipped with an energy-dispersive X-ray (EDX) spectroscopy system. To quantify the number densities, the thickness of the TEM foils was measured with the aid of EELS by determining the mean free path for energy loss [7, 8].

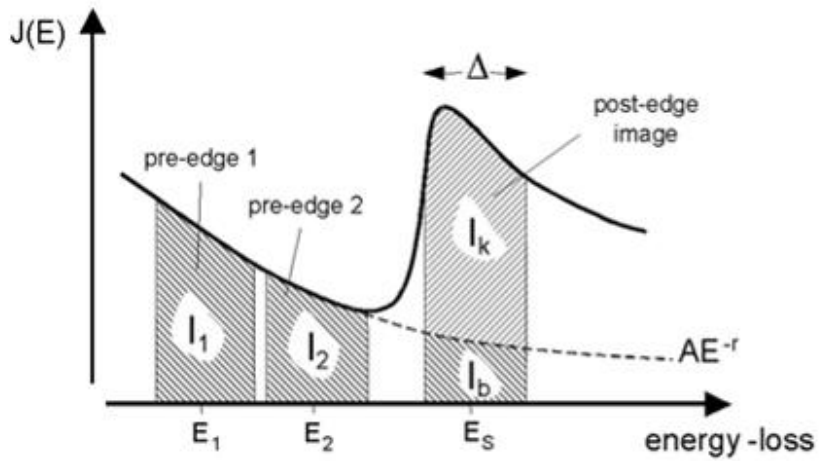


Figure 5-2 A typical EFTEM method called three-window mapping using two pre-edge images to calculate the background in a third post-edge image [5].

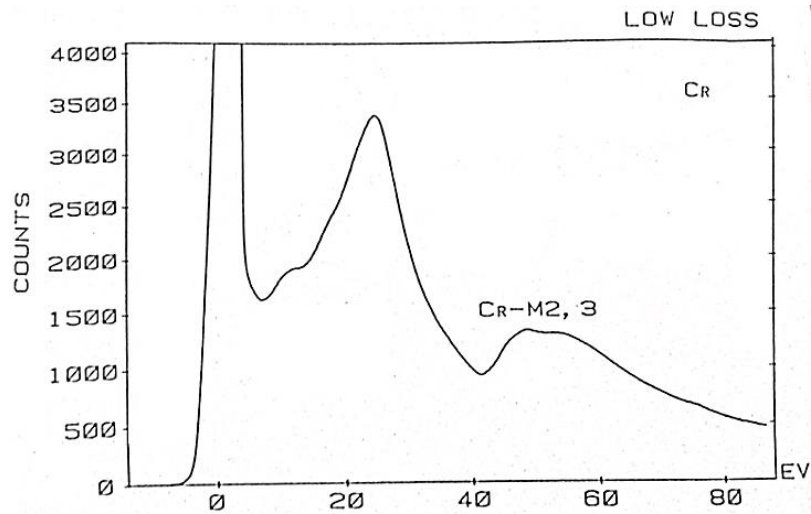


Figure 5-3 Electron energy loss spectroscopy showing Cr $M_{2,3}$ edge spectrum [6].

5.3. Results

5.3.1. Microhardness measurement

The microhardness was measured to characterize the age-hardening behavior of 15Cr-ODS and its model alloys. The evolution of Vickers hardness, HV, and the increment in HV, $\Delta HV = HV - HV_0$, during aging at 475 °C of each material is shown in figure 5-4, where HV_0 is the HV before aging. All of the materials show an increase of hardness after aging. Generally, hardness evolution experiences three different stages, which depend on aging time: Stage-1(ST-1), incubation period (≤ 100 h); Stage-2 (ST-2), under-aging (100-5000 h); Stage-3 (ST-3), over-aging (5000-10,000 h). It seems that 5000 h is a turning period for aging and over-aging caused by thermal aging. In ST-1 and ST-2, the hardness values increase exponentially after an incubation period for all the materials. As aging time reaches 10,000 h, the hardness values decrease slightly as compared to the peak values.

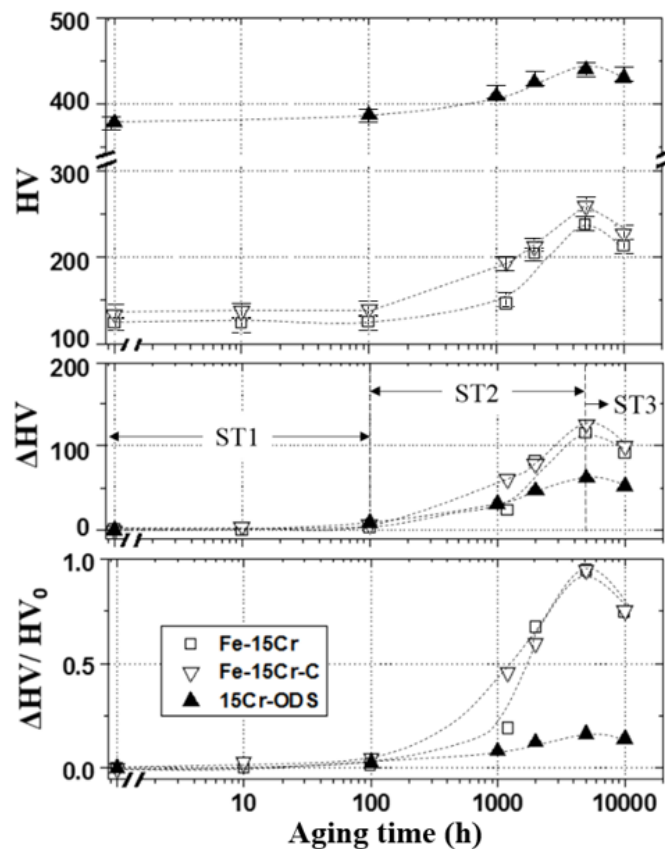


Figure 5-4 Vickers hardness, HV, the increment in hardness, $\Delta HV = HV - HV_0$, and the ratio $\Delta HV / HV_0$ of each material as a function of aging time at 475 °C. HV_0 is the HV before aging.

Fe-15Cr-C shows a faster hardening rate than Fe-15Cr before aging time approaches ~1000 h. In our previous research [9], we have reported that the addition of carbon can lead to the formation of Fe₂C and M₂₃C₆ carbides nearby grain boundaries, which may contribute to the early stage of hardening. Thus, it can be expected that, for 15Cr-ODS, the early stage of hardening is also caused by the formation of carbides. It can be said that 15Cr-ODS shows a smaller hardening than its model alloys up to aging for 5000 h.

The ratio, $\Delta HV/HV_0$, of each material is defined as the hardening ratio, as is also shown in figure 5-4. 15Cr-ODS shows a smaller hardening ratio as compared to Fe-15Cr and Fe-15Cr-C, which indicates that the ODS steel is more resistant to age-hardening than non-ODS alloys.

5.3.2. Tensile properties

As summarized in figure 5-5, the evolution of yield stress, YS, during aging at 475 °C agrees with that of the results of microhardness measurements: the hardening ratio expressed by $\Delta YS/YS_0$ is in good agreement with $\Delta HV/HV_0$. The changes in total elongation of the materials are shown in figure 5-6. Thermal aging usually causes hardening accompanied by reduction in total elongation. For Fe-15Cr, the aging for 5000 h results in a hardening of about 200 MPa of yield stress with a remarkable reduction of total elongation from 30% to 11%. In contrast, 15Cr-ODS shows a smaller hardening accompanied by almost no reduction of total elongation even after aging for 10,000 h.

The relation between ΔYS and $\Delta \epsilon$ is presented in figure 5-7(a). The same amount of hardening results in almost no-loss-of-ductility in 15Cr-ODS but significant ductility loss in Fe-15Cr alloys. A characteristic of 15Cr-ODS is that the hardening is not accompanied by significant ductility loss observed in Fe-15Cr alloys. Figure 5-7(b) shows the relationship between the ductility loss ratio and the hardening ratio of the materials. It is clear that 15Cr-ODS shows a slight change of $\Delta YS/YS_0$, while Fe-15Cr alloys present a significant increase in the ratio. For Fe-15Cr alloys, a linear relationship of $\Delta YS/YS_0$ and $\Delta \epsilon/\epsilon_0$ can be found in Fig. 5b. In contrast, 15Cr-ODS does not show this, indicating that 15Cr-ODS is more resistant to ductility loss caused by age hardening.

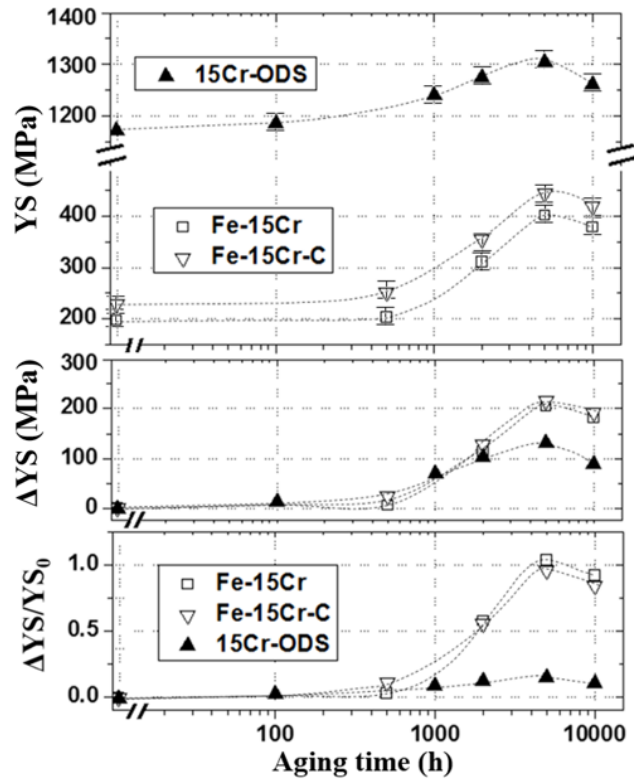


Figure 5-5 Yield stress, YS, the increment in YS, $\Delta YS=YS-YS_0$, and the ratio $\Delta YS/YS_0$ of each material as a function of aging time at 748K. YS_0 is the YS before aging.

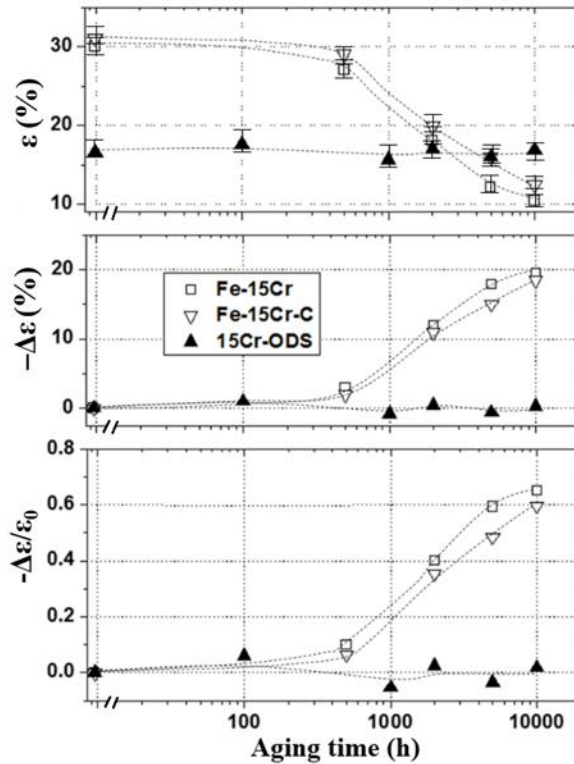


Figure 5-6. Total elongation, ϵ , the change in ϵ , $\Delta\epsilon=\epsilon-\epsilon_0$, and the ratio $\Delta\epsilon/\epsilon_0$ of each material as a function of aging time at 748K. ϵ_0 is the ϵ before aging.

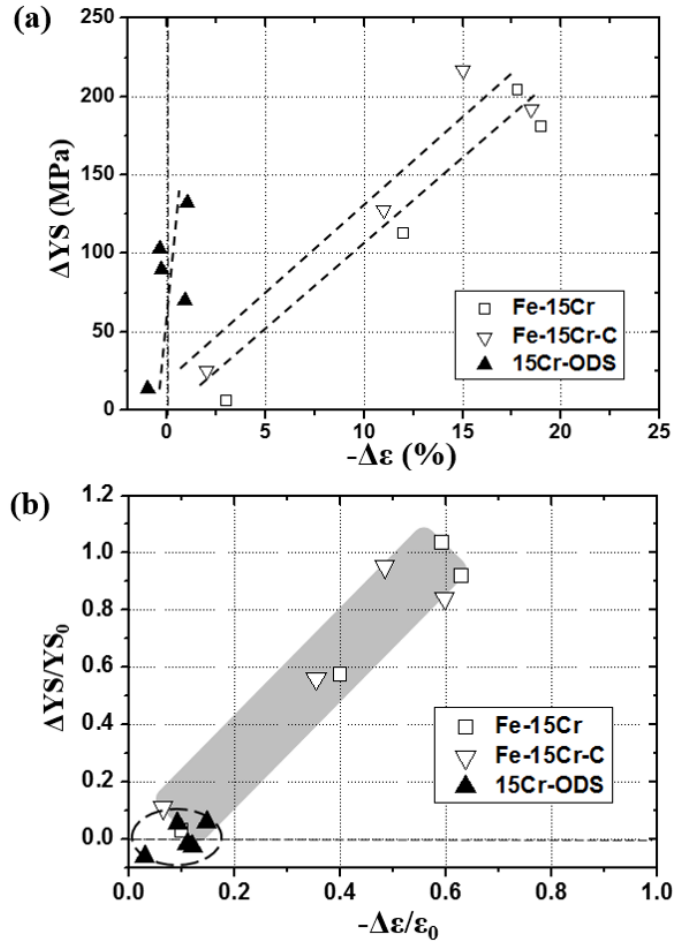


Figure 5-7 The relation between (a) ΔYS and $\Delta \epsilon$, and (b) the hardening ratio, $\Delta YS/Y_{S_0}$, and the ductility loss ratio, $\Delta \epsilon/\epsilon_0$, of the materials after each aging condition at 748K.

5.3.3. Microstructure changes

It is well known that Cr concentration is the main contribution factor for thermal age-hardening behavior at 475 °C [10, 11]. Although the Cr concentration is the same, 15Cr-ODS steel and Fe-15Cr alloys show obvious difference in the age-hardening behavior. Understanding this behavior needs TEM microstructural observations.

Figure 5-8 provides EFTEM Cr $M_{2,3}$ elemental maps of Fe-15Cr alloy. White areas correspond to the area rich in Cr atoms. After aging for 2000 h, the roughly spherical Cr-rich (α') particles are isolated and they appear to grow after aging for 5000 h. Thermal aging at 475 °C leads to nucleation and growth of α' precipitates in Fe-15Cr alloys [12, 13]. Furthermore, with increasing aging time, the size of α' precipitates increases and the density

decreases. In addition, the evolution of the particle size is a non-steady-state of coarsening [14]. The Cr concentration and particle size of the α' phase increase gradually [11].

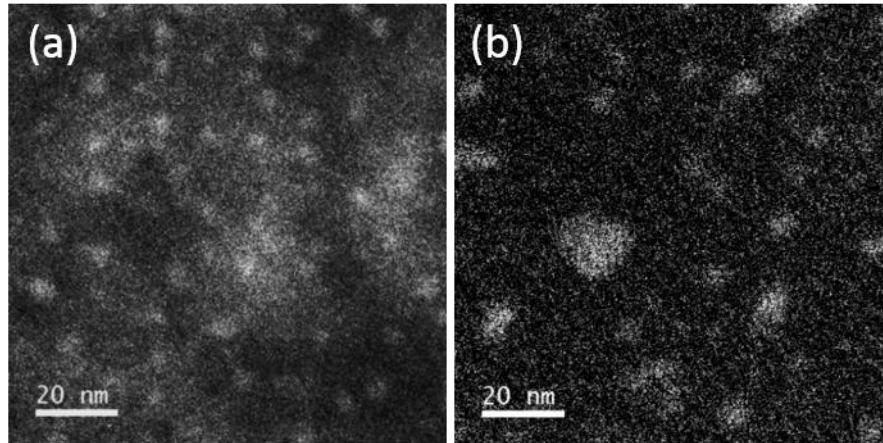


Figure 5-8 Energy-filtered TEM chromium M map showing finely dispersed Cr-rich (α') precipitates in Fe-15Cr alloy after aging at 475 °C for (a) 2000 h, (b) 5000 h.

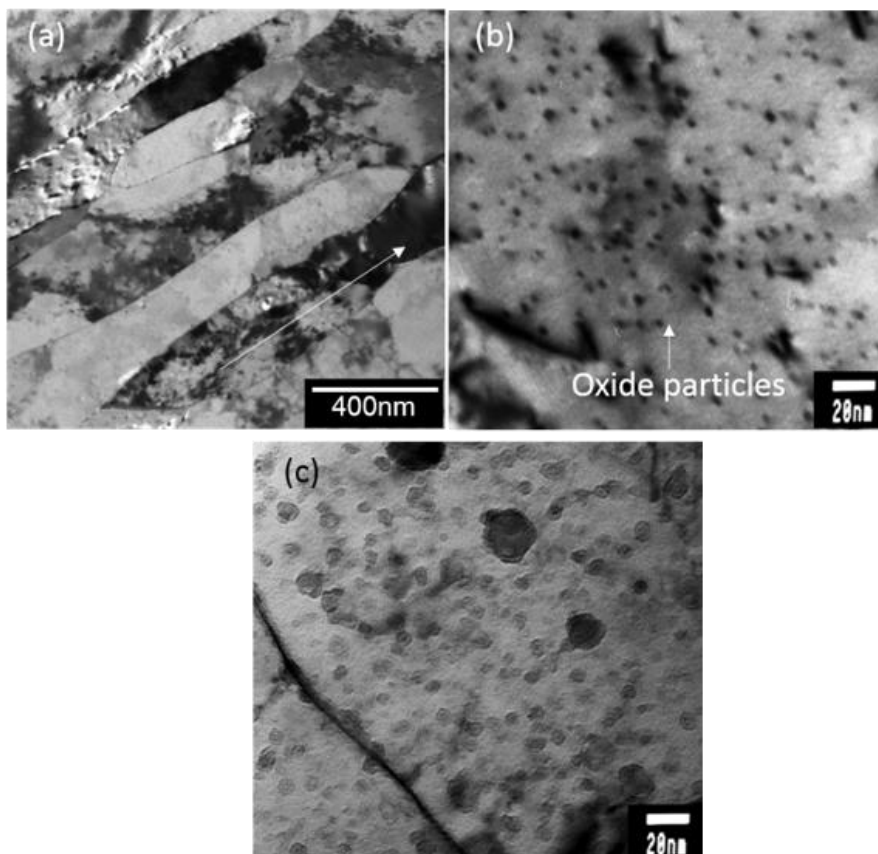


Figure 5-9 TEM Bright field images of 15Cr-ODS showing (a) as-received, grain morphology; (b) as-received, finely dispersed oxide particles; (c) precipitates, after aging for 5000 h.

As presented in figure 5-9(a) and 5-9(b), as-received 15Cr-ODS steel consists of very fine elongated grains because of hot extrusion and forging and a large number density of finely dispersed oxide particles, which contribute to the excellent strength, as illustrated in figure 5-5. After aging for 5000 h, complicated precipitation structures are observed, as shown in figure 5-9(c), where it is difficult to distinguish between pre-existing oxide particles and α' phases produced by α - α' phase separation caused by aging.

For 15Cr-ODS, EFTEM can efficiently characterize the chemistry of precipitates and distinguish Cr-rich precipitates with oxide particles. Figure 5-10(a-d) present EFTEM elemental mapping of 15Cr-ODS after aged for 10, 000 h. Figure 5-10(a) and 5-10(b) show the first pre-edge (32 eV) image of Cr distribution and the final Cr $M_{2,3}$ elemental map. As presented in figure 5-10(b), the α' precipitates can be finely characterized by EFTEM, while other particles can be distinguished by figure 5-10(a). Figure 5-10(c) and 5-10(d) provide EFTEM Ti $L_{2,3}$ and Y $L_{4,5}$ elemental maps. Although no Y map was acquired from the same region, most of the oxide particles in 15Cr-ODS are identified as Y-Ti-O rich particles, as illustrated in figure 5-11, which provides the EDX spectrum of one oxide particle.

Figure 5-12 provide the EFTEM Cr $M_{2,3}$ map, showing that some oxide particles are surrounded by Cr shells in 15Cr-ODS after aged for 10, 000 h. As shown in the sketch map (Fig. 5-12(b)), the oxide particle appears to have a shell structure on its peripheral, which mainly contains Cr atoms. Before thermal aging, Cr is homogenously distributed in the Fe-rich matrix; no Cr-rich clusters were found around oxide particles. The formation of Cr-rich shell structures must be due to the diffusion of Cr to the interfaces of oxide particles and the matrix, where the Cr atoms are trapped because of lowering the interface energy between the particles and matrix [15, 16].

Similar Cr shell structure has been reported in an irradiation study of MA957 ODS alloy by J. Ribis [17]. Because the bonding energies of Y-O and Ti-O are quite higher than Cr-O, it is considered that the Cr shell structure can work as a transition state, where the Gibbs free energy of Cr clusters is lower than that of oxide particles and higher than that of the Fe Matrix.

In order to know the α/α' phase decomposition behaviors, the size and number density of α' precipitates should be statistically analyzed. The stability of oxide particle is also an issue

during thermal aging. Figure 5-13 provides the particle size distribution (PSD) in 15Cr-ODS and Fe-15Cr before and after aging for different times. Before thermal aging, oxide particles are finely dispersed in the matrix of 15Cr-ODS with an average size of 4.0 nm and number density $1.4 \times 10^{23} \text{ m}^{-3}$. After aging for 5000 h, the PSD shows a bi-modal distribution.

Since it has been reported [17] that there are almost no change in the distribution of Y-Ti-O oxide particles after neutron irradiation at $\sim 430 \text{ }^\circ\text{C}$ up to 75 dpa, it is expected that oxide particles could be quite stable during thermal aging at $\sim 475 \text{ }^\circ\text{C}$. The TEM images together with EFTEM suggest that these newly formed precipitates in 15Cr-ODS after aging for 5000 h are α' precipitates with an average size of 8.1 nm and number density $1.6 \times 10^{22} \text{ m}^{-3}$.

Table 5-2 summarizes the calculation results of particle size and number density in 15Cr-ODS and Fe-15Cr before and after aging. Results show that Fe-15Cr contains a higher number density of α' precipitates than 15Cr-ODS at the same aging conditions.

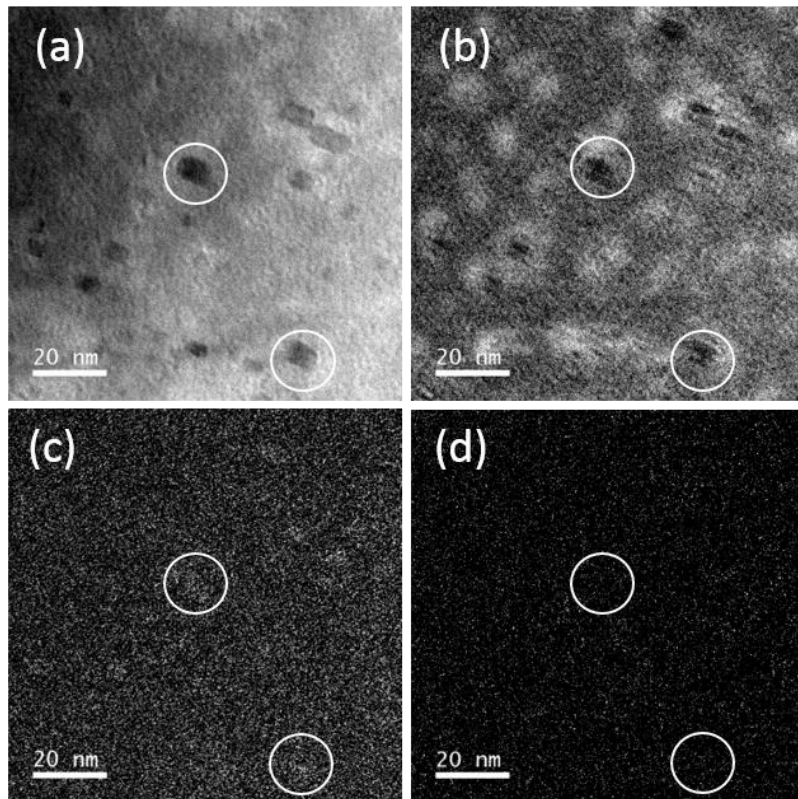


Figure 5-10 EFTEM elemental mapping of 15Cr-ODS after aging for 10,000 h: (a) Cr M edge, first pre-edge image (32 eV), (b) elemental map of Cr M edge, (c) elemental map of Ti $L_{2,3}$ edge, and (d) elemental map of Y $L_{4,5}$.

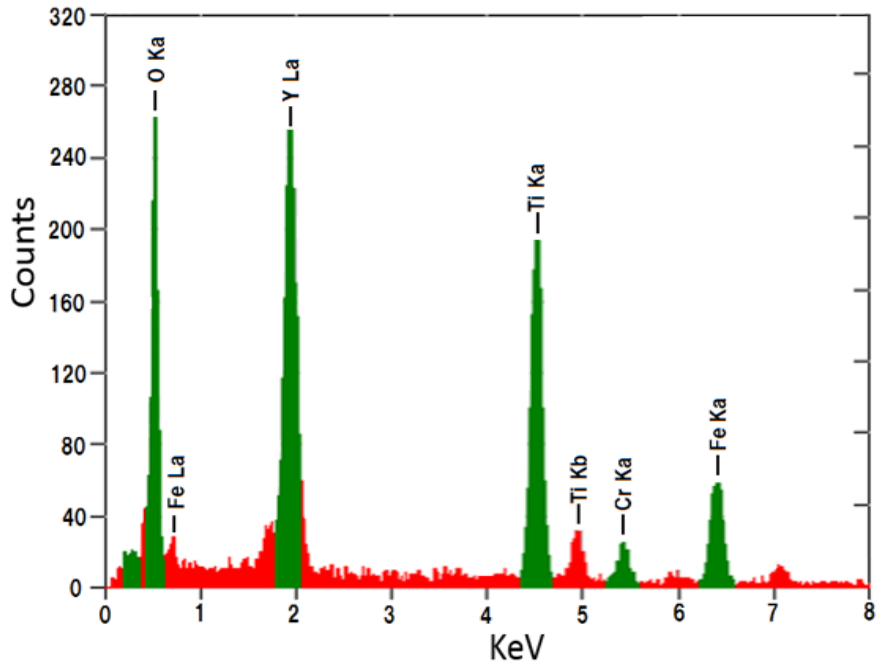


Figure 5-11 TEM energy-dispersive X-ray (EDX) spectrum of one Y-Ti-O oxide particle in 15Cr-ODS.

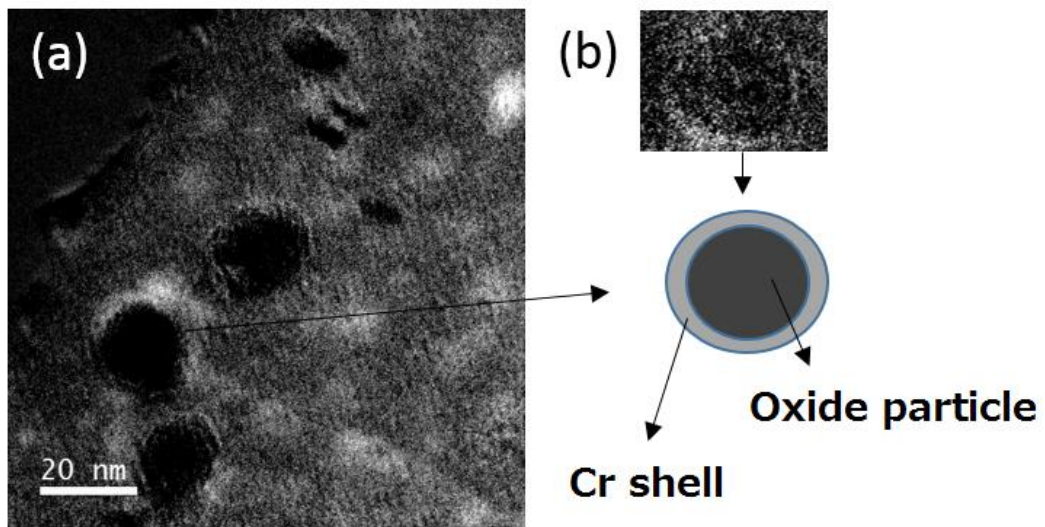


Figure 5-12 (a) EFTEM Cr M edge map of 15Cr-ODS after aging for 10, 000 h, and (b) sketch map showing oxide particle surrounded by Cr shell structure.

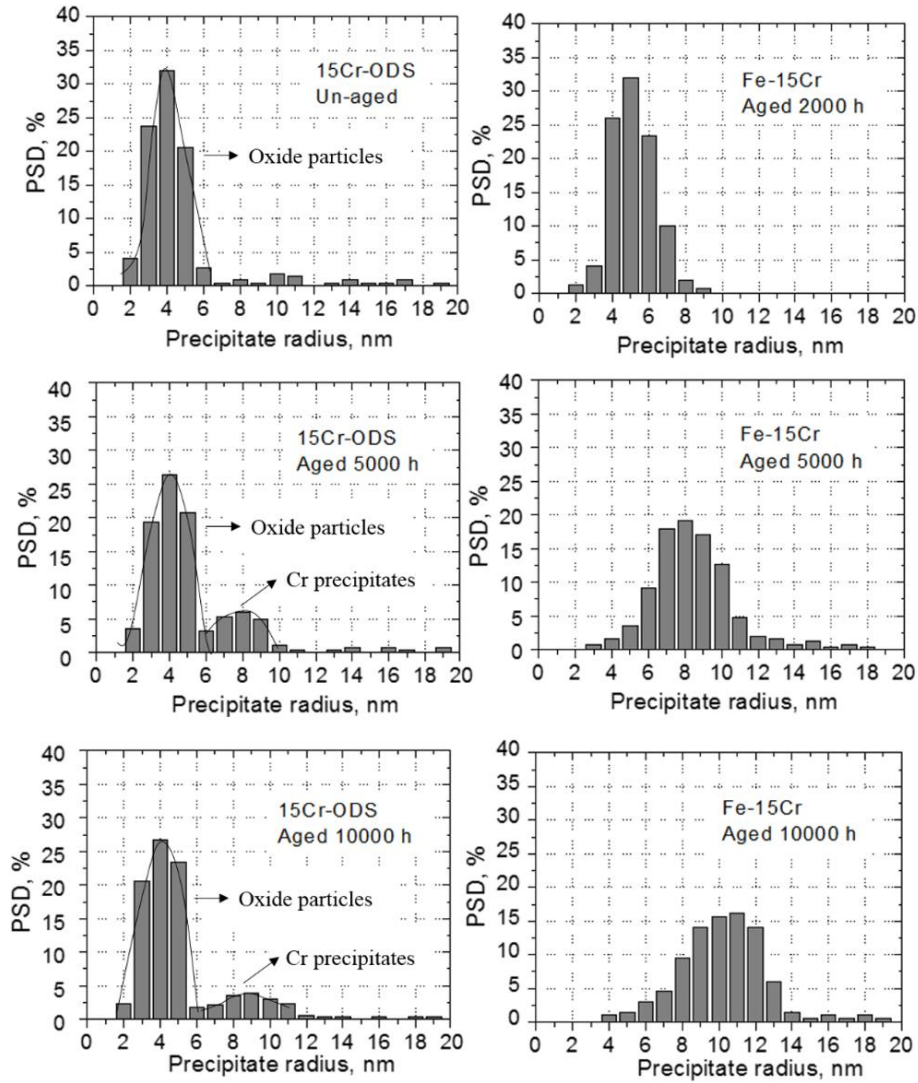


Figure 5-13 The precipitate size distribution (PSD) in 15Cr-ODS and Fe-15Cr before and after aging for different periods.

Table 5-2 Calculation results based on TEM observation.

Materials	Aging time (h)	Number density (m ⁻³)		Average diameter (nm)	
		Cr precipitate	Oxide particle	Cr precipitate	Oxide particle
15Cr-ODS	0	-	1.4×10 ²³	-	4.0
	5000	1.6×10 ²²	1.3×10 ²³	8.1	4.2
	10000	0.8×10 ²²	1.3×10 ²³	9.1	4.3
Fe-15Cr	5000	3.8×10 ²²	-	8.3	-
	10000	1.7×10 ²²	-	11	-

5.4. Discussion

5.4.1. Age-hardening mechanism

With increasing aging time, Vickers hardness and yield stress are increased due to α/α' phase decomposition. The change in yield stress can be interpreted in terms of the Orowan type dispersion strengthening model [22]:

$$\Delta\sigma_y = M\alpha\mu b(Nd)^{\frac{1}{2}} \quad (5.1)$$

where $\Delta\sigma_y$ is the increment in yield stress, M is the Taylor factor (3.06), α is the strength factor (0.2 [23, 24]), μ is the shear modulus (75.3 GPa), b is the Burgers vector (0.248nm), N and d are the number density and the average diameter of α' particles.

Figure 5-14 shows the relation of estimated and measured $\Delta\sigma_y$ for 15Cr-ODS and Fe-15Cr. The estimated values, $\Delta\sigma_y^e$ are consistent with the measured values, $\Delta\sigma_y^m$. This result indicates age-hardening is mainly due to α/α' phase decomposition.

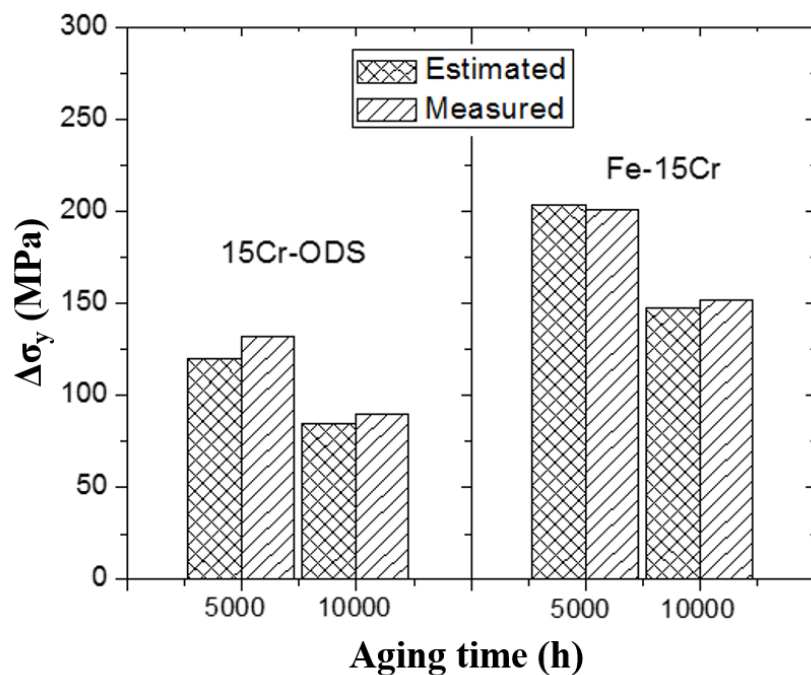


Figure 5-14 Estimated and measured increase in yield stress ($\Delta\sigma_y$) for 15Cr-ODS and Fe-15Cr alloy after aging for 5000 and 10,000 h.

The age-hardening mechanism in 15Cr-ODS steel is quite complicated due to the coexistence of oxide particles and α' precipitates, which have different strength factors. This estimation is based on an assumption that there is no interaction of oxide particles and α' precipitates on age-hardening. As for 15Cr-ODS aged for 5000 h, there is a small difference between $\Delta\sigma_y^e$ and $\Delta\sigma_y^m$. One possible reason is the formation of carbides, which lead to additional hardening. Carbides are also strong obstacles for dislocation [25-27]; More work is necessary to confirm the effect of carbides on age-hardening in 15Cr-ODS.

Based on the comparison of experimental data and estimation data, it is summarized that the hardening caused by α/α' phase decomposition in 15Cr-ODS is lower than that in Fe-15Cr alloys.

5.4.2. Precipitation modeling

Robson [18] developed a numerical model that can be implicated in the interpretation of nucleation and growth of Cr-rich precipitates. The Robson model requires some simplifying assumptions as follows: 1) Nucleation of precipitates is homogeneous within the matrix; 2) The growth and the coarsening of precipitates are diffusion-controlled processes. Additionally, for 15Cr-ODS steel it is assumed that there are no interactions between oxide particles and Cr-rich precipitates on age hardening.

5.4.2.1. Nucleation

The steady-state nucleation rate J during thermal aging, neglecting the incubation period, is calculated by [19]

$$J = N_0 \cdot \frac{kT}{h} \cdot \text{EXP}\left(-\frac{G^* + Q}{kT}\right) \quad (5.2)$$

where N_0 is the number of nucleation sites per unit volume, h is the Planck constant. In the case of homogeneous nucleation, the parameter N_0 is computed as the number of chromium atoms per unit volume. The activation energy G^* [18] required for the nucleation of new particles of the critical radius r^* is computed according to [20]

$$G^* = \frac{4}{3} \pi r^{*2} \cdot \sigma \quad (5.3)$$

$$r^* = \frac{2\sigma V_\alpha}{kT \ln \frac{c}{c_\infty^\alpha}} \quad (5.4)$$

where σ is the interfacial energy between the Fe matrix and the Cr precipitates, V_α is the atomic volume of Cr, k is the Boltzmann constant, T is the aging temperature, c is the instantaneous concentration of Cr in the matrix, and c_∞^α is the concentration of Cr in the matrix in equilibrium with Cr precipitates assuming a planar interface.

It can be inferred that the driving force for the nucleation process is the instantaneous concentration of Cr in the matrix. This stage of the precipitation process is consequently exhausted when the concentration of chromium c is close to the equilibrium concentration c_∞^α at the corresponding temperature.

5.4.2.2. Growth

In the case of diffusion controlled growth of spherical Cr-rich precipitates, the growth rate is given by [20, 21]

$$\frac{dr}{dt} = \frac{D}{r} \frac{c - c_r^\alpha}{c^{\alpha'} - c_r^\alpha} \quad (5.5)$$

where D is the diffusion coefficient of Cr in Fe at a defined temperature, r is the discrete precipitate radius, c_r^α is the concentration of Cr in the matrix at the interface and $c^{\alpha'}$ is the concentration of Cr in the Cr precipitate.

The parameter c_r^α is calculated for every particle radius for the generalized Gibbs-Thomson equation:

$$c_r^\alpha = c_\infty^\alpha \cdot \exp\left(\frac{2\sigma V_\alpha}{kT} \cdot \frac{1}{r}\right) \quad (5.6)$$

The dependence of the diffusion parameter D on the aging temperature T is expressed according to the Arrhenius-type equation:

$$D = D_0 \cdot \exp\left(-\frac{Q}{RT}\right) \quad (5.7)$$

It can be deduced that the thermal stability of Cr precipitates depends on the changes in temperature during the aging process. Therefore, in the case of a non-isothermal aging process, an increase in temperature leads to the dissolution of existing precipitates. However, this phenomena does not occur in current work because a single step aging at constant

temperature was used.

The governing driving force for coarsening is the difference between the matrix concentration in the vicinity of small and large particles, which leads to diffusion flux of the solute atoms from smaller particles to larger ones. This phenomenon is caused by the Gibbs-Thomson effect included in the precipitation model, which changes the phase equilibrium between the precipitates and the matrix and also increases the solute concentration around small particles due to the interfacial curvature.

For Fe-15Cr alloy, coarsening of Cr precipitates arises naturally as interpreted by the Robson model, while in the case of 15Cr-ODS steel, Cr clusters were found at the interfaces of oxide particles and the matrix, as shown in figure 5-12. This means oxide particles can work as trapping sites for Cr atoms, which could decrease the Cr concentration in the matrix. As the fraction of Cr solution in the matrix decreases during precipitation, the driving force for nucleation and growth of Cr precipitates decreases. The Robson precipitation model agrees with our calculation results, which show that 15Cr-ODS steel contains a lower number density of Cr-rich precipitates than Fe-15Cr at the same aging conditions.

5.4.3. Roles of oxide particles

Although the Cr concentration in matrix before thermal aging is almost the same, 15Cr-ODS and Fe-15Cr alloys show a difference in α/α' phase decomposition behavior. Both 15Cr-ODS and Fe-15Cr show a peak in the age-hardening showing so-called over-aging around 5000 h, suggesting that the kinetics of age hardening were not influenced by the existence of oxide particles. It is noticeable that the peak value of age hardening of 15Cr-ODS is smaller than that of Fe-15Cr. This can be interpreted in terms of trapping Cr atoms at nano-scaled oxide particles, which are semi-coherent with the matrix. Trapping Cr atoms at oxide particles may reduce the number density of α' precipitates, and the trapped Cr atoms form a Cr-shell structure, as shown in figure 5-12. The TEM observation results clearly show that the number density of α' precipitates are more than two times smaller in 15Cr-ODS than Fe-15Cr. Equation (5-1) indicates that the smaller age hardening of the ODS steel is due to the smaller number density of α' precipitates. It is also considered that the strength factor, α , of

oxide particles is not significantly influenced by the formation of Cr-shell structure.

The most important result obtained in this research is that it is not the phase separation kinetics but the precipitation morphology of α' precipitates that is affected by nano-sized oxide particles, which results in a lower susceptibility to age hardening of 15Cr-ODS steel than Fe-15Cr model alloys. Nevertheless, this result can also provide important implications for the design of high-Cr steel for nuclear power application.

5.5. Summary

The effects of thermal aging at 475 °C up to 10,000 h on α/α' phase decomposition behavior in 15Cr-ODS steel and its Fe-15Cr model alloys have been investigated. The obtained results are summarized as follows:

- (1) A smaller age hardening is observed in 15Cr-ODS in comparison to Fe-15Cr alloys. A characteristic feature of the hardening in the ODS steel is that the hardening is not accompanied by significant ductility loss that is observed in Fe-15Cr alloys at the same aging condition.
- (2) Energy-filtered TEM can effectively characterize the distribution of Cr precipitates caused by α/α' phase decomposition, especially in steel containing nano-scaled oxide particles. A Cr shell structure is observed on the interfaces of oxide particles and the matrix, where defect formation energy is considered to be lower than that in the matrix.
- (3) The age hardening is correlated with α/α' phase decomposition by the Orowan type strengthening model, which indicates that the smaller age hardening of 15Cr-ODS steel is due to the smaller number density of α' precipitates than Fe-15Cr alloy.
- (4) Oxide particles play a role as trapping sites for Cr atoms, which leads to a decrease in the number density of α' precipitates. Not the phase separation kinetics but the precipitation morphology of α' precipitates is affected by nano-sized oxide particles, which results in a lower susceptibility to age-hardening of 15Cr-ODS steel than Fe-15Cr alloys.

References

- [1] T.J. Nichol, A. Datta, G. Aggen, “Embrittlement of ferritic stainless steel”, *Metal. Trans. A*, **11** (1980) p. 573
- [2] M. Klimiankou, R. Lindau, A. Möslang, “Energy-filtered TEM imaging and EELS study of ODS particles and Argon-filled cavities in ferritic–martensitic steels”, *Micron*, **36** (2005) p. 1-8
- [3] Reimer, 1997, in: L. Reimer (Ed.), “Transmission Electron Microscopy”, *Springer Series in Optical Science*, 36 (1997), p. 452
- [4] M. Hättestrand, H.O. Andre, “Evaluation of particle size distributions of precipitates in a 9% chromium steel using energy filtered transmission electron microscopy”, *Micron*, **32** (2001) p. 789–797
- [5] <http://www.gatan.com/techniques/eelseftem>
- [6] EELS spectrum book of FE-TEM (JEOL, FS2200, Kyoto University)
- [7] T. Mails, S.C. Cheng, R.F. Egerton, “EELS log-ratio technique for specimen-thickness measurement in the TEM”, *J. Electron Micro. Tech.*, **8(2)** (1988) p. 193-200
- [8] B. Feta, U. Abebi, “Determination of the inelastic mean free path of electrons in vitrified ice layers for on-line thickness measurements by zero-loss imaging”, *J. Micros.*, **193(1)** (1999) p. 15-19
- [9] D.S. Chen, A. Kimura, C.H. Zhang, W.T. Han, “Effect of alloying elements on thermal aging embrittlement of Fe-15Cr ferritin alloys”, in *PRICM: 8th Pacific Rim International Congress on Advanced Materials and Processing (PRICM-8)*, (2013) p. 529-536
- [10] P.J. Grober, “The 885 °F (475 °C) embrittlement of ferritic stainless steels”, *Metall. Trans.*, **4** (1973) p. 251-260
- [11] T.J. Nichol, A. Datta, G. Aggen, “Embrittlement of ferritic stainless steels”, *Metall Trans. A*, **11A** (1980) p. 573-585
- [12] J. Chao, C. Capdevila, M. Serrano, A. Garcia-Junceda, J.A. Jimenez, M.K. Miller, “Effect of α - α' phase separation on notch impact behavior of oxide dispersion strengthened (ODS) Fe₂₀Cr₅Al alloy”, *Mater. Des.*, **53** (2014) p. 1037-1046
- [13] S.M. Dubiel, J. Zukrowski, “Fe-rich border and activation energy of phase

- decomposition in a Fe-Cr alloy”, *Mater. Chem. and Phys.*, **141** (2013) p. 18-21
- [14] S.M. Dubiel, J. Żukrowski, “Phase-decomposition-related short-range ordering in an FeCr alloy”, *Acta Mater.*, **61** (2013) p. 6207
- [15] S. Novy, P. Pareige, C. pareige, “Atomic scale analysis and phase separation understanding in a thermally aged Fe-20 at. %Cr alloy”, *J. Nucl. Mater.*, **384** (2009) p. 96-102
- [16] Q. Jiang, D.S. Zhao, M. Zhao, “Size-dependent interface energy and related interface stress”, *Acta Mater.*, **49** (16) (2001) p. 3143-3147
- [17] P. Dou, A. Kimura, R. Kasada, T. Okuda, M. Inoue, S. Ukai, S. Ohnuki, T. Fujisawa, F. Abe, “TEM and HRTEM study of oxide particles in an Al-alloyed high-Cr oxide dispersion strengthened steel with Zr addition” *J. Nucl. Mater.*, **444** (2014) p. 441-453
- [18] J. Ribis, S. Lozano-Perez, “Nano-cluster stability following neutron irradiation in MA957 oxide dispersion strengthened material”, *J. Nucl. Mater.*, **444** (2014) p. 314-322
- [19] J.D. Robson, “Modelling the overlap of nucleation, growth and coarsening during precipitation”, *Acta Mater.*, **52** (2004) p. 4669-4676
- [20] J.W. Christian, “The theory of transformations in metals and alloys”, vols, 1-2, 3rd ed., *Pergamon Press, Oxford*, (2002)
- [21] R. Kampmann, R. Wagner, “A comprehensive treatment”, *Mater. Sci. Tech.*, **5** (1991) p. 213-303
- [22] J.S. Langer, A.J. Schwartz, “Kinetics of nucleation in near-critical fluids”, *Phys. Rev. A*, **21** (1980) p. 948-958
- [23] G.E. Lucas, “The Evolution of Mechanical Property Changes in Irradiated Austenitic Stainless Steels”, *J. Nucl. Mater.*, **206** (1993) p. 287-305
- [24] D. Chen, A. Kimura, W. Han, “Correlation of Fe/Cr phase decomposition process and age-hardening in Fe-15Cr ferritic alloys”, *J. Nucl. Mater.*, **455** (2014) p. 436-439
- [25] S.M. Hafez Haghghat, R. Schaubin, D. Raabe, “Atomistic simulation of the a(0) <100> binary junction formation and its unzipping in body-centered cubic iron”, *Acta Mater.*, **64** (2014) p. 24-32
- [26] C.G. Panait, A. Zielinska-Lipiec, T. Koziel, et al., “Evolution of dislocation density, size of subgrains and MX-type precipitates in a P91 steel during creep and during thermal

- ageing at 600 C for more than 100, 000 h”, *Mater. Sci. Eng. A*, **527** (2010) p. 4062-4069
- [27] T. Sourmail, H. Bhadeshia, “Microstructural evolution in two variants of NF709 at 1023 and 1073 K”, *Mater. Sci. Tech.*, **17** (2001) p. 1-14

Chapter 6

Summary and Conclusions

Chapter 1 is the introduction and objectives of this research. Structural material R&D is essential for the realization of Generation IV fission nuclear reactors as well as fusion DEMO reactors and beyond because the materials requirements are so high that there is no adequate material to meet the requirements. It has been demonstrated that high-chromium oxide dispersion strengthened (ODS) ferritic steels, which contain nano-clusters enriched with Y, Ti and O, show excellent high-temperature tensile and creep strength, high corrosion and oxidation resistance in supercritical pressurized water and high resistance to irradiation. Therefore, high-Cr ODS ferritic steels have been considered to be a candidate advanced structural material for Generation IV nuclear systems with higher thermal efficiency, such as supercritical pressurized water reactors (SCWR) and lead cooled fast reactor (LFR), as well as sodium cooled fast reactor (SFR). However, a “trade-off” between corrosion resistance and aging embrittlement caused by increasing Cr content is one of the critical issues for the practical use of high-Cr ODS steels. Long-term aging tests are necessary to assess the performance of high-Cr ODS ferritic steels as structural material of advanced nuclear systems with high thermal efficiency and of high burn-up operation.

In this research, the iron/chromium (Fe/Cr) phase decomposition behavior of high-Cr ODS steels is investigated to understand the effect of oxide particles on the phase decomposition behavior and to know the age-hardening mechanism of ODS ferritic steels.

For comparison, those of conventional SUS430 ferritic steel and Fe-15Cr alloys were also investigated after the long-term isothermal aging at 475 °C for up to 10,000 hr. Both conventional transmission electron microscopy (TEM) and energy-filtered TEM were used to characterize the Cr-rich precipitates caused by thermal aging and Fe/Cr (α/α') phase decomposition behavior. The age-hardening was evaluated by microhardness measurement, miniaturized tensile tests and small-punch (SP) tests. In addition, the correlation of Fe/Cr phase decomposition and age-hardening behavior was interpreted in terms of dispersed strengthening models.

In Chapter 2, as a basic research on aging effect in high-Cr alloys, the effect of alloying elements on age-hardening in Fe-15Cr alloys were investigated and the following results were obtained:

- (1) Thermal aging at 475 °C for 5000 h resulted in a significant increase in the hardness and tensile strength accompanied by a remarkable decrease in total elongation of Fe-15Cr alloys.
- (2) TEM observation revealed that the addition of carbon and other alloying elements, such as Si, Mn and Ni, caused the formation of some $M_{23}C_6$ carbides and few Mn-Si-Ni enriched G phases on or nearby grain boundaries.
- (3) The formation of isolated Cr-rich precipitates and $M_{23}C_6$ carbides as well as G phases, contributes to the significant age-hardening accompanied by α/α' phase decomposition in Fe-15Cr alloys.
- (4) Age-hardening is mainly caused by Fe/Cr phase decomposition, while alloying elements play a small role in the total age-hardening.

In Chapter 3, the age-hardening was correlated with the Fe/Cr phase decomposition in Fe-15Cr alloy:

- (1) The isolated α' precipitates were formed during aging at 475 °C via nucleation, growth and coarsening processes in Fe-15Cr alloys. As aging time increases, the mean size of α' precipitates increases linearly with the aging time. The number density of α' precipitates experiences a rapid increase followed by a progressive decrease.
- (2) TEM observations of evolution of α' precipitates show a good agreement with the density functional theory (DFT) calculation results, which indicate that the later stage of Fe/Cr phase decomposition in Fe-15Cr alloy is a non-steady-state of coarsening, with an overlap of nucleation, growth and dissolution of small α' particles. The component of α' precipitates is mainly chromium.
- (3) Age-hardening shows two stages: increasing (strengthening) and decreasing (over aging), showing a peak in the strength with increasing aging period.
- (4) The age-hardening in strengthening period is interpreted in terms of the dispersed barrier strengthening models with α' precipitates. The strengthening factor of α' precipitates is assumed to be 0.2 at room temperature. Both the Orowan type dispersed strengthening model and the Scattergood and Bacon (SB) continuum model can be applied to explain the age-hardening caused by α/α' phase decomposition after a longer aging time.

- (5) The over aging after aging beyond 5000 h is associated with the reduction of number density and the increase in the size of α' precipitates. The critical size of α' precipitates for strengthening and softening is around 8 nm.

In Chapter 4, age-hardening susceptibility and mechanism of high-Cr ODS ferritic steels and SUS430 ferritic steel were investigated and the following results were obtained:

- (1) After thermal aging, SUS430 steel shows a larger increase in hardness and strength than 15Cr-ODS steel, while there is almost no hardening for 12Cr-ODS steel. A characteristic of the ODS steels is that the hardening is not accompanied by a remarkable ductility loss that is observed in SUS430 steel. It is considered that in ODS steel, sub-micron sized grains suppress the localized slip that reduces total elongation by offering a number of dislocation sources.
- (2) The results of small punch test suggest that SUS430 suffers a larger DBTT shift to higher temperature than that for 15Cr-ODS, which is consistent with tensile test results. No remarkable change in fracture mode was observed after aging for 10,000 h, and all the materials still present ductile fracture at room temperature.
- (3) TEM EDX analyses indicate that thermally aged SUS430 contains quite small amount of G phases enriched with Cr-Mn-Si. Very few $M_{23}C_6$ carbides are observed in 15Cr-ODS. After 10,000 h aging, the Cr precipitates are found to be semi-coherent particles and have a partial cube-on-cube orientation with Fe matrix.
- (4) The main difference of age-hardening behavior in SUS430 and ODS steels may be interpreted in terms of a nucleation rate controlling theory based on Grobner's theory. Results indicate that thermal aging results in the appearance of age-hardening in the order of SUS430, 15Cr-ODS and 12Cr-ODS, which shows a good agreement with age-hardening level of the materials.
- (5) The correlation of age-hardening and α/α' phase decomposition is interpreted by the Orowan type strengthening model, which indicates 15Cr-ODS has a lower age-hardening susceptibility than SUS430.

In Chapter 5, the roles of nano-sized oxide particles in α/α' phase decomposition behavior of 15Cr-ODS ferritic steel were investigated and the following results were obtained:

- (1) Thermal aging causes a smaller age-hardening in 15Cr-ODS steel in comparison to Fe-15Cr alloys. A characteristic of ODS steel is that the hardening is not accompanied by significant ductility loss that is observed in Fe-15Cr alloys at the same aging conditions.
- (2) Energy-filtering EFTEM analysis can efficiently characterize the distribution of Cr precipitates caused by α/α' phase decomposition, especially in steel containing nano-scaled oxide particles. A Cr shell structure is observed on the interfaces of oxide particles and the matrix, where defect formation energy is considered to be lower than that in the matrix.
- (3) The Robson's model is used to interpret the nucleation and growth process of α' precipitates in ODS steel. Oxide particles play a role as trapping sites for Cr atoms, which leads to a decrease in the number density of α' precipitates. Not the phase decomposition kinetics but the precipitation morphology of α' precipitates is affected by nano-scaled oxide particles.
- (4) The age-hardening is correlated with the α/α' phase decomposition by the Orowan type strengthening model, which indicates that the smaller age hardening of 15Cr-ODS steel is due to the smaller number density of α' precipitates than Fe-15Cr alloys.

In conclusion, nano-sized oxide particles affect Fe/Cr phase decomposition behavior, namely, aging effects in high Cr steels.

List of Publications

1. D.S. Chen, W.T. Han, Y. Ha, A. Kimura, “Characteristic age hardening behavior of 15Cr-ODS ferritic steel”,
Journal of Nuclear Materials, (in preparation)
 2. D.S. Chen, A. Kimura, W.T. Han, H. Je, “Age-hardening susceptibility of high-Cr ODS ferritic steels and SUS430 ferritic steel”,
Fusion and Engineering Design, 2015 (under review)
 3. D.S. Chen, A. Kimura, W.T. Han, W.Y. Tang, “Effect of long-term thermal aging on microstructure and mechanical property changes of Fe-15Cr ferritic alloys”,
Journal of Plasma and Fusion Research SERIES, (2015) p. 58-61
 4. D.S. Chen, A. Kimura, W.T. Han, “Correlation of Fe/Cr phase decomposition process and age-hardening in Fe-15Cr ferritic alloys”,
Journal of Nuclear Materials, 455 (2014) p. 436-439
 5. D.S. Chen, A. Kimura, C.H. Zhang, W.T. Han, “Effects of Alloying Elements on Thermal Aging Embrittlement of 15Cr Ferritic Alloys”,
John Wiley & Sons, Inc., Hoboken, NJ, USA. (2013) doi: 10.1002/9781118792148.ch64
-
6. W.T. Han, A. Kimura, N. Tsuda, H. Serizawa, D.S. Chen, H. Je, H. Fujii, Y. Ha, Y. Morisada, H. Noto, “Effects of mechanical force on grain structures of friction stir welded oxide dispersion strengthened ferritic steel”,
Journal of Nuclear Materials, 455 (2014) p.46-50
 7. W.T. Han, N. Tsuda, D.S. Chen, Y. Ha, H. Je, H. Noto, H. Serizawa, H. Fujii, K. Yabuuchi, A. Kimura, “Effects of rotation speed on microstructure and hardness of friction stir welded ODS ferritic steels”,
Proceedings of 1st International Joint Symposium on Joining and Welding (IJS-JW2013), 2013, p. 81-85

List of Presentations

International conference

1. D.S. Chen, A. Kimura, “Aging effect on the microstructure and mechanical property of Fe-15Cr ferritic steels”, *The 11th China-Japan Symposium on Materials for Advanced Energy Systems & Fusion Engineering (CJS-11)*, Sichuan, China, Sep 11-14, 2012, Session 14, O35 (Oral presentation)
2. D.S. Chen, A. Kimura, C.H. Zhang, H. Noto, “Thermal aging effect on microstructure and mechanical properties of Fe-15Cr ferritic steels”, *The 2nd Germany-Japan Workshop on Energy Materials Science*, Karlsruhe, Germany, Dec 12-17, 2012 (Oral presentation)
3. D.S. Chen, A. Kimura, H. Noto, W.T. Han, C.H. Zhang, “Effect of alloying elements on thermal aging embrittlement of 15Cr ferritic alloys”, *The 8th Pacific Rim International Congress on Advanced Materials and Processing*, Hawaii, United States of America, Aug 4-9, 2013 (Poster section)
4. D.S. Chen, A. Kimura, W.T. Han, “Correlation of Fe/Cr phase decomposition process and age-hardening in Fe-15Cr ferritic alloys”, *The 16th International Conference on Fusion Reactor Materials*, October 20-26, 2013, Beijing, China (Poster section)
5. D.S. Chen, F. Okino, H. Negm, K. Hada, K. Daichi, T.A. Ngo, R. Kasada, S. Konishi, “TRL evaluation of energy related research”, *Joint Symposium Ajou University and Kyoto University on Energy Science*, Feb 25, 2014, Kyoto, Japan (Oral presentation)
6. D.S. Chen, A. Kimura, “Correlation of microstructure characteristics and mechanical properties of high-Cr ODS ferritic steels and SUS430 stainless steel during 475 °C thermal aging”, *The 3rd German-Japanese Seminar on Zero-Emission Energy*, March 17-19, 2014, Kyoto University, Kyoto, Japan (Oral presentation)
7. D.S. Chen, A. Kimura, W.T. Han, “Effect of long-term thermal aging on the age-hardening behavior of 15Cr-ODS steel and its Fe-15Cr model alloys”, *The 12th Japan-China Symposium on Materials for Advanced Energy Systems and Fission & Fusion Engineering*, September 17-20, 2014, Shizuoka, Japan (Oral presentation)

8. D.S. Chen, A. Kimura, W.T. Han, H. Je, “Age-hardening susceptibility of high-Cr ODS ferritic steels and SUS430 ferritic steel”, The 28th Symposium on Fusion Technology, Sep 29th - Oct-3rd, 2014, San Sebastian, Spain (Poster section)

Domestic conference

1. D.S. Chen, A. Kimura, “Influence of the α/α' phase separation on the mechanical properties of Fe-15Cr ferritic alloys”, The Spring Meeting of the Japan Institute of Metals and Materials, 2013 Autumn Annual Meeting of the Japan Institute of Metals and Materials, September 17-19, 2013, Kanazawa University, Kanazawa (Oral presentation)
2. D.S. Chen, A. Kimura, “Comparison of the age-hardening susceptibility between high-Cr ferritic oxide dispersion strengthened steels and SUS430 stainless steel”, 2014 Spring Meeting of the Japan Institute of Metals and Materials, March 21-23, 2014, Tokyo Institute of Technology, Tokyo (Oral presentation)
3. D.S. Chen, A. Kimura, W.T. Han, H. Je, “Comparison of the age-hardening susceptibility between high-Cr ODS ferritic steels and SUS430 ferritic steel”, The 10th Symposium of Nuclear Fusion Energy, June 19-20, 2014, Tsukuba (Poster section)
4. D.S. Chen, A. Kimura, “Comparison of age-hardening behavior between ODS ferritic steel and SUS430 ferritic steel”, 2014 Fall Meeting of the Atomic Energy Society of Japan, September 8-10, 2014, Kyoto University, Kyoto (Oral presentation)
5. D.S. Chen, A. Kimura, W.T. Han, Y. Ha, Y. Hayashi, “Effect of long-term thermal aging on the age-hardening behavior of 15Cr-ODS steel and its model alloys”, September 24-26, 2014, Nagoya University, Nagoya (Oral presentation)

Acknowledgement

First and foremost, I would like to express my thanks to my Ph. D advisor, Professor AKIHIKO KIMURA, for his patient guidance, positive encouragement, for his continuous support of my study and research. Especially, I was completely impressed by his immense knowledge and ability to inspire. Without his diligent guidance and enthusiastic help, this dissertation would not have been possible.

I would also like to thank the members of my thesis committee, Prof. Hoshide and Prof. Imatani for their helpful comments and suggestions.

I have to acknowledge Prof. Kasada, Prof. Iwata and Prof. Morishita for their encouragement and practical advice.

I would also like to thank to the members of Kimura-Lab., (Dr Han, Dr Yabuuchi, Dr. Noto, Dr Je, Dr Ha, Mr Zhang, Mr Yamamoto, Mr Sugino, Mr Tsuda, Mr Maekawa, Mr Murai, Mr Kubo, Mr Taniguchi, Mr Yamaguchi, Mr Nakasuji, Mr. Okunishi), for their assistances in many aspects. Especially, I must offer my thanks to Dr. Han Wentuo and Dr. Ha Yoosung for spending time in discussion.

My sincere thanks also gives to Mrs. Wada for offering me so much convenience for not only academic research but also the life in Japan.

I appreciate the financial support from China Scholarship Council (CSC) and Global-Centers of Excellence (GCOE) program that funded parts of my research.

Most importantly, I wish to thank my parents, Chen Fude and Ding Furui. Their love always provides my inspiration and driving force. Also, I would like to thank my wife, Tang Wenyue, whose love and encouragement make this journey much more meaningful and happier.